Washington University in St. Louis
Washington University Open Scholarship

Arts & Sciences Electronic Theses and Dissertations

Arts & Sciences

Spring 5-15-2022

Distributed X-ray Sources for X-ray Imaging and Small Animal FLASH Irradiator

Yuewen Tan
Washington University in St. Louis

Follow this and additional works at: https://openscholarship.wustl.edu/art_sci_etds

Part of the Physics Commons

Recommended Citation

Tan, Yuewen, "Distributed X-ray Sources for X-ray Imaging and Small Animal FLASH Irradiator" (2022). *Arts & Sciences Electronic Theses and Dissertations*. 2727.
https://openscholarship.wustl.edu/art_sci_etds/2727

This Dissertation is brought to you for free and open access by the Arts & Sciences at Washington University Open Scholarship. It has been accepted for inclusion in Arts & Sciences Electronic Theses and Dissertations by an authorized administrator of Washington University Open Scholarship. For more information, please contact digital@wumail.wustl.edu.

WASHINGTON UNIVERSITY IN ST. LOUIS

Department of Physics

Dissertation Examination Committee:

Tiezhi Zhang, Co-Chair
Erik Henriksen, Co-Chair
Arash Darafsheh
Ryan Ogliore
Lee Sobotka

Distributed X-Ray Sources for X-Ray Imaging and Small Animal FLASH Irradiator

by

Yuewen Tan

A dissertation presented to
The Graduate School
of Washington University in
partial fulfillment of the
requirements for the degree
of Doctor of Philosophy

August, 2022
St. Louis, Missouri

©2022, Yuewen Tan

Table of Contents

List of Figures

List of Tables

Acknowledgments

I am so fortunate to have been able to study in the physics graduate program at Washington University in St. Louis. Besides the endeavor of studying interesting research topics and pursuing the degree, the most valuable resource here for me has been the professors, graduate students, and undergraduate students, who are from diverse backgrounds, talented, and willing to share. The exchanges of thoughts or even a small talk might unconsciously reshape the way I think, and I have always appreciated that I could meet these people in my life.

First, I want to acknowledge my thesis advisor, Professor Tiezhi Zhang. He provided me with much resources, guidance and tremendous support in research. I learned many hands-on lab skills and detailed x-ray tube technologies from him. He was always very patient and constantly tried to inspire me. With his help, I gradually built up my confidence and became more independent in research.

I would like to thank my physics advisor Professor Erik Henriksen for his mentoring. He always cared about my academic progress, gave me advice, and encouraged me. I would also like to thank Professor Ryan Ogliore for his advice and encouragement during my mentoring committee meetings.

I would like to thank Professor Arash Darafsheh and Professor Thomas Mazur for their ideas and suggestions for my research projects. I would like to thank Professor Rao Khan for lending me his computer, which saved me a large amount of time. I want to thank Professor Lee Sobotka for his interest to be in my thesis defense committee and for giving me helpful suggestions.

I would like to thank my lab mates and colleagues: Praneeth Kandlakunta, Shuang Zhou, Qinghao Chen, and Ruirui Liu. They were extremely helpful when I tried to reach them for questions. They created a very comfortable and collaborative office environment that I would always like to stay in.

I want to sincerely thank all my friends who have made my graduate school life special.

Here I list a few of them: Kiandokht Amiri, Jesse Bagley, Thao Cao, Garv Chauhan, Menghan Chen, Sabrina Chen, Xinyuan Chen, Furqan Dar, Lei Fang, Kun Hao, Steven Harris, Jared Lalmansingh, Xunwei Liu, Qinghan Meng, Wei Miao, Weiyi Pan, Jufri Setianegara, Siera Stoen, Kainen Utt, Changqing Wang, Shixing Wang, Linhua Xu, Xinzhe Zhang, and Yuyue Zhao. There are tons of unforgettable and precious memories with them - I always remember when we were in classes, when we were traveling, when we were playing sports and video games, and when we were eating and drinking together. Even during the pandemic, we were bonded together and helping each other. I am so grateful to know all of them and to be their friend. In addition, I would like to thank my family friends Yi and Jiao who have supported me.

I want to thank my family: my grandparents, uncle Jiawei and Guishi, aunt Haihua and Bingzhe, and cousin Siyu and Yuge. We occasionally talked to each other remotely. I could always feel abundant love from them. I thank my partner Ji Xia and her parents for their support. Ji took great care of me and encouraged me when I sometimes was sad. Finally and most importantly, I thank my parents, mom Yimei and dad Jianong, for their unconditional love and support. They are the reason why I never give up. I have not seen them in person for more than three years, and I really miss them. Here I want to thank my parents for their understanding of my absence.

August, 2022
St. Louis, MO

ABSTRACT OF THE DISSERTATION

Distributed X-ray Sources for X-ray Imaging and Small Animal FLASH Irradiator

by

Yuewen Tan

Doctor of Philosophy in Physics

Washington University in St.Louis, 2022

Advisor: Professor Tiezhi Zhang

Emerging distributed x-ray source technology enables new designs for x-ray imaging systems. The multi-pixel thermionic emission X-ray (MPTEX) source, a distributed x-ray source developed in our lab, was assembled and tested. With a multi-row CdTe photon-counting detector, forty-eight x-ray fan beams of MPTEX source were able to cover a 25-cm cross-sectional and 8-cm axial field of view. Tetrahedron-beam x-ray imaging techniques using MPTEX source were demonstrated.

Ultra-high dose rate radiotherapy or FLASH radiotherapy (RT) potentially can reduce normal tissue toxicity in radiation treatments. A compact irradiator that can deliver FLASH-RT treatments similar to conventional RT treatments is needed for preclinical studies. Based on our MPTEX source, we designed and optimized a ring-shaped x-ray small animal FLASH irradiator (SAFI) with 51 focal spots. The dose rate characteristics in a 4-cm cylindrical water phantom and operating power limitations of SAFI were discussed. Forward and inverse treatment planning, as well as an inverse-geometry CT using the SAFI circular sources, were demonstrated.

The power of MPTEX sources with a fixed anode is limited by the focal spot power density. We optimized the design of tungsten(W)-diamond target and predicted its performance in MPTEX sources via Monte Carlo and finite-element analysis simulations. The maximum tube power and x-ray output intensities were predicted for both transmission and reflection target configurations. We showed a significant tube power and x-ray output enhancement when using a W-diamond target with the optimal W film thickness. Furthermore, a fabricated W-diamond sample was tested in an experimental x-ray tube. It can be potentially used in the next version of MPTEX source.

Chapter 1

Introduction

In the past two decades, distributed x-ray sources have been required for many novel x-ray imaging designs, such as x-ray tomosynthesis and inverse-geometry computed tomography (CT) [1, 2]. This dissertation presents the design of distributed x-ray source and its applications. For this chapter, as an introductory part of the dissertation, essential components of an x-ray tube and relevant background knowledge, including the principle of x-ray imaging and some basic concepts of the FLASH effect, will be reviewed.

1.1 Conventional X-ray Tubes

The discovery of x-rays by Wilhelm Röntgen in 1895 greatly advanced modern science and technologies [3]. Since their first discovery, the glass-tube vacuum envelope became an iconic feature of the device generating x-rays, and it was therefore named "x-ray tube" even if the glass tubes were replaced by chambers in later designs. Over these 127 years, the x-ray tube has been the most common and economical device to generate x-rays, especially for medical use.

1.1.1 A brief history

At the early stage of x-ray tube development, Crookes' ion tube design was quickly commercialized due to the mature incandescent light-bulb industry in the early 20th century.

Later in 1913, the design was replaced by Coolidge's invention at the labs of General Electric Research [4]. The design of using thermionic emission current from a hot tungsten filament revolutionized the tube market and provided stability and simplicity for x-ray production. To further increase the power of the x-ray tube, several physicists and inventors proposed and commercialized the rotating anode in 1929 [5, 6]. The exposure time of a radiography for medical use was largely reduced. The rotating anode design is effective and remains in current high-power diagnostic x-ray tubes. Other important improvements to the x-ray tube came much later in the 1980s and 1990s, including metal ceramics anode, liquid bearing technology, and back-scattered electron capturing. After there was a rapid growth in the computed tomography (CT) market, companies heavily invested in power enhancement of the x-ray tube. Rotating frame tubes and other powerful CT x-ray tubes were invented in the 2000s.

Future development of x-ray tubes in favor of higher temporal and spatial resolution will be predominantly driven by the healthcare applications, such as dose efficiency, spectral CT, contrast imaging, and others.

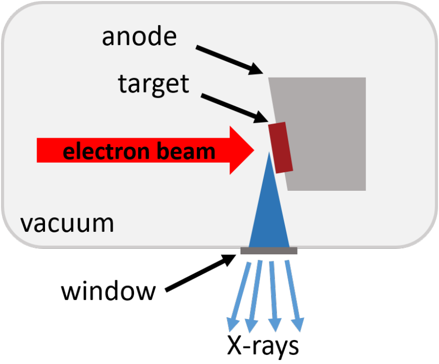

Fig. 1.1: Basic setup of an x-ray tube.

1.1.2 X-ray tube components

For medical imaging and treatment, the dominating processes of x-rays generation are deceleration and scatter of energetic electrons, when they penetrate into the target material and interact with the coulomb field of the surrounding nuclei and bounded electrons. Figure 1.1 demonstrates a basic setup of a conventional x-ray tube.

Comparing to other energy transferring processes in an x-ray tube system, the x-ray production is only a tiny fraction of the primary electron input energy. The power conversion distribution is illustrated in Table 1.1. For a 100 keV electron beam incident on a tungsten target, 39% of energy remains in the back-scattered electrons, 60% of energy is converted to heat in the tungsten, and left 1% energy is converted to photons through primarily Bremsstrahlung process. In this 1% radiative energy, only $\sim$3% of it comes out from the x-ray window, passes though the collimation, and reaches to the imaging object [3]. This number will be less if any further filtration is used to manipulate the spectrum. Therefore, the x-ray production in an x-ray tube is quite inefficient. However, this type of electron-impact Bremsstrahlung tube is also considered the most efficient and economical way of producing diagnostic x-rays [3]. When we work on the design of a diagnostic x-ray tube, we manipulate and optimize the tube design under scheme of the electron-impact system. A typical x-ray tube consists of a free electron source and an x-ray target. These two components are set up with a diode - cathode and anode - and operated in a vacuum environment.

Energetic 100 keV electron impact power conversion				
	Heat	Back-scattered electrons	Produced photons	
percentage	$\sim$60%	$\sim$39%	Used 0.03%	Others 0.97%

Tab. 1.1: The distribution of power conversion during 100 keV electron impact in a tungsten target. The electrons are perpendicularly incident on a flat tungsten surface. Only very little amount of x-rays (in the order of $\sim 10^{-4}$) will come out from the tube and be used in medical diagnostics [3].

Cathode

Through several physical mechanisms, free electrons can be generated from the cathode in an x-ray tube. The most common way is the thermionic emission of electrons from a hot cathode, which follows the Richardson's law of thermal excitation to overcome the work function of the cathode material (Equation 1.1). The thermionic emission current density can be expressed as

$$J = A_G T^2 e^{-\frac{W}{kT}}, \tag{1.1}$$

where T is the cathode surface temperature, W is the work function of cathode material, k is the Boltzmann's constant, and A_G is the generalized parameter that depends on the band-structure of emitting material. Thoriated tungsten filament (or a coil of thoriated tungsten wire) is the most common thermionic emitter in x-ray tubes [7]. During operation, it is directly heated to above 2000°C by an electric heating current in the order of few amps. The filament emitter is embedded in a cup structure made of metal, which can provide electron beam focusing. There are other lower work function cathode materials that are used in x-ray tubes, such as oxide-coated cathodes and Boride cathodes (LaB_6). The working temperatures for them are as low as 900°C. They require additional procedures in operation, and therefore are used only in specific x-ray tube applications and conditions [8, 9].

Another category of cathode emitter in x-ray tube is the carbon nanotube (CNT) field emitter, or also called the CNT cold cathode [10]. For this emitter, the electrons in the carbon nanotubes are pulled by a high electric field into the vacuum space. Comparing to the hot filament cathodes, field emitters reduce the heat generation in the x-ray tube. However, CNT-based cold cathodes are very sensitive to the operating environment, which reduces the robustness of this type of cathode. Now, the challenges of using CNT field emitter in x-ray tubes include ion attachment on tips, anode positive ion sputtering, mesh-grid electrode heating, and maximum emission current limitation [11]. Only a few low power medical imaging applications, such as tomosynthesis in mammography and miniature transmission x-ray tube, can be used with the CNT emitters [12, 13].

Anode and its heat management

Anode is the most crucial component that determines the tube performance. As illustrated in the previous section, over 50% of electron kinetic energy is converted to heat in the x-ray target and anode. Anode thermal management is the key task in x-ray generation. How heat is removed from the electron beam focal spot is always an important question to ask when designing an x-ray tube. In general, the heat deposited to the focal spot is transferred through diffusive process to the anode body, then transferred to the tube housing, and eventually dissipated to the environment.

Currently, x-ray tubes employ either stationary or rotating anode. The heat diffusion in both stationary and rotating anode target has been well studied and modelled [14, 15]. For the rotating anode, the maximum tube power is largely depending on the line-speed of the focal spot and is near a constant when the exposure time is ranged in 1μs to 0.1 s [3]. For the stationary anode, the maximum tube power dominates by the thermal properties of target, anode, and cooling liquid. In general, the tube power of rotating anode has 1-2 higher order of magnitude compared to stationary anode. In addition, even though there are other types of anode such as the liquid-jet target, they are far away from practice [16, 17].

1.1.3 X-ray production

There are primarily two physical mechanisms account for the x-ray generation in an x-ray tube. X-rays produced from these two processes are called Bremsstrahlung and characteristic x-rays. Bremsstrahlung originally means the "braking radiation". It is produced when a charged particle is decelerated or changing direction in the target material. The output spectrum of Bremsstrahlung is continuous and can be empirically described by the Kramer's formula, given as

$$I(\lambda)d\lambda = K\left(\frac{\lambda}{\lambda_{\min}} - 1\right)\frac{1}{\lambda^2}d\lambda \tag{1.2}$$

where λ is the produced Bremsstrahlung wavelength, I is its intensity, $\lambda_{\min}$ is the minimum wavelength of the produced photon corresponding to the largest Bremsstrahlung energy called "kilo-voltage peak (kVp)" and equal to the kinetic energy of incident electron, and K is a parameter related to the atomic number of target element. Characteristic x-rays are generated when an energetic particle ejects an inner shell electron in an atom and an outer shell electron fills in the inner shell energy level. The energy of the characteristic x-ray is the difference between outer and inner shell electron binding energies. An example of x-ray energy spectra is plotted in Figure 1.2. For the x-ray tube using tungsten target, lower energy characteristic x-rays are filtered by the tube housing and become negligible and merge into Bremsstrahlung. Thus, only the K-characteristic x-ray production appears on the spectrum.

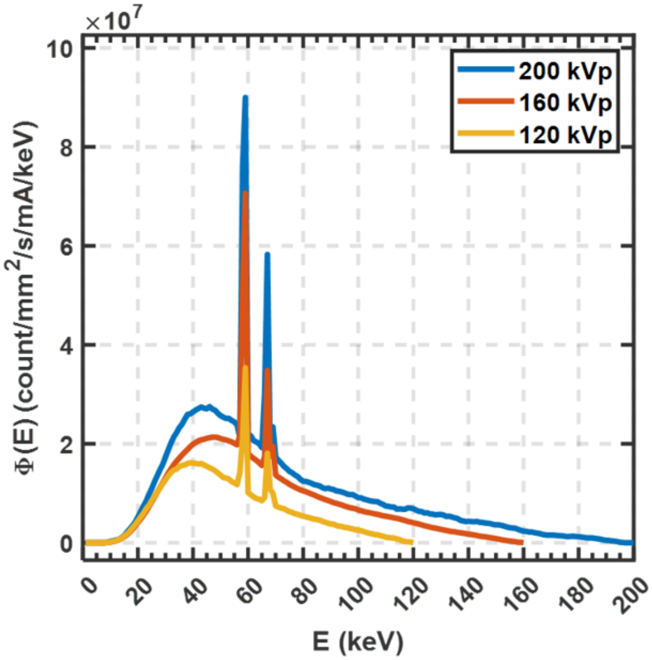

Fig. 1.2: Energy spectra of x-rays produced from a tungsten target using three different incident electron energies, resulting in three kilo-voltage peaks (kVp). The results are filtered by a 3-mm aluminum slab. The curves consist of the continuous Bremsstrahlung and discontinuous K-energy characteristic x-rays.

1.2 X-ray Imaging

1.2.1 X-ray projection radiography

X-rays interact with matter. For the x-rays produced from an x-ray tube (usually 35 - 140 kVp), three physical processes significantly contribute to the x-ray attenuation in matter.

They are elastic scattering (Rayleigh), inelastic scattering (Compton), and photoelectric effect. The attenuation of the x-ray beam passing through an object can be modelled as,

$$\ln\left(\frac{I_0(E)}{I(E)}\right) = \int_L \mu(E,x)dx \tag{1.3}$$

where $I_0(E)$ is the intensity of the incident x-rays of energy E $I(E)$ is the intensity of the transmitted x-rays, L indicates the path through the object, and $\mu(E,x)$ is the attenuation coefficient for photon energy E at location x. The coefficient $\mu(E,x)$ accounts for the three interactions, and have been tabulated by NIST for most of materials. This attenuation model is the essential of x-ray imaging, and this quantity is usually called the projection. The most traditional way of getting an x-ray image is to directly expose under an x-ray source and detect the projection. The variation of the structures inside the imaging object alters the projection intensities and forms an image.

1.2.2 Computed tomography (CT)

X-ray computed tomography is more sophisticated projection radiography. In a CT scan, the imaging object is measured its projections at multiple angles rotating in a same plane, and this set of data is called the sinogram.

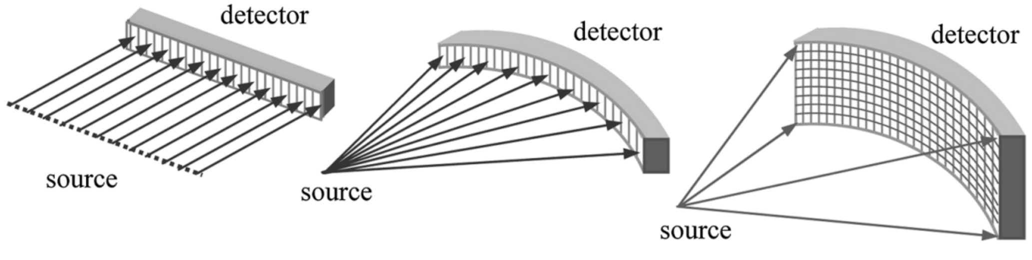

Fig. 1.3: Beam geometries in CT scan: (left) parallel beam, (middle) fan beam, and (right) cone beam.

An important component of a CT scan is its measuring geometry: parallel beam, fan beam, or cone beam. This geometry determines the reconstruction of the sinogram to the tomographic image. In Figure 1.3, three beam geometry are illustrated [18]. An example of the reconstructed image from a sinogram is shown in Figure 1.4. The reconstruction from measured projection sinogram to the original object is a major research topic in x-ray CT technologies.

A conventional way of reconstructing the image is call filtered back projection (FBP) algorithm. It takes advantage of the Fourier slice theorem, which states that x-ray projection measurement at each angle is equivalent as sampling of a slice in the 2-dimensional Fourier space of the object image. With weighting in the Fourier space, the tomographic image can be directly obtained by the inverse 2D Fourier transform. The FBP reconstruction algorithm has also been developed for fan beam and cone beam, and they have been used since the invention of CT scan.

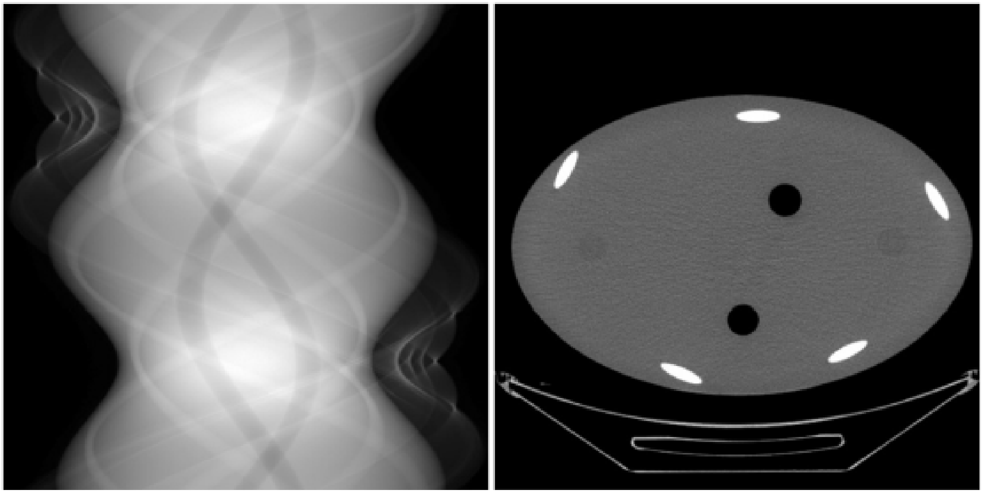

Fig. 1.4: An example of a sinogram and reconstructed object.

Another major reconstruction algorithm for CT is the iterative reconstruction, a numerical approach. The iterative reconstruction, or specifically model-based iterative reconstruction, is modelled under the framework of Bayesian inference by assuming that the noise in projection measurement is Poissonian. With a correct physical modelling of the projection, such that a transformation from a known object to the sinogram with noise, a log-likelihood function can be written for any given sinogram. There exists a material distribution of the object image that can maximize the posterior probability, and it will be the reconstructed image. Due to its high image quality, the iterative reconstruction has been used in many current major commercial CT scanners.

1.3 Distributed x-ray source imaging systems

The scanning-beam digital X-ray (SBDX) source is one of the earliest distributed x-ray sources. It scans an electron beam and generates a two-dimensional array of X-ray focal spots on a transmission target. An inverse-geometry X-ray fluoroscopy system has been developed with an SBDX source [19]. It can generate tomosynthesis images with unblurred images at selected depths. Due to the convergent beam geometry, the SBDX has a lower skin dose and thus is ideal for procedures that require long imaging time, such as cardiac catheterization [20, 21]. An inverse geometry CT has been developed with SBDX, but the limited focal spot array dimension does not provide sufficient field of view (FOV) coverage. Although multiple detectors can be used, the system design, especially the collimator, can be very complicated [22, 23].

Several linearly distributed x-ray sources with discrete electron sources have been developed later [24–26]. These linear x-ray sources generate a linear array of electron beam focal spots on a fixed elongated anode. An inverse geometry fan-beam CT system has been developed in which a long source array and a small detector array were used to cover the reconstruction field-of-view [27]. A major advantage of the inverse fan-beam CT is that each X-ray beam intensity can be dynamically modulated based on body shape so that the X-ray exposure can be optimized [2, 26]. However it would require a high tube power that cannot be achieved with the fixed anode tube design [26]. A multi-pixel field emission X-ray source has been developed with carbon nanotubes and has been used in digital tomosynthesis systems, in which the source scanning replaces the gantry rotation so that it eliminates blurring by source motion in conventional CT imaging [1, 28, 29].

1.4 FLASH Effect

The FLASH effect is also called the "ultra-high dose-rate effect". It is a radio-biological phenomenon triggered when the radiation dose rate is extremely higher than the conventional dose rate for radiotherapy. The ultrahigh dose rate threshold is usually defined as 40 Gy/s [30]. At ultrahigh dose rate, the radiation induces less toxicity to the normal tissue compared to at the conventional dose rate, while it treats the tumor as same as the conventional dose rate radiation.

1.4.1 Development of FLASH effect in Radiotherapy

Early high radiation dose rate studies demonstrated ubiquitous cell survival curves [31, 32]. Special mechanisms related to high dose rates are mysterious, while they did not bring much attention due to the extreme dose rate conditions. In 1978, a graduate student Anatoli Bugorski, who worked at the U-70 proton synchrotron facility in Protvino, accidentally stuck his head into the 76 GeV proton beamline while checking a malfunctioning part. The proton beam pulse was on and passed through Anatoli's head from the backside. He received thousands Gy of doses at the path in his head, which were considered to cause death. However, Anatoli survived and has lived as normal until now at the age of 79. This accident was not understood and defied radiobiological theories at that time [33]. After 35 years, the terminology "FLASH" for ultrahigh dose rate radiation first appeared in 2014 from a paper by Favaudon *et al.*, in which authors described the "FLASH" irradiation technique, known as using radiations with a mean dose rate greater than 40 Gy/s to treat lung tumor in mice. They showed that the FLASH irradiation surprisingly treated the tumor as effectively as the conventional dose-rate irradiation while having less toxicity to the normal tissues. What causes the discrepancy between the tumor and normal tissue reacting to the ultrahigh dose-rate radiation is a new mystery. This phenomenon brought great research interest, and numerous preclinical and clinical studies have started since then.

1.4.2 Radiation sources for FLASH studies

Achieving an ultrahigh dose rate irradiation requires high brightness of the radiation source. Instrumentation development plays an important role in FLASH studies. Since 2014, ultrahigh dose rate radiation for FLASH effect studies has been realized using electrons generated by clinical linear accelerators (linacs), biomedical synchrotron radiation, protons generated by cyclotrons, and kV x-rays from conventional X-ray tubes [34]. There are also other novel designs to achieve the FLASH requirement. Selected FLASH radiation sources are summarized in the following table (Table 1.2, partly adapted from Darafsheh 2021 [35]).

The FLASH effect has promising future applications and might revolutionize the standards of radiotherapy. However, there are still many questions related to the FLASH effect. Even though the first human FLASH radiotherapy treatment was done in 2019, many more preclinical studies need to be done before the FLASH radiotherapy techniques are eventually translated to the clinical settings.

Year	Ref	Type	Machine	E (MeV)	$\bar{\dot{D}}$ (Gy/s)	$\dot{D}$ (Gy/s)	D_p (Gy)	Purpose
2014	[30]	electron	Kinetron linac	4	$0.03 \sim 750$	5.0×10^6	60	mouse study
2017	[36]	electron	Oriatron 6e linac & Kinetron	6 & 4.5	$0.1 \sim 500$	5.6×10^6	10	mouse study
2017	[37]	electron	Varian Clinac 21EX	9 & 20	74&22, 900	8.2×10^4	–	dosimetry
2017	[38]	electron	Oriatron eRT6	5 - 6	200	4.5×10^6	2.2	platform development
2018	[39]	photon	ESRF ID17 bio beamline	0.102	37	1.2×10^4	N/A	mouse study
2018	[40]	proton	IBA isochronous cyclotron	138 - 198	40	N/A	N/A	dosimetry
2019	[41]	electron	Elekta precise clinical linac	8	$30 \sim 1000$	–	–	dosimetry
2019	[42]	electron	Oriatron 6e linac & Kinetron	6 & 4.5	300	–	–	mini pig & cat
2019	[43]	electron	Oriatron eRT6	5.6	150	1.5×10^6	1.5	human patient
2019	[44]	proton	Varian isochronous cyclotron	245	40	N/A	N/A	mouse study
2019	[45]	electron	Varian Clinac 21EX	16 & 20	300 & 200	8.8×10^5	1.75	mouse study
2019	[46]	photon	MXR-160/22&165 x-ray tubes	~0.06	~ 160	N/A	N/A	feasibility study
2020	[47]	proton	IBA isochronous cyclotron	230	78	N/A	N/A	mouse study
2020	[35]	proton	Mevion synchrocyclotron	70	$100 \sim 200$	1.6×10^4	0.32	feasibility study
2020	[48]	electron	Oriatron 6e linac	6.0	200	7.4×10^5	1.33	mouse study
2020	[49]	electron	Kinetron linac	4.5	100	N/A	N/A	mouse study
2021	[50]	photon	RAD-44&G-1592 x-ray tubes	~0.06	140	N/A	N/A	feasibility study
2021	[51]	photon	PARTNER platform	6.0	$700 \sim 1200$	N/A	N/A	platform development
2022	[52]	photon	SAFI system	~0.06	$120 \sim 500$	N/A	N/A	platform design

Tab. 1.2: Radiation sources that were used in the FLASH effect research. The particle energies E, the maximum mean dose rates $\bar{\dot{D}}$, the maximum instantaneous dose rate $\dot{D}$, and dose per pulse D_p, were specified. "–" signs indicate that the values were not specified in the reference articles.

1.5 Overview

In Chapter 2, technological details of multi-pixel thermionic emission x-ray (MPTEX) source are discussed, including the design of the MPTEX tube, its operation, and its tube parameters. Chapter 3 is an introduction of the imaging application of MPTEX source, the tetrahedron-beam (TB) x-ray imaging. The imaging data acquisition and imaging results are shown. In Chapter 4, a newly proposed FLASH irradiator for preclinical studies based on MPTEX is presented. Its design and the capability of delivering planned FLASH radiations are discussed. An associated imaging system of the irradiator is also demonstrated. Chapter 5 exhibits the study of thin-film tungsten(W)-diamond x-ray target, a novel x-ray target that can potentially increase the x-ray tube power. It will be especially useful for the distributed x-ray source using fixed anode. The analysis of the optimized W-diamond design and how they will be used in various tube conditions are particularly addressed. Finally in Chapter 6, this dissertation is concluded, and contributions are summarized.

Chapter 2

Multi-pixel Thermionic Emission X-ray (MPTEX) Source

In this chapter, the multi-pixel thermionic emission x-ray (MPTEX) source, a distributed x-ray source developed in our lab, is introduced. The MPTEX source has a linear or circular array x-ray focal spots that can be employed in the Tetrahedron Beam CT and the Small Animal FLASH Irridator (SAFI) that will be introduced in Chapter 3 and 4, respectively.

2.1 Source Design and Beam Control

Similar to a conventional x-ray source, the multi-pixel thermionic x-ray (MPTEX) source employs electron-impact design in x-ray production. It consists of an array of cathodes, focusing electrodes, mesh grid and a an elongated anode, which is connected to the high voltage.

2.1.1 Oxide-coated cathodes

The thermionic cathode is a mature electron source technology that can provide a larger current density than field emission cathodes. The oxide-coated cathodes were developed using a high-density alkaline earth metal carbonate mixture coated on the nickel-substrate metal substrate (Figure 2.1). The triple carbonate cathode coating (Transene Company, Danvers, MA, USA) is a mixture of homogenous crystalline carbonates of barium (Ba), strontium (Sr) and calcium (Ca) (56% $BaCO_3$, 31% $SrCO_3$, and 13% $CaCO_3$) with an isomorphous crystal structure dispersed in a lacquer vehicle containing an ethyl cellulose binder.

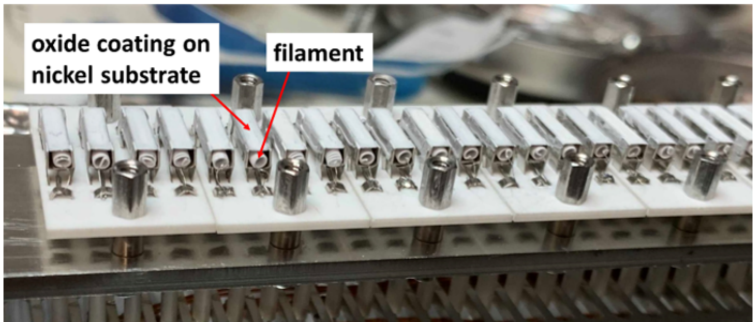

Fig. 2.1: The oxide-coated cathodes assembly of MPTEX source. The coating was painted on 48 nickel substrates, each with a heater filament attached to the back.

The coating was manually applied on 48 nickel substrates. The cathodes were heated by a tungsten filament heater attached to the back, as shown in Figure 2.1. The heaters (Union City Filament, Ridgefield, New Jersey, USA) were made of 0.0045-inch diameter tungsten wires and had resistances of about 2 Ω at room temperature. The filament heater had helical shape and was coated with alumina. The heater was powered by AC electric power directly from a transformer. The heating power of each filament was 6 - 8 Watts, and the operation temperature reached 700 - 900 °C. Figure 2.1 is a complete assembly with oxide coating, and Figure 2.2 shows some components for the assembly. The temperature was estimated based on the change in tungsten's resistivity. After being mounted in the tube, the cathodes were activated at temperatures up to 1000 °C. Though higher currents (>50 mA) had been achieved, the emission currents used for imaging were usually 10 - 20 mA (50 - 100 mA/cm^2 cathode emission current density) to avoid overheating and melting the tungsten target on the fixed anode. As a precaution against cracking in the coatings, the cathodes were heated slowly to the target temperature without overheating them. Exposure to the air, especially oxygen and carbon dioxide, will cause poisoning to the coatings, which produces a decrease in emission current density. To avoid the poisoning effect, the cathodes were kept at a vacuum level of 10^{-4} Torr when not in use.

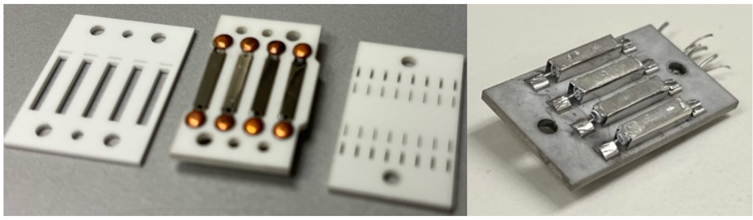

Fig. 2.2: Some ceramic components of cathode assembly (left) and an assembly of four cathodes without coating (right).

Compared to traditional tungsten filament cathodes, oxide-coated cathodes work at a lower temperature and have a higher emission efficiency, which is defined as the total emission current per watt of heating power. Because oxides of alkaline earth metals such as barium have low work functions for electron emission, they can operate at a lower temperature (∼800 °C) than traditional tungsten filament (∼2200 °C) and thus require less heating power [8]. In addition, oxide cathodes were reported to have a lifetime of over 5000 hours with an emission current density of 2.1 A/cm^2 at 800 °C [53]. Therefore, oxide-coated cathodes were chosen as the electron sources of the MPTEX source [25, 54].

2.1.2 Electron beam control and focusing

The MPTEX source employed a triode electron gun design with a grounded tungsten mesh grid and an elongated anode with tungsten target. The anode was connected to a positive high voltage power supply (STR120; Spellman High Voltage Electronics Corporation, Hauppauge, NY, USA). The tube controller provides positive or negative bias voltages to the cathodes via fast metal-oxide-semiconductor field-effect transistor (MOSFET) switches. As shown in Figure 2.3 and 2.4, when a cathode was negatively biased, electrons were accelerated to the mesh and, and they partially passed through the mesh grid and bombarded the focal spot at corresponding locations. When a cathode was positively biased, the electrons remains at the cathode's surface.

All 48 cathodes were assembled in a compact triode array (Figure 2.4). The heater

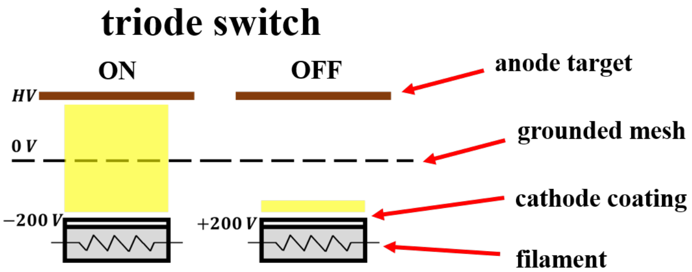

Fig. 2.3: Schematic diagram of triode electron beam control design for the oxide-coated cathode in MPTEX. The ON and OFF state correspond to the negatively and positively biased cathode voltage.

filaments were powered using an AC source controlled by a variable transformer. The cathode was connected to one side of the heater filament. One cathode corresponds to one channel and was controlled by a complementary metal-oxide semiconductor (CMOS) switching circuit which enabled the ON/OFF of emission current powered by a DC voltage source. Every eight cathodes were controlled by one CMOS channel selecting and switching board, and there are total 6 boards for 48 cathodes (Figure 2.5).

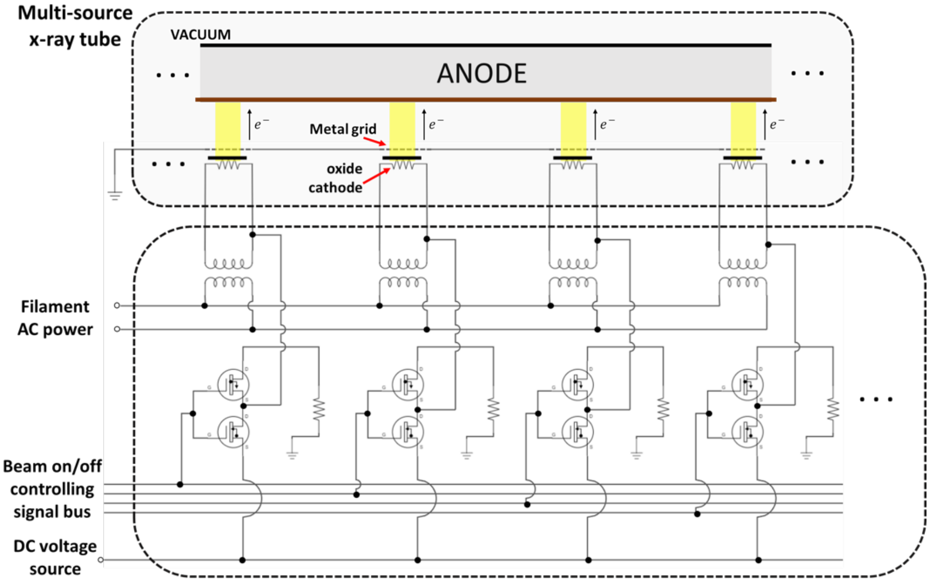

Fig. 2.4: Functional diagram of MPTEX source (only 4 cathodes are shown). The tube controller provides positive or negative bias voltages to the cathodes via CMOS switches. When a cathode is negative biased, electrons will pass through the mesh grid and bombard the focal spot.

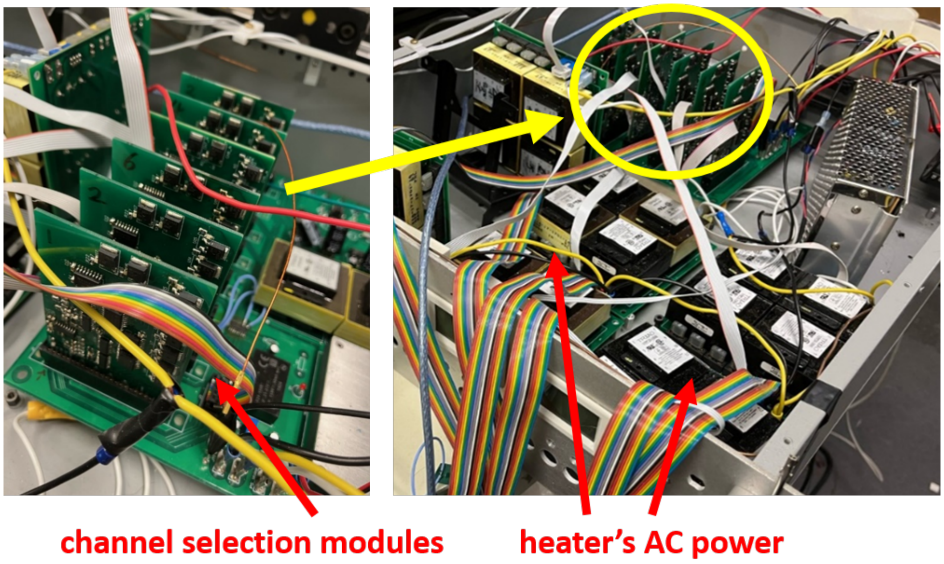

Fig. 2.5: Electronics for the beam control, including 6 channel selection boards (each board controls 8 channels) and the heater's AC power supply.

The grounded electrode attached to the mesh was shaped to form a focusing electric field for both dimensions of the cathodes. The focusing optics were designed using the charged-particle-tracing module of a finite-element simulation software (COMSOL, Inc., Burlington, MA). The designed electric field focusing can confine the electron beam to a small focal spot, as shown in Figure 2.6. The rise and fall times of the beam extraction voltage are approximately 1 μs. The total source array length is 188 mm, with a total of 48 source pixels spaced 4 mm apart. The electron optics design is shown in Figure 1b. A beam begins as the electrons are extracted from the cathode when the cathode is negatively biased. A portion of the electrons will hit the mesh grid, while the remainder will pass through it and enter the focusing electric field. We employed electrostatic lenses that produce the focusing electric fields under the high voltage of the tube, steering and focusing the 2×10 mm^2 electron beams to small focal spots on the target surface. In Figure 2.6, the focusing optics consist of two parts. The first part focuses the beam in the 2-mm width direction, and the second part focuses it in the 10-mm length direction. Both the focusing electrodes and the mesh grid are grounded. In this design, the bias voltage between the cathode and the grid was ±200 V. A change in high voltage alters the focusing electric fields, resulting in a small change in focal spot size, but the change is insignificant within 70 - 90 kV anode voltage.

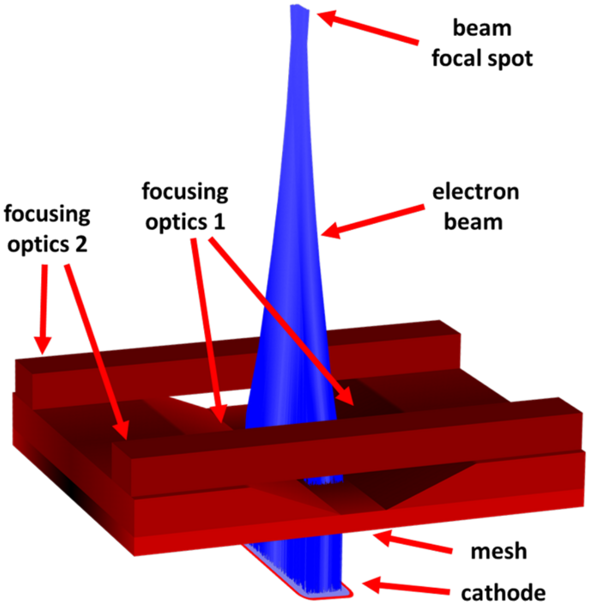

Fig. 2.6: Focusing optics design in width and length direction of the cathode. Electrons are extracted when the cathode is negatively biased. After passing through the mesh grid, the electrons are confined by the focusing electric field to a focal spot on the anode surface.

MPTEX tube assembly

The MPTEX tube was assembled in our lab. The MPTEX tube consists of three major components: an aluminum vacuum chamber, 48 oxide-coated cathodes' assembly, and an elongated tungsten target on a copper anode. The anode was installed inside the vacuum chamber and electrically isolated to the tube housing by a pair of ceramic spacer. The anode was connected to the high voltages via a high voltage feed-through. The cathode assembly (Figure 2.1) was slotted in to a vacuum chamber. The oxide cathodes and mesh faced to a tungsten target with designed distance. The completed MPTEX prototype tube assembly is shown in Figure 2.7. Both front and side view are demonstrated.

The tube body was grounded to the high voltage power chassis. The tube body was water-cooled, and a commercial liquid cooling kit (EK-KIT X240, EK, Komenda, Slovenia) was used to dissipate the heat into the air. Hot water leaving the tube was cooled through the radiator with fans before it was pumped back into the tube again. They are shown in Figure 2.7 (side view).

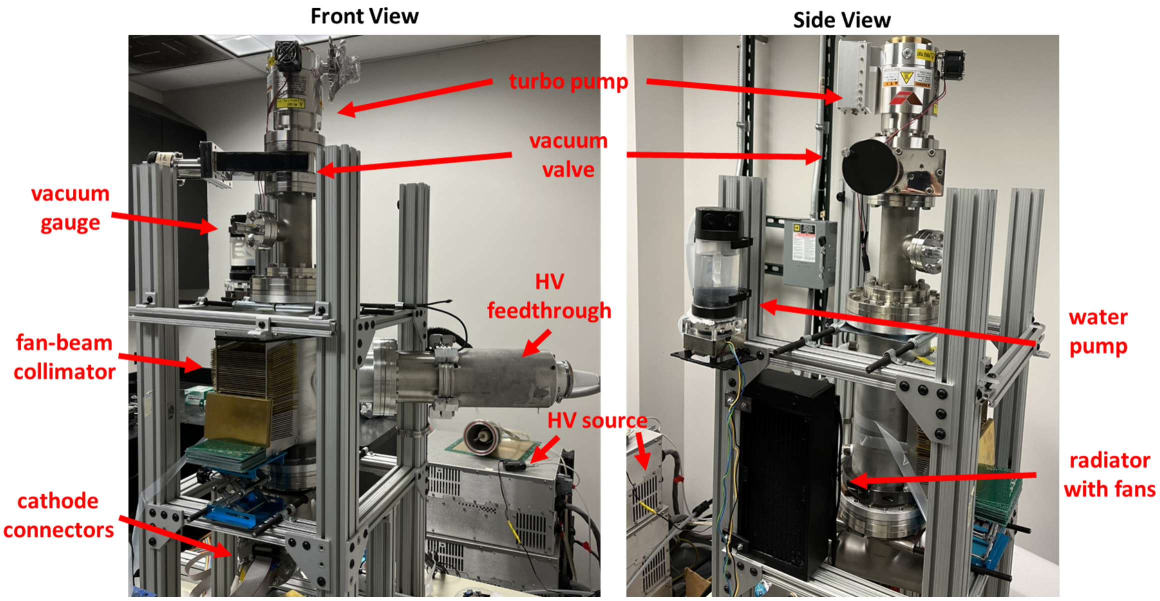

Fig. 2.7: The MPTEX prototype tube assembly in lab.

2.2 Tube Preparation and Operation

Conditioning of vacuum environment

Before tube can be operated at high voltage, the tube conditioning is necessary to reduce the frequency of vacuum discharges (arcing). The tube was maintained at lower anode voltage, and the voltage gradually ramped up. At each voltage, ten low mA exposures (1 mA and 100 ms for each exposure) was turned on for each source. Then we raised the anode voltage by 1 kV to the next step. This process was repeated for each step until the desired voltage was reached. Whenever a vacuum arcing occurred in the tube, the anode voltage was lowered by 3 kV. A newly installed x-ray tube usually takes more than one day to condition. The tube also requires conditioning after an inactive period. After the high voltage conditioning, the MPTEX source could maintain at 100 kV anode voltage. However, the tube regular operating anode voltage was usually between 70 and 90 kV to reduce possibility of arcing.

Activation of oxide-coated cathodes

The activation procedure involves the heating of the oxide cathode in high vacuum to cause the decomposition of carbonates into oxides and production of free Ba in the resultant oxide coating that allows the high electron emission at a given cathode temperature. The activation process only needs to be performed once. After activation, the oxide cathodes need to be kept in vacuum and cannot be exposed to air [25].

All 48 cathodes were activated one by one before regular use. During the activation of each oxide cathode, the vacuum chamber was first evacuated to a pressure below 1×10^{-6} Torr which was monitored with a vacuum gauge. The heater attached to the coated cathode was powered by a variable transformer. When started activation, the heating power was slowly ramped up. The chemical equations below describe the reactions during the conversion of carbonates to oxides.

$$\mathrm{BaCO_3} \rightarrow \mathrm{BaO} + \mathrm{CO_2} \uparrow$$

$$\mathrm{CaCO_3} \rightarrow \mathrm{CaO} + \mathrm{CO_2} \uparrow$$

$$\mathrm{SrCO_3} \rightarrow \mathrm{SrO} + \mathrm{CO_2} \uparrow$$

The breakdown of carbonates was accompanied by a sharp rise in the vacuum pressure due to the out-gassing of the heated carbonate. However, the vacuum pressure was maintained under 1×10^{-5} Torr. The complete breakdown of the carbonates and conversion to oxides was indicated by a sudden drop in the vacuum pressure. A further increase in heater temperature resulted in the reduction of Ba oxide in the cathode coating to free Ba. The free Ba formed at the oxide coating-nickel interface disperses uniformly to form an active cathode structure. In each subsequent operation, the oxide cathode is heated to its operating temperature (∼800 °C) to produce electron emission from free Ba formed in the oxide coating.

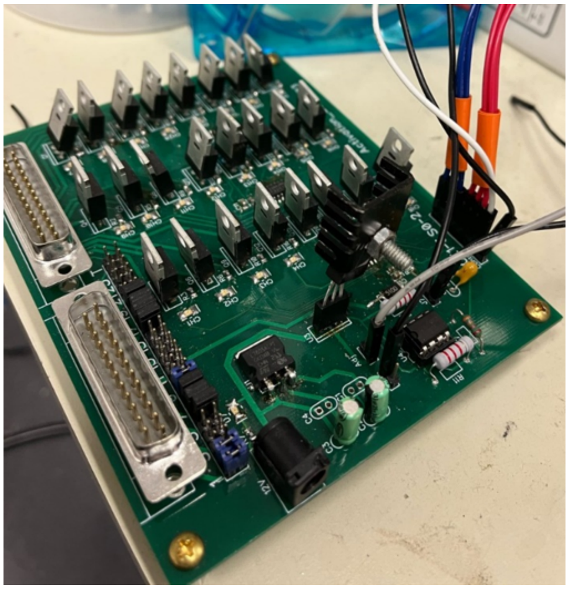

Fig. 2.8: The automatic activation device that can perform the activation process for 24 cathodes, one at each time.

The activation process for each cathode usually takes more than an hour, meaning that it would take at least two whole days to get all 48 cathodes activated. Manually activating all cathodes might take more than a week. Thus, we developed a DC powered activation device (Figure 2.8) to perform the activation automatically. This device was controlled by the signals generated from an NI-DAQ USB-6008 device. The board can select single cathode via one of the metal-oxide semiconductor field-effect transistor (MOSFET) channel, and it can alter the DC source up to 1 amp.

2.3 Discussion

This chapter introduced the design of our MPTEX source prototype based on the oxide-coated cathode and beam control. The oxide-coated cathode's thermionic emission current is significantly greater than the field-emission cathodes with a much lower cathode-gate voltage (< 100 V) [29]. MPTEX source has significantly higher tube power in a compact vacuum envelope design, and it is compatible for many high power applications, such as tetrahedron-beam imaging and high power irradiator discussed in later chapters.

The MPTEX source employed a fixed tungsten anode. Although the MPTEX source allows higher tube power than single focal spot X-ray source with a fixed anode by allowing the focal spots to cool down during the scan, its power is still lower than the rotating anode that can spread the heat to a larger focal spot track. Although not impossible, the development of a linear array X-ray source with a rotating anode would be very challenging. Therefore, the maximum available focal spot power density is the power-limiting factor for the MPTEX source. The maximum focal spot power density depends on the thermal properties of the target, such as the thermal conductivity of tungsten for the continuous electron beam. In pulse mode, much higher power can be achieved by using shorter pulse duration and quickly switching to the next source. In this way, it is effectively enlarge the focal spot area like rotating anode. The maximum power is eventually limited by the pulse duration, which relies on the switching electronics and the detector dwell time if it's used for an imaging application.

To further increase the power limitation of the fixed anode that is used in distributed x-ray source, we proposed a high-power composite target design for this type of multiple focal spot source, and its design and optimization will be discussed in Chapter 5.

Chapter 3

Tetrahedron-Beam X-ray Imaging Based on MPTEX Source

A tetrahedron-beam (TB) X-ray imaging system with a linear distributed X-ray source and a linear detector array positioned orthogonal to each other may overcome the X-ray scattering problem of traditional cone-beam X-ray systems. This Chapter describes the TB imaging benchtop system developed in our lab and its performance.

3.1 Motivation

Traditional X-ray systems with a point X-ray source and two-dimensional detector involve a large number of scattered photons. The advancement in distributed X-ray source technology allows new X-ray imaging system designs that may overcome the inherent problems due to the broad beam geometry.

Cone beam CT (CBCT) is an important imaging modality for image-guided intervention (IGI) and point-of-care diagnostic imaging. The high scatter-to-primary ratio (SPR) is a major problem of CBCT with flat panel imagers (FPIs). Mentioned in earlier paragraphs, Tetrahedron beam CT (TBCT) comprises a linear array of x-ray sources and a linear array detector positioned orthogonal to each other [55]. The axial coverage is achieved by scanning a stack of narrowly collimated fan beams. The low SPR and the use of high-quality discrete

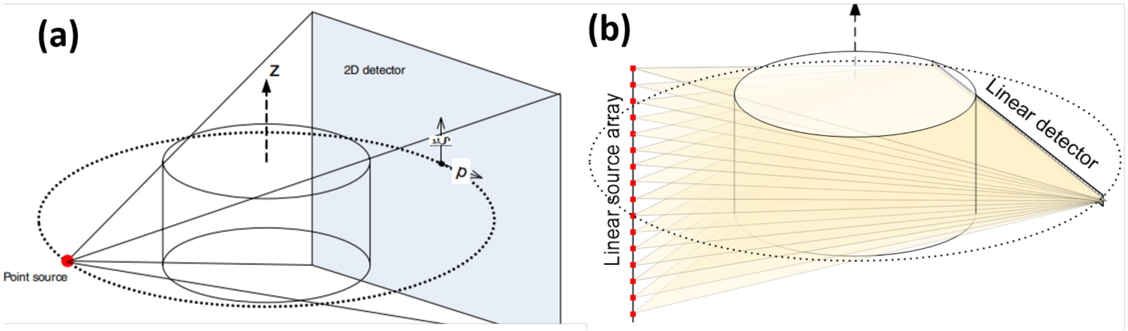

Fig. 3.1: (a) Cone-beam geometry. (b) Tetrahedron-beam (fan-beam) geometry.

CT detectors allow TBCT to achieve comparable image quality as diagnostic helical CT. Similar to CBCT, TBCT can be easily mounted on a linac or a C-arm gantries for IGI and image-guided radiotherapy (IGRT) [56]. A comparison between CBCT and TBCT geometries is shown in Figure 3.1. Besides volumetric CT, real-time imaging by fluoroscopy is also frequently used in IGI and IGRT procedures. TBCT may also perform fluoroscopic imaging by sequentially scanning the source array. Our lab developed a TBCT benchtop system with our multi-pixel thermionic emission X-ray (MPTEX) source and a photon-counting detector.

3.2 TB Imaging System Design

The TB imaging system employs the multi-pixel thermionic emission x-ray (MPTEX) source that we developed, which comprises 48 x-ray sources with 4 mm spacing on a linear array. Sections in Chapter 2 described its design and operation procedure. Before using it in the TB imaging, the MPTEX source was activated and tested.

A specially made multi-slot collimator was used to collimate the x-ray beams into 48 fan beams that were received by the linear detector array. Figure 3.2 shows the diagram and picture of the multi-slot collimator. It was designed using a computer aided design (CAD) software based on the system geometry. Brass plates were positioned between the consecutive beams to form narrow beams. Each plate was wide enough, and no x-rays can cross multiple slot openings.

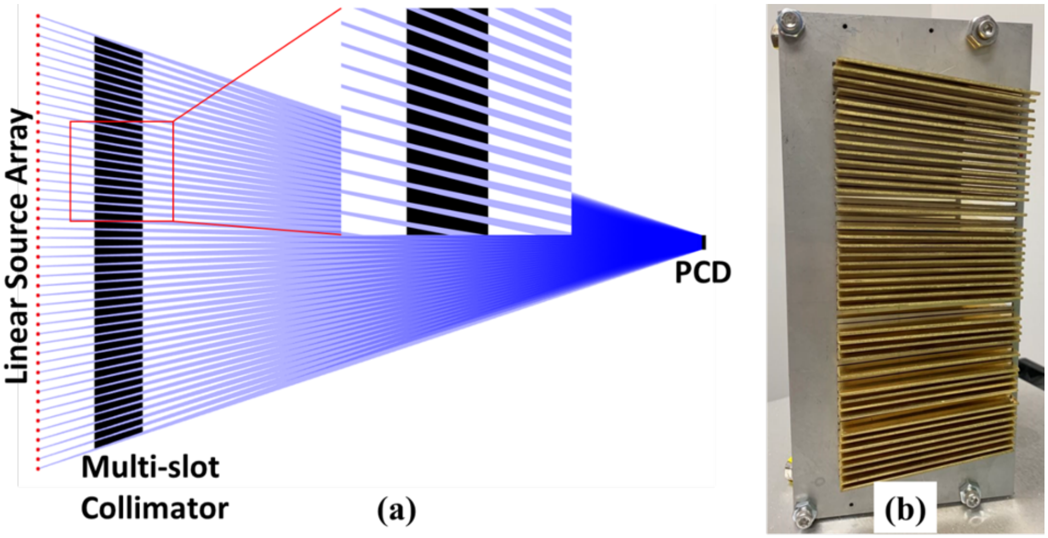

Fig. 3.2: Diagram (a) and picture (b) of the multi-slot collimator for TB imaging system. The X-ray beams were collimated into a stack of fan beams with different slant angles and received by a linear array detector after passing through the imaged object.

A commercial 60-row cadmium telluride (CdTe) photon-counting detector (PCD, XC-TDI350, Direct Conversion AB, Danderyd, Sweden) was used for the x-ray detection. The PCD has 60 × 3584 detector pixels with a pixel size of 0.1 mm × 0.1 mm. It has two energy bins that can be used for dual-energy imaging. During measurement, we set the low and high energy thresholds at 30 and 45 keV for 70 kV tube voltage, 30 and 50 keV for 80 kV tube voltage. The imaging FOV of a traditional cone-beam X-ray system is determined by the detector width and height. A TB x-ray system achieves its FOV coverage by the source length and detector length jointly. A TB imaging system in principle may employ a similar multi-row energy integration or PCD array used by diagnostic CT. Figure 3.3 (a) shows the actual TB benchtop imaging system with the MPTEX source, multi-slot collimator and PCD. Because the MPTEX is still in the development stage, it used an open chamber design so that its components can be replaced. The vacuum pressure was maintained uner 10^{-6} Torr by a 60 Liters/sec turbomolecular pump (TG60F; Osaka Vacuum, Nabari, Japan). The source-to-axis distance (SAD) and source-to-detector distance (SDD) were 500 and 700 mm,

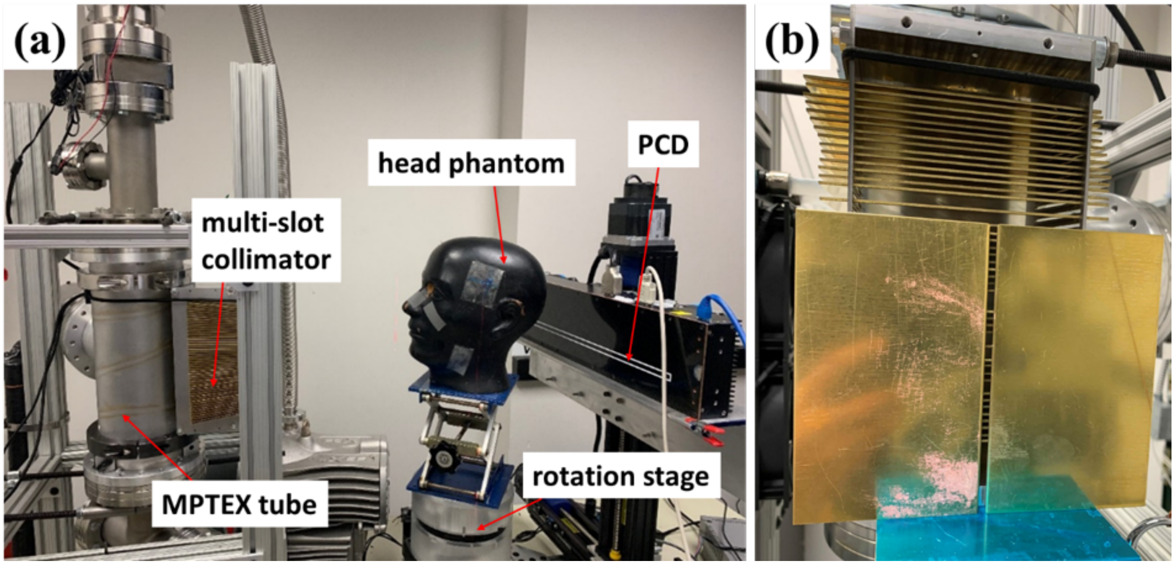

Fig. 3.3: (a) TBCT benchtop with an in-house developed multi-pixel thermionic emission X-ray (MPTEX) source, a multi-slot collimator, ahead phantom, and a commercial photon-counting detector (PCD). The MPTEX source generates 48 X-ray beams that are collimated by the multi-slot collimator. (b) The brass collimator that was used in the scatter-to-primary ratio (SPR) measurement to produce a pencil beam. This second collimator was made of five brass plates on each side, forming a slit.

respectively. The PCD and rotation stage were mounted on motorized translation stage for precise positioning. The system was aligned with better than 0.1 mm precision.

3.3 Source-Scanning Operation and Imaging Data Collection

Shown in Figure 3.4, a field-programmable gate array (FPGA) device was used to control the beam scanning and PCD data acquisition. The FPGA was also used to control the rotation stage for TBCT scans and activate each source with precisely controlled dwell duration. The workflow is summarized in the Figure 3.4 (a). The lab computer sent signals to the FPGA (0). It turned one of 48 x-ray beams on (1), triggered the PCD to collect photon counts for given time (2), transferred the photon-counting projection data to the lab computer (4), and then switched to another x-ray beam (1). After all 48 x-ray beam source were turned on and projection data were collected, the rotation stage was shifted one CT step angle (3).

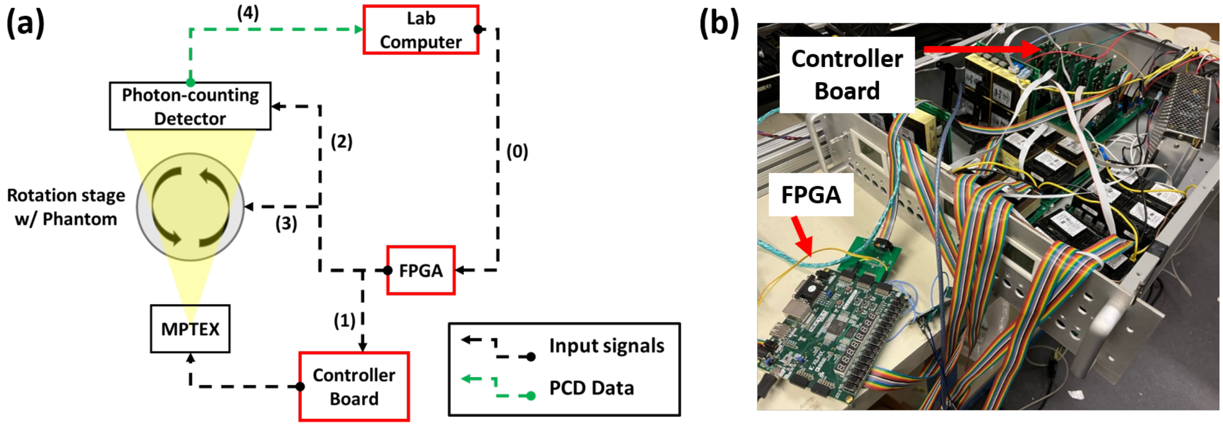

Fig. 3.4: (a) Schematic diagram with signal flow and data acquisition. (b) Image of the FPGA board connected to the controller board of MPTEX source.

We scanned the 48 source pixels sequentially at each CT angle, and the 48 image frames acquired by the PCD were transferred to the computer for image reconstruction. The PCD was run at its maximum frame rate of 150 frame per second (fps), translating to 6.67 ms for each frame window. A typical TBCT scan with 200 mAs exposure and 720 projections yielded 0.277 mAs exposure in each projection. With 15 mA emission current, the exposure time for each source in each projection was 0.277 mAs/15 mA = 18.5 ms. Given that the frame window is 6.67 ms at 150 fps frame rate, three frames were needed for the 18.5 ms exposure time. During each frame, the beam was on for 18.5 ms/3 = 6.17 ms and then off for the remaining 0.5 ms. These three frames were not arranged successively but rather divided into three scanning cycles to prevent overheating the target. The 48 sources were turned on sequentially during each scanning cycle, with 0.5-ms intervals between pulses. Thus, each projection took three cycles (144 pulses in total), and the entire imaging process took 2160 cycles. The timing was precisely controlled by the FPGA, and the tube controller could work synchronously with the PCD.

SPR quantification

Due to the collimated narrow fan-beam geometry, the SPR of the TB imaging system is expected to be considerably lower than the traditional cone beam system. The SPR measurement was carried out in the presence of a head phantom as shown in Figure 3.3 (a). The head phantom was adjusted to the height when its teeth were at the same level as the detector. In Figure 3.3 (b), another brass collimator was placed in front of the multi-slot collimator to further collimate the fan beam to a pencil beam. This second collimator was simply made of 5 brass plates on each side, forming a slit, and was used only when pencil beams were needed. When the pencil beam x-rays was on, a small area of the detector pixels was exposed to the x-rays, and the detector recorded the primary radiation after passing through the head phantom. The photon counts recorded by the detector pixels illuminated by the pencil beam was considered as the primary x-ray. The beam was broadened to form a fan beam by removing the pencil beam collimator. The photon counts in the detector were considered as the "primary and scattered" x-rays of the TB (fan) beam. Finally, the multi-slot collimator was removed, and the head phantom was exposed to full size x-ray beam. Under this circumstance, the measured SPR would be equivalent to a cone-beam system.

Figure 3.5 shows the distribution of x-ray counts over a detector row exposed to the pencil beam, fan beam, and cone beam. The air curve is also shown, which was obtained when no object was presented. The tube voltage was set to be 70 kVp and the high energy threshold of the PCD was 45 keV. Therefore, the detector counts represented the x-rays with energy between 45 and 70 keV. In order to correct the x-ray flux fluctuations in different beams, the counts were normalized according to the counts recorded in an isolated detector area where no scattered x-ray from the phantom can be detected. The counts of the three beams in the evaluation zone have three different levels, caused by different scatter components. The counts of the cone-beam x-rays are notably larger than that of the pencil-beam x-rays while the counts of the fan-beam x-rays are very close to the pencil-beam count, which indicates that the x-ray scattering of tetrahedron (fan) beam x-rays was at a much lower level than

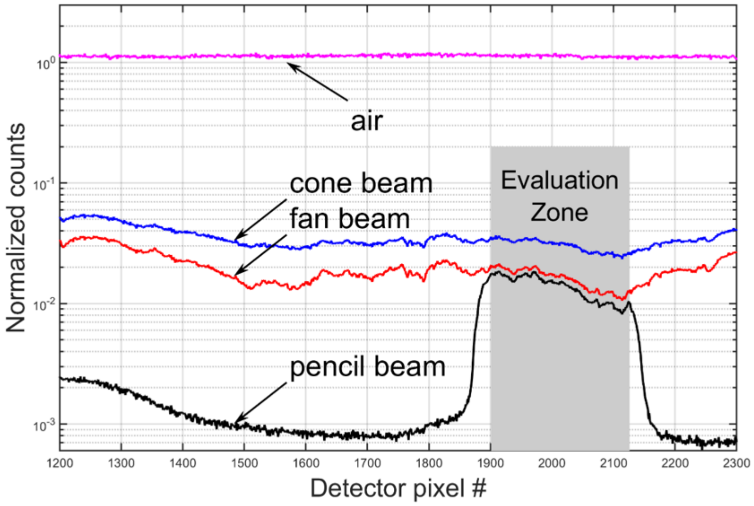

Fig. 3.5: The normalized x-ray counts over pixels radiated by the pencil-beam, fan-beam, and cone-beam x-rays. Pixel #1901-2126 was selected to be the evaluation zone where the SPR was calculated. Quantitative evaluation of the counts within the evaluation zone showed the mean SPRs were roughly 120% for the cone beam and 17% for the tetrahedron (fan) beam.

that of cone-beam x-rays. Quantitative evaluation of the counts within the evaluation zone showed the mean SPRs were roughly 120% for the cone beam and 17% for the tetrahedron (fan) beam.

3.4 TB imaging results

2D planar radiography

A sequential scan of the 48 sources generates 48 frames of 2D images P_i by the PCD in the dimension of 60×3584 image matrix where i is the source index. These images cannot be tiled together to form a 2D image because of the various divergence of the beams. Instead, they were digitally synthesized using a shift-and-add method [56].

To demonstrate this 2D imaging method, a star resolution pattern and a head phantom were used to get the 2D radiographic images. They were both scanned by the 48 sources sequentially, resulting in 48 projection images, which can then be combined by the shift-and-add method to create 2D radiographic images. The star resolution pattern (shown in Figure 3.6), with a diameter of 45 mm and spoke angles of 1.5°, was made of Pb with a thickness of 0.03 mm. The head phantom was the same one shown in Figure 3.3. The exposures for the star pattern and the head phantom are 1 mAs and 5 mAs respectively.

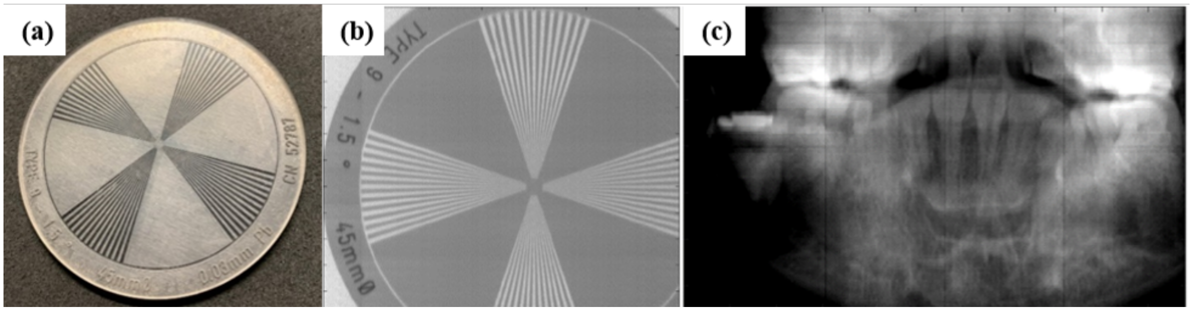

Fig. 3.6: The star resolution pattern (a) and its digitally synthesized 2D image (b), and the synthesized 2D image (c) of the head phantom shown in Figure 3.3 (a).

The star resolution pattern image can be further used to measure the focal spot size of the x-ray tube [57]. As the spoke width decreases along the radial direction from periphery to center, the gaps in the image start to blur at some diameter D due to the penumbras of the spokes. The focal spot size can be determined by

$$f = 2d \cdot \frac{M}{M-1}, \tag{3.1}$$

where d is the spoke width at which the image starts to blur, M is the magnification factor, i.e. the ratio of SDD to source-to-pattern distance. For the star pattern, blurring spoke width d can be estimated by measuring the blurring diameter.

The blurring diameter in Figure 3.6 (b) is 7.2 mm, which yields a blurring spoke width d of 0.19 mm. With a magnification factor $M = 4$, the focal spot size can be calculated according to the Equation 3.1. Based on Figure 3.6 (b) and the Equation 3.1, the focal spot size were measured about 0.5 mm. The 2D radiographic image in Figure 3.6 (b) is formed by the 48 projections of the 48 sources, and we assume the MPTEX sources have similar focal spot sizes since the electron optics designs are the same. Therefore, the size of 0.5 mm applies to all focal spots at the central axis with a ≈ 11° anode angle.

Figure 3.6 (c) shows the head phantom image focused on the incisor plane. Due to the limited height of the detector, the blurring effect of the 2D image is not as obvious as the images from tomosynthesis.

3D CT imaging

The TBCT geometry is different from the CBCT geometry in how the sample is scanned. The TBCT system generates multiple narrow cone beams from a series of sources, which results in several overlapping zones in the field of view (FOV). An image voxel in an overlapping zone is irradiated by more than one beam, and the number of these beams varies with the voxel's location. A 3D TBCT reconstruction algorithm was developed based on Feldkamp, Davis, and Kress (FDK) reconstruction algorithm for CBCT [58]. The FDK algorithm is an 3D extension of the standard 2D fan-beam filtered-backprojection (FBP) algorithm [59]. In the FDK algorithm, it is common to set up a virtual detector that runs parallel to the real detector and passes through the origin. The size of the virtual detector is scaled from the real detector by a factor of SAD/SDD so that the projection data on the real detector can be converted into the projection data on the virtual detector.

In TBCT geometry, each source-detector pair can be treated as a cone beam system. As previously mentioned, a given voxel at a given view angle can be illuminated by multiple source-detector pairs, the number of which ranges from 1 to 8. The filtered projection values from those sources have to be normalized by a weighting factor. The reconstruction formula of a given voxel can be expressed as:

$$f_{FDK-TBCT}(x,y,z) = \frac{1}{2}\int_0^{2\pi} \frac{\sum_{i=1}^{N} w_\beta^i P_\beta^i(x,y,z,\beta)}{\sum_{i=1}^{N} w_\beta^i} d\beta, \tag{3.2}$$

$$P_\beta^i(x,y,z) = \frac{\mathrm{SAD}^2}{(\mathrm{SAD} + x\sin\beta - y\cos\beta)^2}\left[\frac{\mathrm{SAD}}{\sqrt{\mathrm{SAD}^2+u^2+v^2}} \cdot I_\beta(u,v)\right] * h(u), \tag{3.3}$$

where $f_{FDK-TBCT}(x, y, z)$ is the reconstructed voxel value at spatial position (x, y, z), the subscript i represents the number of the x-ray source, $P^i_\beta(x, y, z, \beta)$ is the pre-weighted and filtered projection at the view angle β in the ith source-detector cone beam system, w^i_β is the weight assigned to this filtered projection. For a given image voxel at a given view angle, w^i_β equals 1 for sources that illuminate this voxel and 0 for sources that do not. In $P^i_\beta(x, y, z, \beta)$ expression, u, v are the coordinates of the reconstructed voxel's projection to the virtual detector, $\dfrac{\mathrm{SAD}}{\sqrt{\mathrm{SAD}^2 + u^2 + v^2}}$ is the pre-weighting factor that represents the cosine of the angle between the ray and the central ray, and I_β is the projection on the virtual detector. The expression inside the square brackets is the convolution with the kernel of the ramp filter $h(u)$.

TBCT scans were performed on a mouse cadaver and a pig's head, as shown in Figure 3.7. These scans had the same system geometry with SAD = 500 mm and SDD = 700 mm. A total of 720 projections were acquired for each source in both scans.

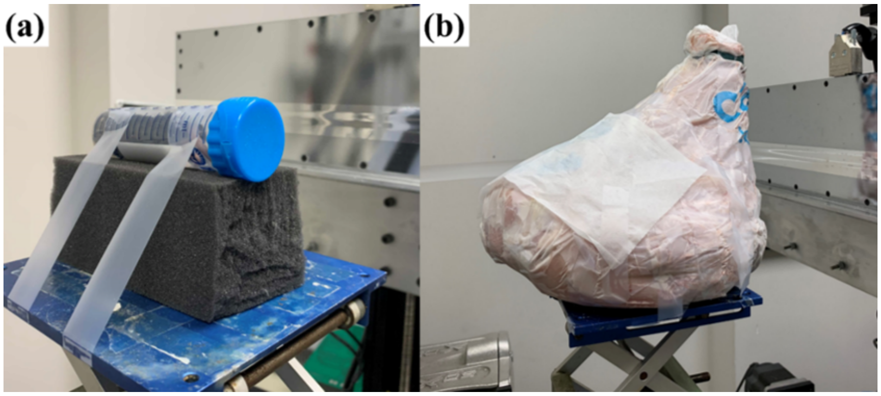

Fig. 3.7: TBCT scan setups for a mouse cadaver (a) and a pig's head (b). The source-to-axis distance and source-to-detector distance were 500 and 700 mm in both setups. The objects were sequentially scanned by a series of sources at 720 CT angles, resulting in 720 projections for each source. The mouse cadaver was scanned at 50 kV tube voltage by 30 sources in the middle of the array to cover the relatively small FOV along the z-direction. The pig's head was scanned at 80 kV tube voltage by only 9 sources to examine the imaging quality of the transverse plane through the eyes.

Due to the small size of the mouse cadaver, only 30 sources in the middle of the array were used to sufficiently cover the FOV along the z-direction. For the same reason, a tube voltage of 50 kV was applied.

The pig's head was placed on the stage so that its eyes were level with the detector. The middle 9 sources were used to perform the scan using 80 kVp tube voltage. We compared the image quality of the transverse plane through the pig's eyes between the TBCT and helical CT (SOMATOM Confidence, Siemens, Germany). The image acquisition parameters of these two scanners are listed in Table 3.1.

Scanner	SAD (mm)	SDD (mm)	Tube Voltage (kV)	Exposure (mAs)	Pixel Spacing (mm×mm)
TBCT	500	700	80	200	0.1×0.1
Helical CT	595	1085.6	80	500	0.6×0.6

Tab. 3.1: The image acquisition parameters of the TBCT and the SOMATOM helical CT.

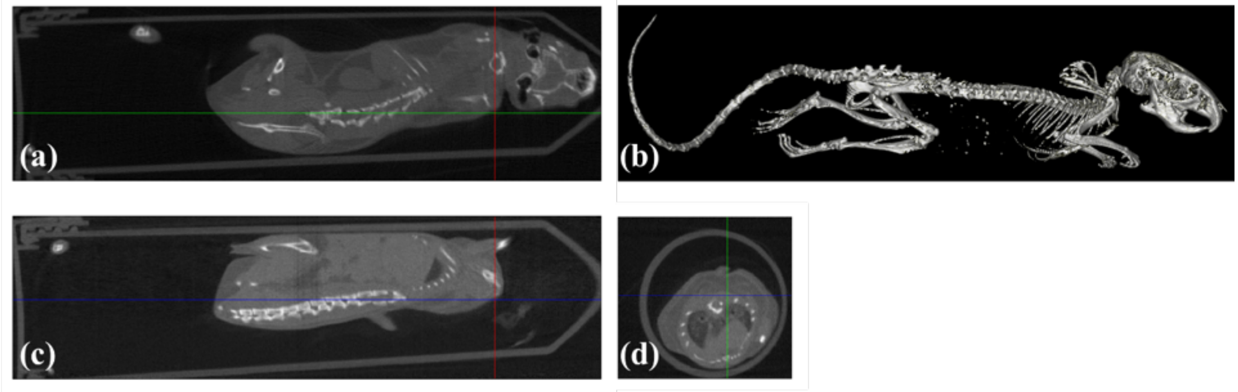

Fig. 3.8: 3D reconstruction result (b) and the three orthogonal planes: (a) transverse, (c) sagittal, and (d) coronal view of the mouse cadaver using the FDK-TBCT algorithm. The voxel size is 0.2×0.2×0.2 mm^3. The reconstructed FOV is 112×48×48 mm^3.

Figure 3.8 shows the 3D reconstruction result and three orthogonal views of the mouse cadaver using the FDK-TBCT algorithm. The voxel size is 0.2×0.2×0.2 mm^3. The reconstructed FOV is 112×48×48 mm^3.

Figure 3.9 compares the qualitative results of the TBCT and the SOMATOM helical CT on the images of the transverse planes through the pig's eyes. The detector pixels of the TBCT system were re-binned to 0.5×0.5 mm^2 to reduce the noise and kept the pixel size at a similar level as in helical CT. The tomographic pixel size of the TBCT image is 0.5×0.5

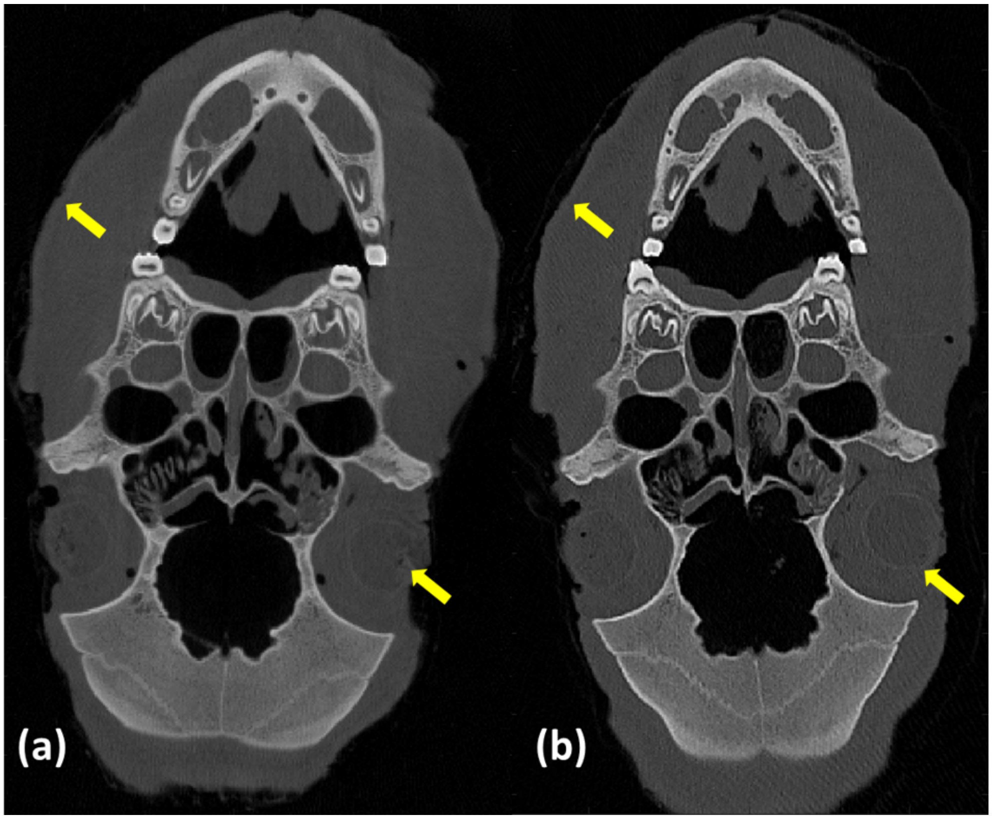

Fig. 3.9: Comparison of image quality between TBCT (a) and the SOMATOM helical CT (b). Soft tissue (arrows), such as eyeball and skin, can be well visualized.

mm^2, and the slice thickness is 0.5 mm. The pitch of the helical CT was set at 0.35 mm. The voxel size of the helical CT image is 0.48×0.48 mm^2, and the slice thickness is 0.6 mm. The reconstruction kernel in the helical CT was a routine clinical brain kernel used in radiation oncology. The TBCT reconstruction demonstrates a comparable spatial resolution of bone structure. For soft tissue imaging, the TBCT reconstruction also achieves clear visualization of eyeballs and skin (arrows in Figure 3.9).

3.5 Discussion

Thanks to the narrowly collimated fan-beam geometry, TBCT involves remarkably less scattered photon signals than CBCT. Its SPR was measured to be about 17% in contrast to 120% for the cone beam in the presence of ahead phantom. The dramatically low SPR is expected to remarkably improve the imaging quality of the TB imaging system. Moreover, a low level of SPR eliminates the need for an anti-scatter grid as usually used in CBCT and helical CT systems to reject X-ray scatter, leading to more effective use of x-rays and hence a lower dose to the patient. The anti-scatter grid, especially the 2D grid, blocks a considerable amount of primary X-ray too due to finite wall thickness. For high-resolution imaging, the grid also leaves a shadow on the images, and it is difficult to be removed completely. We may employ a 1D anti-scatter grid to further remove the remaining scattered photons if it's necessary.

Besides CT imaging, the TB system can also produce radiographic images similar to the traditional cone beam x-ray system. Although the beam divergence is different from the cone-beam x-ray radiography, it is still useful formedical applications. The low SPR is beneficial to radiography imaging too. It is similar to slot-scan radiography but without any mechanical moving parts. The imaging speed is limited by the detector frame rate. In principle, a TB system can use any fast linear array detector that is used by diagnostic CTs. State-of-art CT detectors with fast scintillators have a frame rate as high as a few thousand Hz. We employed a PCD in the benchtop imaging system. PCD intrinsically can achieve fast frame rate than scintillator-based detectors. However, the PCD currently used in our system has a maximum frame rate of 150 fps limited by the Ethernet data port. Future products with CameraLink will allow a much higher frame rate.

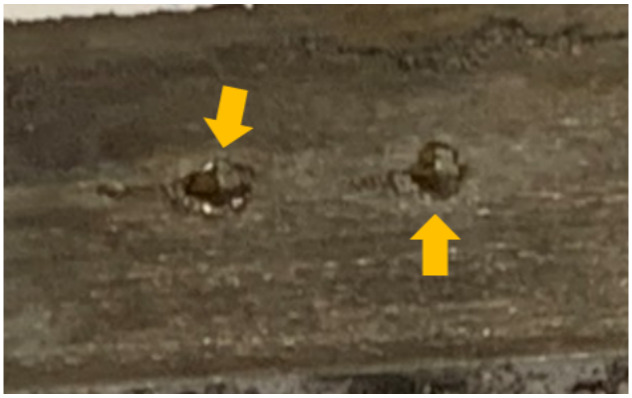

Fig. 3.10: Two melted focal spots on the tungsten target due to excessive applied electron beam power.

The focal spot power density of the tungsten target limits the distributed source tube power and therefore the imaging power. We need to carefully control the current and pulse duration to avoid damaging the target. Figure 3.10 shows a tungsten target with two melted focal spots due to excessive applied power. Faster source scanning allows higher tube power, but the source scanning speed will be limited by the detector readout rate. We can also increase the focal spot sizes to allow higher mAs scans with a sacrifice of image resolution for imaging speed. In order to balance the scanning time and high imaging quality with small focal spot sizes, it is desirable to develop an MPTEX tube with variable focal spot size. Modern iterative image reconstruction has been proved the capability of reducing imaging dose. It will also allow TBCT to achieve faster imaging speed. The emission currents vary among the cathodes. The previous publication from our group reported the variation of emission currents [25]. However, because CT transmission measurement is normalized by an air scan of the same source pixel, the variation of emission current does not cause noticeable artifacts in the images. In the future, we may program the FPGA controller to adjust the pulse width of each source to maintain a constant mAs.

Chapter 4

Small Animal X-ray FLASH Irradiator Based on Circular Source Array

FLASH radiotherapy (FLASH-RT) at ultra-high dose rates (UHDRs) (> 40 Gy/s) has gained significant momentum since the publication of an *in vivo* study in 2014 by Favaudon *et al.*, which demonstrated a significant reduction in normal tissue toxicity using FLASH-RT while maintaining similar tumor control when compared with RT at a conventional dose rate (0.03 Gy/s) [30]. Multiple follow-up studies confirming the FLASH effect paved the way for the treatment of the first human patient in 2019 using electron FLASH-RT [39, 42, 43, 49, 60–63]. Currently, proton FLASH-RT clinical trials are ongoing [64].

Section 4.2 and 4.3 of this chapter will illustrate the design and simulation of a novel small animal FLASH irradiator (SAFI) based on a circular distributed x-ray source array with 51 sources. The SAFI can deliver UHDRs (up to 120 Gy/s) for preclinical FLASH-RT studies, as well as conventional dose rates for comparative studies. Section 4.4 and 4.5 demonstrates the forward and inverse treatment plans, as well as an onboard inverse-geometry CT imaging with an add-on rotatable detector. Finally, Section 4.6 discusses the limitations and future work of the FLASH irradiator.

4.1 Introduction

The intriguing biological mechanism of the FLASH effect has attracted intense research effort; however, its exact radiobiology is not well understood yet and is under debate [45, 60, 63, 65–68]. Preclinical research is of great importance to guide FLASH-RT to clinical applications [69]. Ideally, FLASH irradiator platforms capable of delivering both conventional and UHDRs with precise control over the delivered dose-per-pulse are required to fully explore the dependence of the FLASH effect on temporal characteristics of the radiation beam. To date, nearly all FLASH preclinical studies have been performed using electron and proton beams, with the former constituting the vast majority. Electron FLASH beams have been produced using dedicated or modified linear accelerators (linacs) [37, 38, 41]. Proton FLASH beams have been produced using Singletron accelerators, isochronous cyclotrons, and synchrocyclotrons [35, 40, 47, 70–72]. Such machines require high capital investment and maintenance and are mostly dedicated to specific experimental setups or patients' treatment. Also, not all laboratory researchers have access to these radiation sources.

Producing x-ray photon FLASH beams is more challenging due to the low efficiency of the Bremsstrahlung process. Although a few x-ray FLASH-RT studies have been performed with kV and MV x-ray beams generated in national research centers, a compact and affordable FLASH-RT system is more compelling for preclinical photon FLASH-RT research [39, 51]. Bazalova-Carter and Esplen studied the feasibility of achieving UHDR in a commercially available x-ray tube with a fixed anode [46]. Although the simulation suggests the dose rate can be as high as 160 Gy/s outside the tube housing, the dose rate falls off very fast due to its low x-ray mean energy. In a later development of a kV FLASH tube for *in vitro* irradiations, x-ray beams were controlled by a shutter to deliver FLASH irradiations in pulses [73]. Rezaee *et al.* proposed another kV FLASH design consisting of two commercial diagnostic x-ray tubes with rotating anodes facing each other [50]. The FLASH dose region in their design has a more uniform dose rate distribution compared to the design of Bazalova-Carter and Esplen. Due to the limited space and size of the x-ray tube, it is impractical to employ more than two x-ray tubes in such a design.

In clinical intensity modulated radiation treatments (IMRT), the radiation dose is delivered from multiple angles by rotating the linac. It has been proposed that a multi-head linac can be designed for conformal MV photon FLASH-RT [74] However, mimicking that concept using kV sources for conformal FLASH-RT of small animals is not trivial. Due to the relatively large physical size of the x-ray sources and the close proximity to the source required to achieve a UHDR beam. It has not yet been possible to concurrently deliver FLASH-RT at multiple beam angles using conventional x-ray sources with fixed or rotating anodes.

The emerging distributed x-ray sources initially designed for x-ray imaging provides an ideal solution for preclinical conformal x-ray FLASH-RT. These sources generate a plurality of focal spots with a scanning electron beam or discrete cathode arrays [25, 54]. With all the focal spots within one vacuum envelope, the distributed x-ray source may be compact enough to simultaneously deliver FLASH-RT from multiple angles. This chapter demonstrates a novel small animal FLASH irradiator (SAFI) based on the 51 thermionic emission x-ray source.

4.2 Design of the Irradiator

Figure 4.1 (a-c) illustrates the design of the SAFI system, which comprises a fixed circular anode with a tungsten target and a circular array of cathodes in a vacuum housing. The animal subject and MAC are located in the bore outside the vacuum housing. When activated, the constituent cathodes generate a circular array of focal spots on the targets. The bore inner diameter (ID) is about 14 cm. The MAC that is designed based on the actual geometry of the animal subject in treatment planning collimates the x-ray beams to the treatment target. The aperture shape and beam intensity can be optimized to achieve the desired dose distribution similar to clinical IMRT. The same source array also is used for onboard micro-CT imaging when operating at lower kVp, smaller focal spots, and lower tube current. In imaging, the treatment MAC will be replaced with another MAC dedicated to imaging. Due to space limitations, a small area detector will be used and form an inverse-geometry CT [75]. The detector and MAC will rotate together about the animal subject while the sources that can produce x-ray intercepting the imaging field-of-view are turned on sequentially.

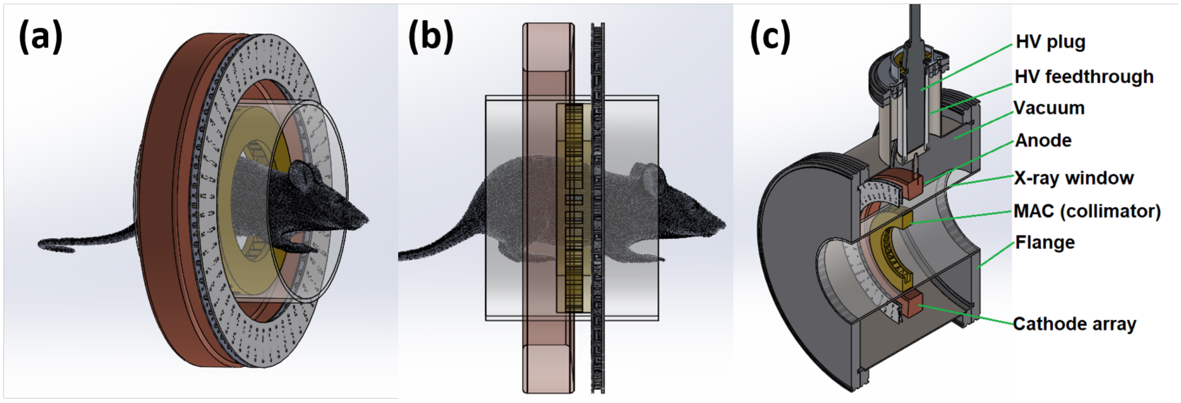

Fig. 4.1: (a-c) Schematics of the SAFI system based on a multi-pixel x-ray source. Fifty-one cathodes are equally distributed on a circle and generate a circular array of focal spots on a ring-shaped anode. A multi-aperture collimator (MAC), designed based on the specific anatomy of the animal subject in treatment planning, is positioned outside the vacuum envelope and collimates the beams to the target. All beams are turned on simultaneously during FLASH-RT treatment with optimized intensity and sequentially during inverse-geometry micro-CT imaging.

A grounded mesh grid will be used to control the beam on and off similar to the linear x-ray source we developed previously and introduced in the previous chapter [25]. When a cathode is connected to a negative bias voltage, thermionic electrons will pass through a grid mesh and generate an x-ray beam at the corresponding focal spot location on the tungsten target. A schematic diagram of the beam controller design based on the multi-source x-ray tube, as shown in Figure 2.4. Due to the complexity of the electron beam control, the SAFI system employs a uni-polar design with the anode connecting to a positive high voltage and the mesh grid grounded. Each source can be addressed independently by a controller, and they can be turned on/off simultaneously for FLASH-RT or sequentially for inverse-geometry micro-CT imaging.

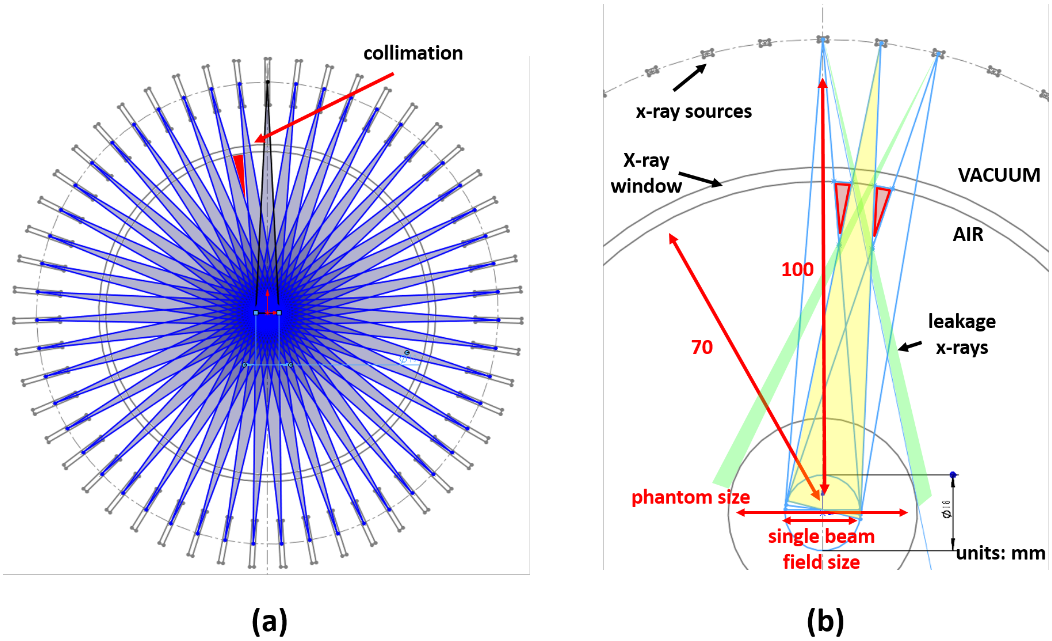

Fig. 4.2: (a) The geometry of SAFI with 51 sources and (b) the diagram of the MAC design. Illustration of x-ray leakage from the neighboring apertures. The shapes of the MAC apertures are designed based on the anatomy of the animal subject. A properly designed MAC should allow the target to receive full flux while preventing unnecessary radiation exposure from the leakage x-rays shown in (b). The MAC can be manufactured by 3D printing techniques.

Figure 4.2 (a) and (b) illustrate the geometry of the SAFI system with 51 sources and the design of a MAC. A specific MAC will be designed based on the actual shape of the target by treatment planning software and manufactured by 3D printing techniques. The MAC collimates x-ray beams to the target while preventing unnecessary radiation from leakage x-rays produced by adjacent sources. The maximum target size is jointly determined by the system geometry and the number of sources. Demonstrated in Figure 4.2 (b), x-ray beams may leak through the adjacent slots if treating an oversized target and result in undesired radiation exposure to the animals. The intensity and actual shape of each beam can be optimized by inverse planning to achieve the desired target and normal tissue doses. The x-ray intensity of each beam can be controlled by the cathode beam current, beam-on duration, or a physical compensator.

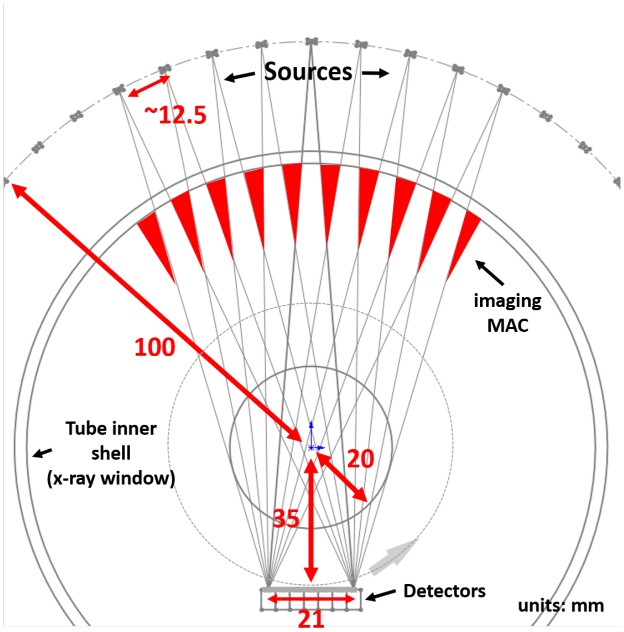

Fig. 4.3: Overview of inverse-geometry CT imaging with rotatable detectors and dedicated imaging MAC.

The small animal irradiator needs onboard imaging for setup. The same source array can also be used for onboard inverse-geometry CT imaging. A rotatable, flat small-area detector array and an imaging MAC can be positioned in the system bore, as shown in Figure 4.3. The imaging MAC is designed based on the detector shape in the beam-eye view direction. Similar to the treatment MAC, the imaging MAC should conform the x-ray beam to the detector. It will be made using a 3D printing method similar to the treatment MAC. The detector array and imaging MAC will rotate in steps during acquisition while the source array stays stationary such that the MAC can identically collimate beams for each set of projection data. At each step angle, the multi-source beam controller sequentially turns on/off selected nine sources opposite to the detector array to sample the entire field of view completely. Without rotating the animal or the sources, a rotation of the detector alone will generate only 51 CT projection angles for image reconstruction. To reconstruct high-resolution images, we can repeatedly rotate the source array or the animal subject by a small step angle (less than the angular spacing between sources) to get a new set of CT sampling in another full detector rotation for acquiring more projection angles.

4.3 Dose Rate and Beam Power Simulations

4.3.1 Monte Carlo dose rate efficiency estimation

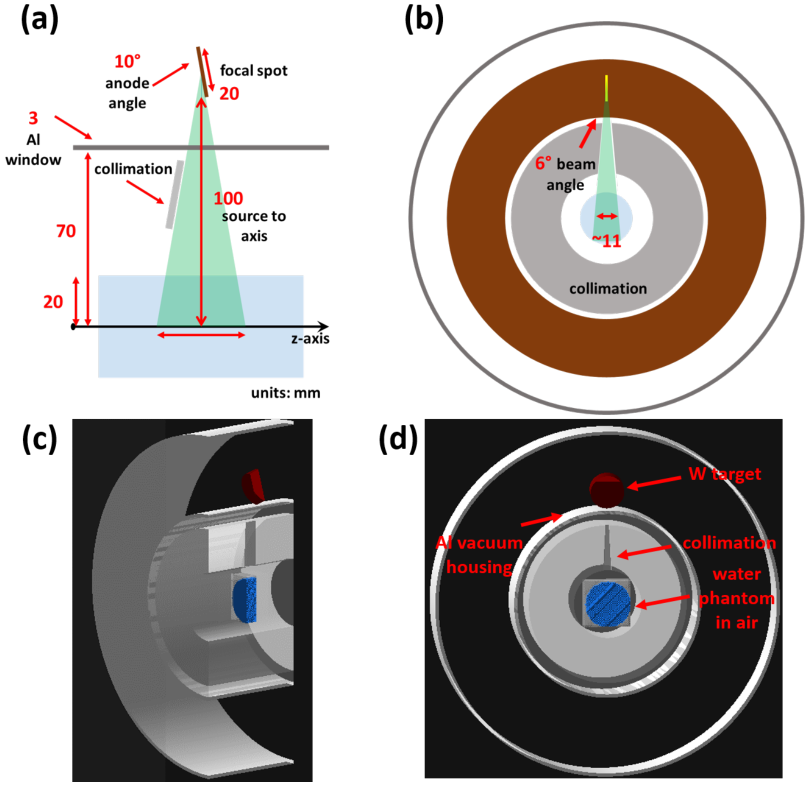

Fig. 4.4: Sagittal (a) and transverse (b) views of the SAFI system geometry; (c) and (d) Geant4 model of a single source x-ray field for dose rate estimation based on (a) and (b) design.

The dose rate of the SAFI system at the phantom center is approximately proportional to the total anode current. We employed the Geant4 Monte Carlo (MC) toolkit to calculate the x-ray production and the dose distribution in a cylindrical water phantom that represents a small animal subject. Figure 4.4 (a) and (b) show the beam geometry of a single x-ray source. Figure 4.4 (c) and (d) show the geometries in the Geant4 visualization. We modeled electron beams with 120, 160, and 200 keV energies that are incident on the tungsten target with a 10° anode angle. The cylindrical water phantom with a diameter of 40 mm was placed at the geometric center of the irradiator. The distance from the focal spots to the phantom center was 100 mm. The x-ray beam was attenuated by the 3-mm Al tube housing and collected at the surface of the water phantom. The photon fluence rates at the water phantom surface for each energy E per unit tube current $\dot{\Phi}(E)/I$ were obtained. The dose distributions per photon fluence $D(E)$ in the cylindrical water phantom for each photon energy E were then obtained. The dose rate in the water phantom per unit tube current of a single electron source in units of Gy/s/mA can then be calculated based on its spectrum according to following expression,

$$\frac{\dot{D}_i}{I} = \int_{E=0}^{E_{\max}} \frac{\dot{\Phi}(E)}{I} \cdot D(E) \cdot \mathrm{d}E, \tag{4.1}$$

where i is the location index in the water phantom. In order to achieve a dose rate $\dot{D}_{\mathrm{FLASH}}$ at the center of the phantom for N sources in the design, the anode current required for each source in units of mA is simply

$$I_{\mathrm{FLASH}} = \frac{\dot{D}_{\mathrm{FLASH}}}{N \cdot \dfrac{\dot{D}_i}{I}}. \tag{4.2}$$

Figure 4.5 (a) plots the fluence rate energy spectra $\dot{\Phi}(E)/I$ of three kVp values (120, 160, and 200) obtained by the Geant4 MC program. As estimated by Equation 4.1, the depth dose rates per mA current for the same three kVps are plotted in Figure 4.5 (b). The 50% dose rate for 120, 160, and 200 kVp are at 12.6, 15.0, and 16.0 mm depths, respectively. The increase in the 50% depth dose from 160 kVp to 200 kVp was marginal at approximately 1 mm. In order to ease the dielectric insulation requirements, the SAFI system will operate at 160 kVp for FLASH-RT treatment. Although the dose rate per tube current of 200 kVp is about 30% higher than the 160 kVp, the higher kinetic energy also results in more energy deposition on the target, which limits its peak operating current. At 160 kVp, the dose rate per mA is 0.056 Gy/s/mA at the phantom surface and 0.022 Gy/s/mA at the center of the

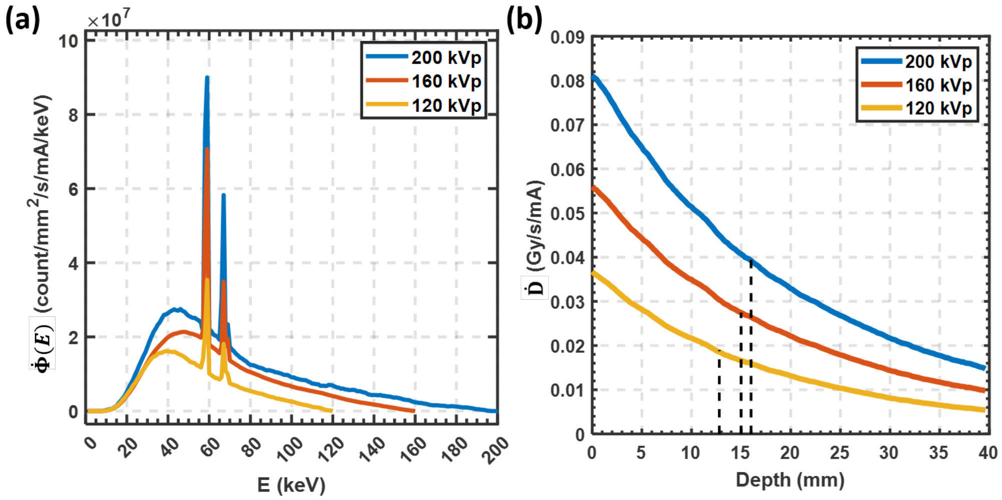

Fig. 4.5: Monte Carlo simulation results: (a) Energy spectra $\dot{\Phi}(E)/I$ of 120, 160, and 200 kVp beams per mA beam current. (b) The depth dose rate $\dot{D}(z)/I$ of 120, 160, and 200 kVp x-ray beams per mA of beam current. As shown by the dotted lines, the 50% depth dose position for 160 kVp is only 1 mm shallower than 200 kVp.

phantom with 4 cm OD.

4.3.2 Electron Beam Power Requirements

The required tube current for a given dose rate can be calculated based on Equation 4.2. A dose rate of 100 Gy/s at the center of the 4 cm diameter cylindrical phantom requires about 4.5 A total tube current. With 51 sources, the required cathode current for each source I_{FLASH} would be about 88 mA and the x-ray generator will have a power of 72 kW with 160 kVp. A FLASH-RT treatment would last <1 s depending on the total dose delivered.

The maximum power of the SAFI system is limited by the focal spot power density like other x-ray sources. In order to estimate the maximum power, finite-element analysis software (COMSOL, Inc., Burlington, MA) was used to calculate the transient temperature distribution in the target under electron bombardment. We estimated the maximum power density that can be allowed with a single-source focal spot area A via numerical simulation. Then, the maximum incident current density for a focal spot in units of mA/mm^2 was obtained by the expression

$$\frac{I_{\text{max}}}{A} = \frac{P_{\text{in}}/A}{U} \cdot \frac{1}{c_b(U)}, \tag{4.3}$$

where U is the voltage difference between anode and cathode (160 kV in this study), $c_b(U)$ is the backscattering coefficient of the corresponding energetic electron on solid tungsten. Following Equation 4.3, the total area of the focal spot needs to achieve FLASH dose rate $\dot{D}_{\text{FLASH}}$ is calculated by,

$$A_{\text{FLASH}} = \frac{I_{\text{FLASH}}}{I_{\text{max}}/A} = \frac{\dot{D}_{\text{FLASH}}}{N \cdot \frac{\dot{D}_i}{I}} \cdot \frac{A \cdot U \cdot c_b(U)}{P_{\text{in}}}. \tag{4.4}$$

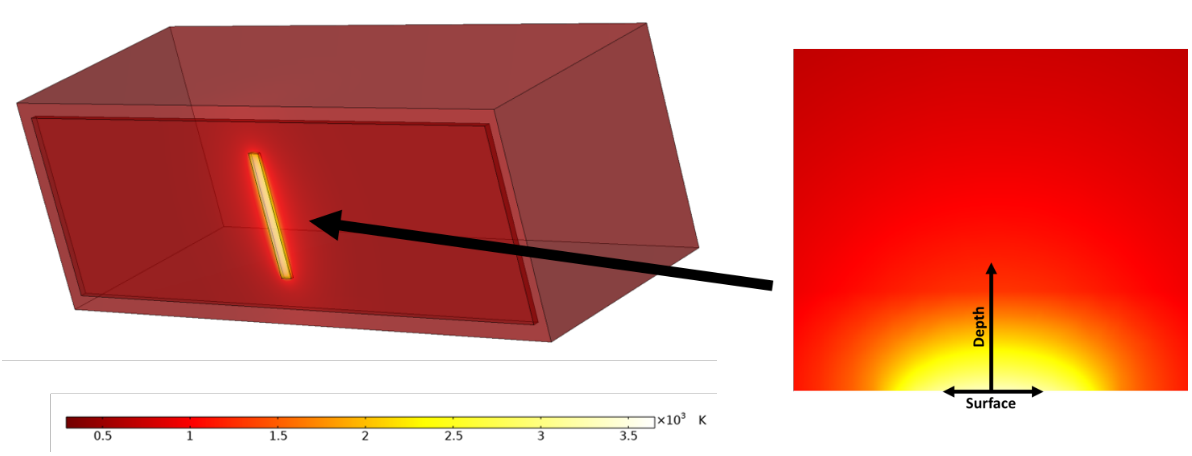

Fig. 4.6: Temperature distribution of a 2 × 20 mm^2 focal spot on the anode caused by a 160 keV 100 mA DC electron beam in FEA thermal analysis. The temperature distribution at the focal spot is shown in a cross-sectional view.

Temperature distributions, where temperature rise near the focal spot caused by a DC electron beam, were obtained by transient thermal finite-element analysis (FEA) performed in COMSOL (Figure 4.6). The center of the focal spot on the surface had the highest temperature and was defined as the temperature of the focal spot T.

Figure 4.7 (a) shows the rise of the focal spot temperature T over time for various beam-on durations t_W using the maximum incident current density I_{max}/A, for which T remain below the melting point of tungsten for each t_W (3695 Kelvin). Figure 4.7 (b) plots the

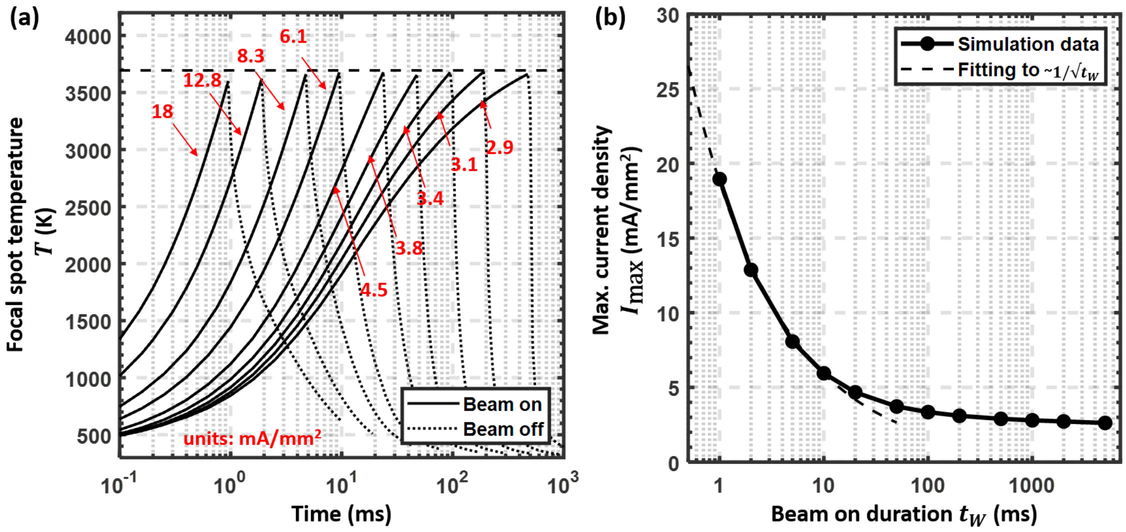

Fig. 4.7: (a) Focal spot temperature vs. time for various beam-on durations (t_W = 1, 2, 5, 10, 25, 50, 100, 200 and 500 ms). In each case, the maximum incident current density $I_{\max}/A$ were used and labeled on the plot. Solid lines indicate the temperature rise when the electron beam is on; dotted lines indicate the temperature cooling process when the electron beam is off. The focal spot temperature T are kept under the melting point of the tungsten target (3695 K). (b) Maximum incident current density ($I_{\max}/A$) vs beam-on duration t_W. The curve is fitted with diffusive approximation $\propto 1/\sqrt{t_W}$ for short t_W.

maximum incident current density $I_{\max}/A$ governed by the melting point of tungsten and t_W. Of note, $I_{\max}/A$ at short t_W is proportional to $1/\sqrt{t_W}$, as suggested by Oosterkamp [14].

Based on results in Figure 4.7, the maximum current density $I_{\max}/A$ is 2.6 mA/mm^2 for a DC beam, 3.1 mA/mm^2 for a 200-ms beam, and 19 mA/mm^2 for a 1-ms beam. If we consider the incident current requirement of each source to achieve 100 Gy/s dose rate with 51 sources that have been calculated in this section, the required minimum line focal spot area is 33.8 mm^2 for DC beam, 28.3 mm^2 for a 200-ms beam, and 4.6 mm^2 for a 100-ms beam. If the width of the line focal spot is 2 mm, the minimum length of the focal spot to achieve 100 Gy/s needs to be 17 mm, 15 mm, and 3 mm, respectively, which will be projected to effective focal spot sizes under 3 mm, 2.6 mm, and 0.5 mm respectively with 10° anode angle. In this study, we chose the focal spot area for the electron beam in the SAFI system to be 2×20 mm^2, which will be sufficient to deliver a DC-beam FLASH dose.

4.4 Irradiator Forward and Inverse Treatment Plan with Organs at Risk

4.4.1 Forward planning with dose distribution

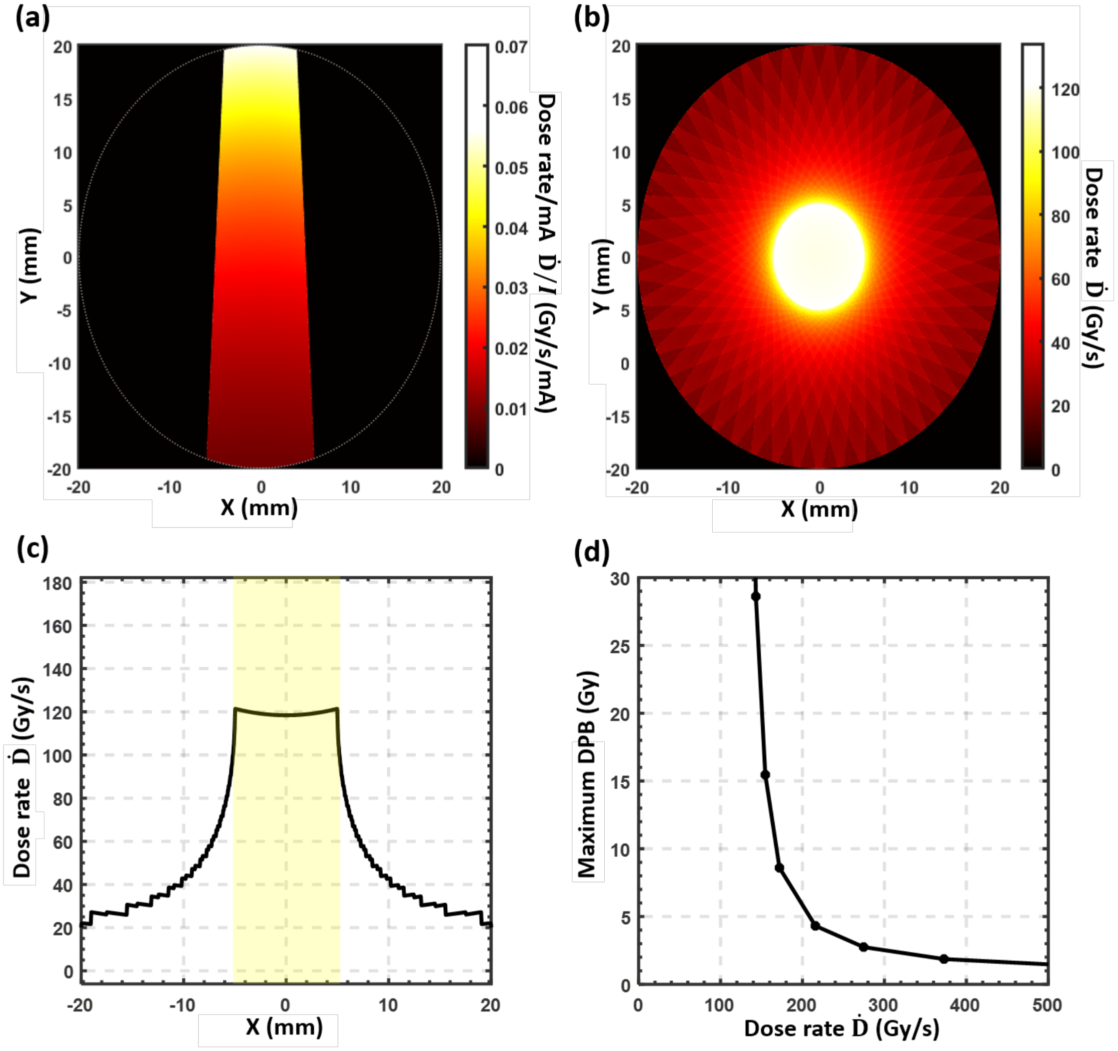

Fig. 4.8: (a) Dose rate distribution in the cylindrical phantom of single 160 kVp beam per unit tube current. (b) Total maximum dose rate distribution by 51 equally weighted DC beams with a focal spot area 2×20 mm^2. (c) Dose rate profile of the centerline in (b). The target region is highlighted. (d) Maximum deliverable DPB using focal spot area 2×20 mm^2 at various dose rates.

3D dose distributions can be obtained by Monte Carlo calculation and converted to dose rate by Equation 4.1. The focal spot size used in the simulation is 2×20 mm^2, which is achievable in practice and demonstrated above to be suitable for achieving DC ultrahigh dose rate. Based on the $I_{\max}/A$ results in Figure 4.7, the maximal incident current $I_{\max}$ for t_W can be calculated. Figure 4.8 (a) demonstrates the dose rate distribution by a single 160 kVp x-ray beam that was collimated to a 10 mm width at the center of the cylindrical phantom, as we presented in the design in Figure 4.2. Figure 4.8 (b) demonstrates the total dose rate distribution of all 51 beams. The DC tube current by each source is 104 mA (maximal for a 2×20 mm^2 focal spot). The maximum dose rate in the target center will be about 120 Gy/s, and the largest dose rate deviation in the target region is within ±2%. Figure 4.8 (c) plots the dose rate profile through the phantom center.

The maximum dose-per-beam (DPB) or dose-per-pulse (DPP) at the center of the phantom can be calculated for each dose rate by multiplying the beam-on duration t_W with the corresponding maximum dose rate from Figure 4.7 (b). Figure 4.8 (d) plots the maximum DPB at various dose rates. For example, a 10 Gy of dose can be delivered using a dose rate up to 160 Gy/s in a 63 ms beam.

4.4.2 Inverse treatment planning

The SAFI system can deliver IMRT by modulating the weight, fluence intensity, or aperture shape of each beam. We developed a simple beam-weight optimization method with aperture shape determined by the target geometry. The dose distributions of each source per anode current were calculated using the MC software. A cylindrical water phantom with a target in the center and two adjacent organs-at-risk (OARs) was used in treatment planning. The beam weights were optimized by the inverse optimization algorithm that minimizes the sum of the square of the difference between prescribed and actual doses. The inverse optimization is formulated,

$$I^* = \underset{I \geq 0}{\arg\min} \; ||b - AI||_2 \tag{4.5}$$

where I is the relative beam intensities of 51 sources, b is the planning goal, and A is the dose distribution mapping that evaluates the dose distribution from each beam. The solution was obtained by the pseudo-inverse method.

The weight of each beam can be modulated below the maximum beam power to achieve a more desirable dose distribution while still keeping over 40 Gy/s dose rate in the target. Figure 4.9 (a) and (b) show the dose rate distribution of an inversely optimized treatment plan according to 4.5. A target of 10 mm diameter is located in the middle of two OARs. The beam weights that contribute more dose to the OARs were minimized. The dose rate of the treatment target region can still maintain above 40 Gy/s in this example, whereas the average dose received in OAR regions is below 15% of the target dose.

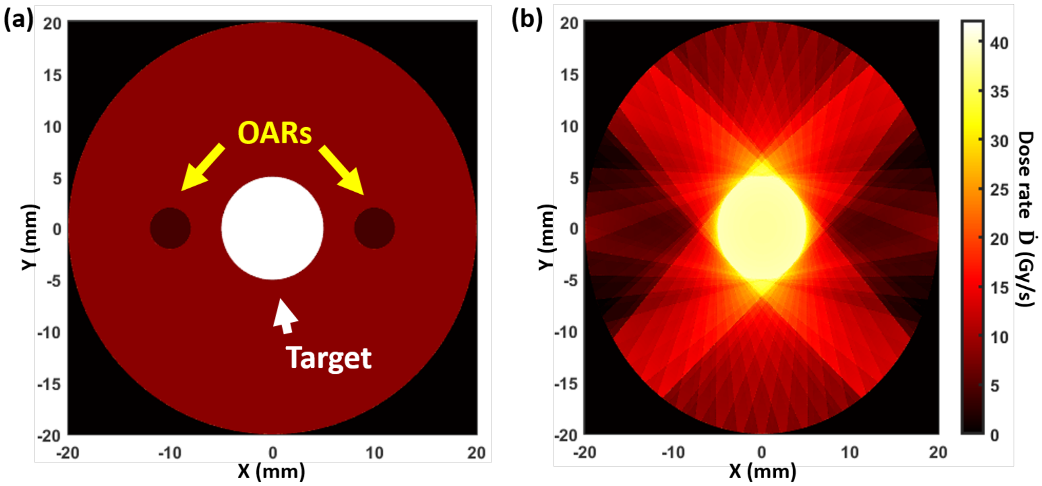

Fig. 4.9: An example of inverse FLASH-RT planning. (a) The geometry with a 1 cm OD target in the middle of two 5mm OD OARs. (b) Dose rate distribution obtained by inverse-optimization. The OARs doses are minimized while keeping the target DC dose rate at 40 Gy/s.

4.5 On-board Imaging System

4.5.1 Electron optics design

FLASH-RT requires large focal spots to achieve UHDR, while inverse-geometry CT needs smaller focal spots for high resolution imaging. We designed electron optics of the SAFI system that consisted of multiple focusing electrodes. The focal spot size can be changed by adjusting the voltage of the focusing electrodes. The finite-element charged-particle-tracing model in COMSOL was used for the electron optics design.

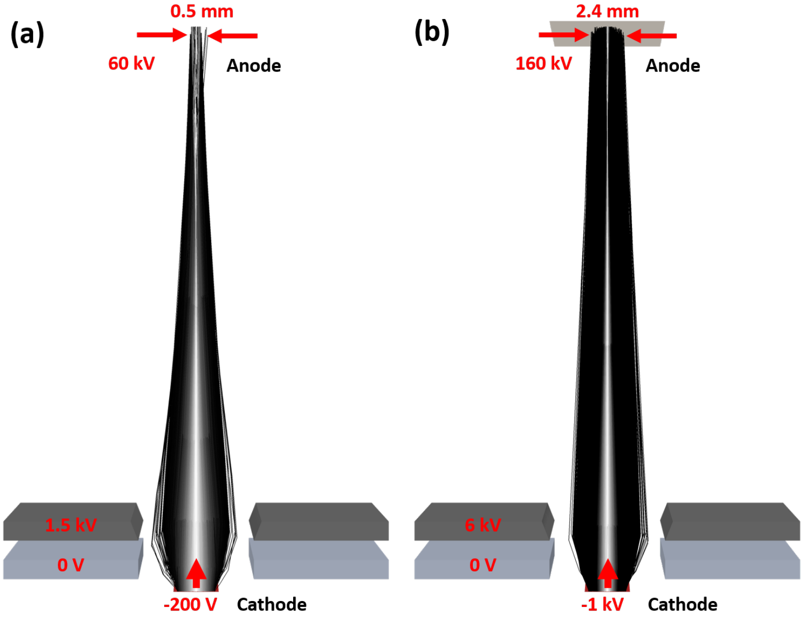

Fig. 4.10: Examples of electron beam optics of two operation modes: (a) inverse-geometry CT imaging mode and (b) FLASH-RT mode. The electron beam focal-spot width can be adjusted by the beam focusing electrodes.

Figure 4.10 shows a simplified electron optics design that enables variable focal spot sizes for FLASH-RT and CT imaging modes. The electron beam focal-spot width can vary between 0.5 mm to 2 mm by changing the voltages of focusing electrodes. The 2 cm focal spot length is projected to about 3.5 mm by the 10 degree angle angle. It can also be focused to a smaller focal spot size with a similar electron optics design. In FLASH-RT mode, the anode voltage is 160 kV, while a much lower anode voltage (60 kV) is used in the CT imaging mode.

4.5.2 Image reconstruction of inverse-geometry CT

The source array of the SAFI system can remain stationary and only the detector rotates. However, the stationary SAFI system can only produce 51 projection measurements. By rotating either the animal subject or the sources with N small-angle steps between the adjacent source angles, one can obtain N-fold projection angles that can be used to reconstruct high-resolution images. We implemented an iterative image reconstruction algorithm to reconstruct tomographic images from limited views [76]. With the system matrix A, the image data μ is reconstructed from the measurement y by minimizing the objective function

$$\mu^* = \underset{I \geq 0}{\arg\min} \; \Big((y - A\mu)^T)D(y - A\mu) + \lambda R_{\text{TV}}(\mu)\Big) \tag{4.6}$$

$$R_{\text{TV}}(\mu) = \sum_{i,j} \sqrt{(\mu_{i,j+1} - \mu_{i,j})^2 + (\mu_{i+1,j} - \mu_{i,j})^2} \tag{4.7}$$

where D is a diagonal matrix associated with the Poissonian noise of the projection data, λ is the tuning parameter to set the strength of the regularization, and $R_{\text{TV}}(\mu)$ is the regularization term based on the prior knowledge of the total variation in adjacent locations [77]. The optimization was performed using the conjugate descent algorithm. We generated projection data using the FORBILD head phantom (Figure 4.10 (a)) and compared the difference in image quality with different numbers of projection angles.

Projection data in inverse-geometry CT was generated using the FORBILD numerical head phantom and reconstructed using the iterative reconstruction algorithm based on Equation 4.6. The reconstructed images of stationary and rotating SAFI systems with different number of projection angles are shown in Figure 4.11 (b-d). Due to insufficient views, stationary-source imaging ($N = 1$) is blurry due to high smoothness constraints, and it may still be good enough for image guidance. The rotating system is simulated using $N = 2$ and $N = 3$ rotation steps that produce in total 102 and 153 projection angles respectively.

The SAFI system can produce images with sufficient resolution for treatment planning with additional rotation steps.

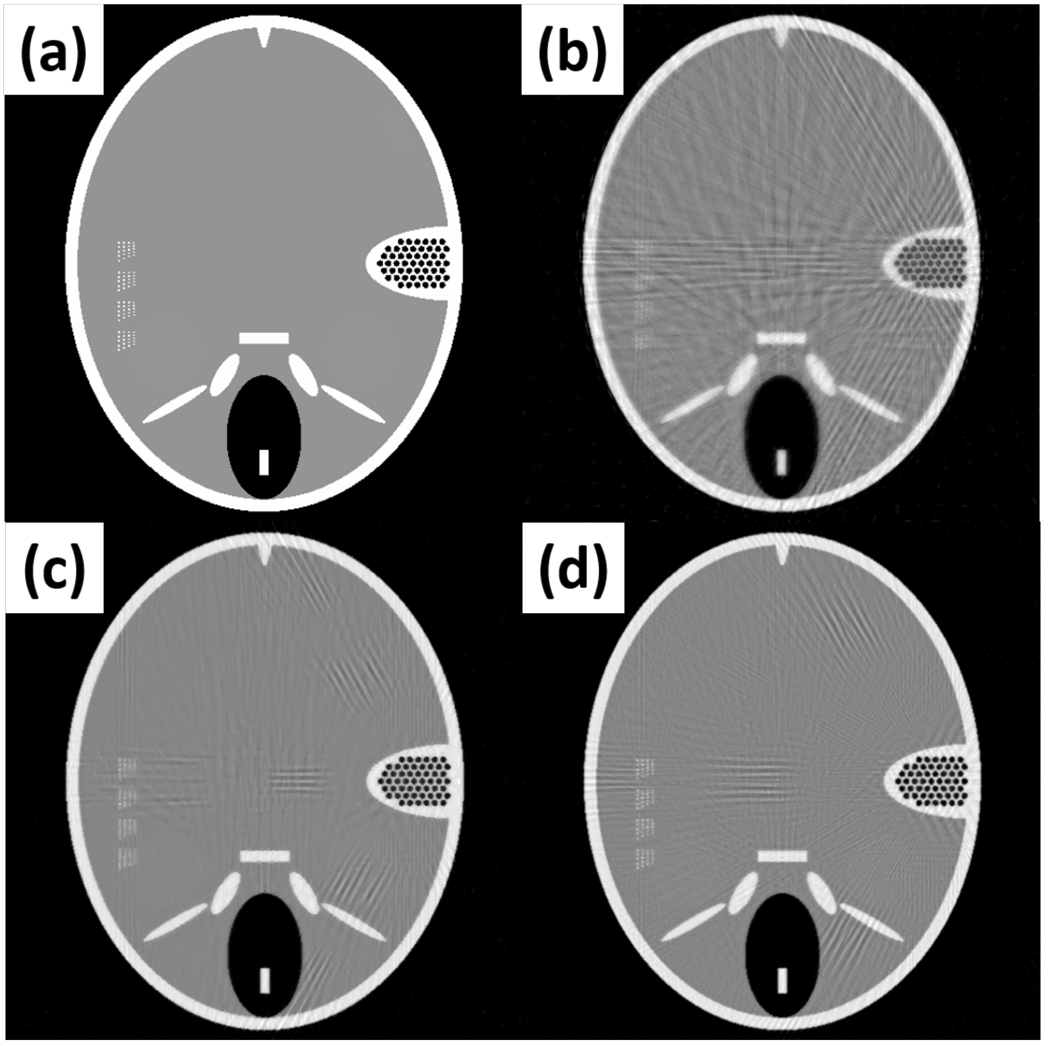

Fig. 4.11: Simulation for inverse-geometry micro-CT. (a) The FORBLID head phantom. Reconstructed images using conjugate gradient algorithm with (b) 51 ($N = 1$), (c) 102 (51×2, $N = 2$), and (d) 153 (51×3, $N = 3$) projection angles.

4.6 Discussion

Preclinical studies of new radiation treatment techniques with small animal irradiators are of paramount importance for the advancement of human radiotherapy. It is important that the dedicated platforms can administer radiation doses to animals in a similar way as human treatments in radiation oncology clinics. While proton therapy accelerators and linacs can potentially deliver conformal FLASH-RT to human patients, current small animal FLASH-RT modalities based on proton accelerator or dedicated linacs have various limitations such as accessibility to the machines and limited penetration depth of the electron beams. Current small animal x-ray FLASH-RT solutions are incapable of delivering conformal doses to deep-seated targets. Our design of SAFI based on distributed x-ray source technology potentially can deliver a highly conformal dose with UHDR and allow broad preclinical studies of FLASH-RT.

The choice of 51 sources of SAFI is based on the trade-off between maximum field size and dose rate. It is also the same as the number of beam angles by tomotherapy. With 51 sources turned on simultaneously, the current design allows treating a target $\propto 1 \times 1$ cm^2 large. Further increase of source number is possible, but the field size will be reduced to accommodate the MAC. Further shortening the distance between MAC and anode will allow treating a larger target. Because MAC is installed in air, the anode on high voltage has to be a certain distance to the MAC to provide sufficient dielectric insulation. Grounding anode will allow further reduction of distance from the focal spot to the MAC, but the source scanning control would be difficult to design with the cathodes on negative high voltage.

Rotating anode is broadly used in high-power x-ray sources. In principle, SAFI may employ a rotating anode if necessary. Based on our simulation, a fixed anode with 51 focal spots may produce sufficient x-ray flux for FLASH-RT. Fixed anode reduces the complexity of the system and the cost of the system. The anode can be made of oxygen-free copper brazed with a tungsten target. Because a FLASH-RT operates in a very short time, the temperature rise of the anode will be only a couple hundred degrees. Thus, we consider no active cooling is necessary.

The majority of clinical RT machines, including linacs and proton therapy systems, deliver pulsed radiation beams. Many FLASH radiobiological questions require investigating various microstructure parameters of the beam used in dose delivery [69]. For example, many studies claimed the benefits of delivering doses in pulses with a mean dose rate higher than FLASH [43, 45]. Studies showed that the dose-per-pulse, in addition to the mean dose rate, has a significant biological impact [30, 37, 41, 49, 60]. Our SAFI system is capable of delivering FLASH doses either in DC or in short beam-on durations. If using a 2×20 mm^2 focal spot, shorter beam-on duration allows a much higher instantaneous dose rate, which can be used to emulate clinical FLASH-RT modalities such as linacs and proton machines operating in pulsed mode. In this case, the tube current and beam-on duration need to be carefully controlled to avoid damaging the tungsten target.

During FLASH-RT delivery, the cathode currents will be a few amperes, and the instantaneous power will be as high as a few hundred kilowatts. A high voltage power supply with high power is not easily accessible. A pulse-discharge capacitor can be used as the power supply of the SAFI. The capacitor may be charged to 160 kV slowly before treatment and discharged during the treatment. The voltage drop can be compensated in treatment planning. Such a high voltage pulse-discharge capacitor can be developed with super-capacitors, which is now affordable due to the rapid growth of the electric vehicle industry.

Chapter 5

Thin-film Target on Diamond Substrate

This chapter introduces a novel composite x-ray target, the tungsten(W)-diamond target, which is being developed in our lab. Its design and optimization of parameters have been studied.

5.1 Introduction

Conventional x-ray sources produce x-ray photons by bombarding a thick high atomic number (Z) refractory metal target with high-energy electrons. Except for the energy carried away by back-scattered electrons, most of the incident electron kinetic energy is converted into heat and deposited in the target. The maximum power of an x-ray tube thus is limited by the focal spot power density. The maximum power for different target materials subject to continuous beam currents was derived by Grider *et al* [78]. To achieve higher power, rotating anode x-ray sources were developed to reduce the dwell duration of the focal spots. Osterkamp derived the maximum power of the x-ray source with a rotating anode [14]. The faster the anode rotates (the shorter dwell duration), the higher tube power can be achieved. Modern computed tomography (CT) x-ray tubes have a focal spot line speed up to 110 m/s and power over 100 kW [3]. Other than employing a rotating anode, using a composite material x-ray target may also increase the power density limit.

Emerging distributed x-ray sources enable new designs for x-ray imaging systems. The scanning beam digital x-ray (SBDX) source employs a transmission target with thin tungsten (W) target on a liquid-cooled beryllium window [19]. Linear array x-ray sources, such as multi-pixel field emission x-ray (MPFEX) source and the multi-pixel thermionic emission x-ray (MPTEX) source that our group developed employ an elongated fixed reflection W target [54]. Circular source array for SAFI system, as described in the previous chapter, also needs better target material for higher power. However, it is technically challenging, if not impossible, to employ rotating anodes in these distributed x-ray sources. Working in pulse mode, the dwell duration of distributed x-ray sources is determined by the detector speed. Limited by scintillation speed or readout electronics, the x-ray detector arrays for CT scanners usually have a maximum speed of about a few thousand samples per second, which limits x-ray pulse width to a few hundred microseconds. Most distributed x-ray sources with a thick W target have a maximum power of a few kW depending on focal spot size, greatly limiting the imaging speed of distributed x-ray imaging systems [24–26, 75, 79].

Improving the thermal conductivity of the target material is a viable approach to increase the focal spot power density of distributed x-ray sources without major modification of the tube design. With the highest thermal conductivity among all known materials, diamond has been utilized in several high brilliance x-ray sources [80–85]. The tungsten-diamond (W-diamond) thin-film target usually is made of a thin layer of tungsten deposited on a diamond substrate. The thermal and radiative properties of thin-film targets are superior to traditional thick targets for the following reasons: 1) Since electrons are gradually slowed down by collisions, the average electron energy in the thin-film target is much higher than in the diamond substrate, giving a higher radiative yield compared to thick targets; 2) As electrons reach deeper layers of the target, they produce only very soft x-rays that are mostly filtered out by downstream x-ray windows and other source filtration of the beam. In thin-film targets, these unwanted low-energy electrons instead deposit their energy in the diamond substrate, which avoids overheating the target; 3) The target and substrate material temperatures may be very different due to the temperature gradient in the thin-film target. Thus, the focal spot power density may not be limited by the melting point of the target material.

While the radiative and thermal characteristics of thick x-ray reflection targets have been studied thoroughly, the properties of thin-film targets are very different and have not been studied thoroughly. In most previous studies, the W-diamond is used as a transmission target [13, 86–91]. However, it can be used as a reflection target in distributed x-ray sources as well [85]. In the past few years, the x-ray production of W-diamond thin-film targets was studied via Monte Carlo simulation, finite-element thermal analysis of the target materials was performed, and the performance of W-diamond thin-film targets in both transmission and reflection configurations was predicted. The results of this study can be used to guide the design of distributed x-ray sources with thin-film targets. The use of properly designed thin-film W-diamond targets can greatly boost the output of distributed x-ray sources.

5.2 X-ray production with a thin-film target on diamond substrate

A thin-film target bombarded by an energetic electron beam generates x-rays in a way similar to the conventional targets. However, depending on the material of the target, the thickness of the thin film, the direction of the produced x-rays, and the energy of the electron beam, the amount of the Bremsstrahlung and characteristic x-rays can be drastically different. In order to quantify the x-ray production from the thin-film target, we did virtual experiments via the Monte Carlo simulations.

5.2.1 Monte Carlo simulation

Geant4 Monte Carlo toolkit was used to determine the x-ray production efficiency of the W-diamond thin-film target [92].

Simulation setup

In the model, tungsten thin films with various thicknesses on a 1-mm thick and 3-mm diameter diamond disk were considered. Electron beams with kinetic energies ranging from 40 to 150 keV are bombarded on the target perpendicularly. A total of 100 million particles were simulated for each combination of electron energy and W film thickness. X-ray energy fluence rates (or intensities) in the transmission and reflection directions were recorded as shown in Figure 5.1. A 3-mm aluminum filter was used to simulate the filtration by the x-ray window.

Transmission and reflection x-ray production

Figure 5.2 shows the transmission and reflection x-ray intensities per mA of electron beam current versus the W film thickness for different electron beam energies. The transmission x-ray intensity increases with target thickness at the beginning, then reaches the maximum value at the thicknesses of approximately 1.2, 2.5, 3.9, 5.7, 6.9, and 10.1 μm for 40, 60, 80, 100, 120, and 150 keV, respectively. Then, the x-ray intensity slowly decreases with the increase of target thickness due to self-attenuation. On the other hand, the reflection x-ray intensity increases monotonically with the thickness of the W target. The reflection intensity reaches the maximum value at a similar thickness as the transmission intensity. The maximum transmission x-ray intensities are about 40-50% higher than the reflection x-ray intensities for all energies.

Angular distribution of x-ray intensity is shown in Figure 5.3. The characteristic x-rays are nearly isotropically distributed, while the Bremsstrahlung is anisotropic and weighted more in the transmission direction (same as the momentum direction of the electron beam).

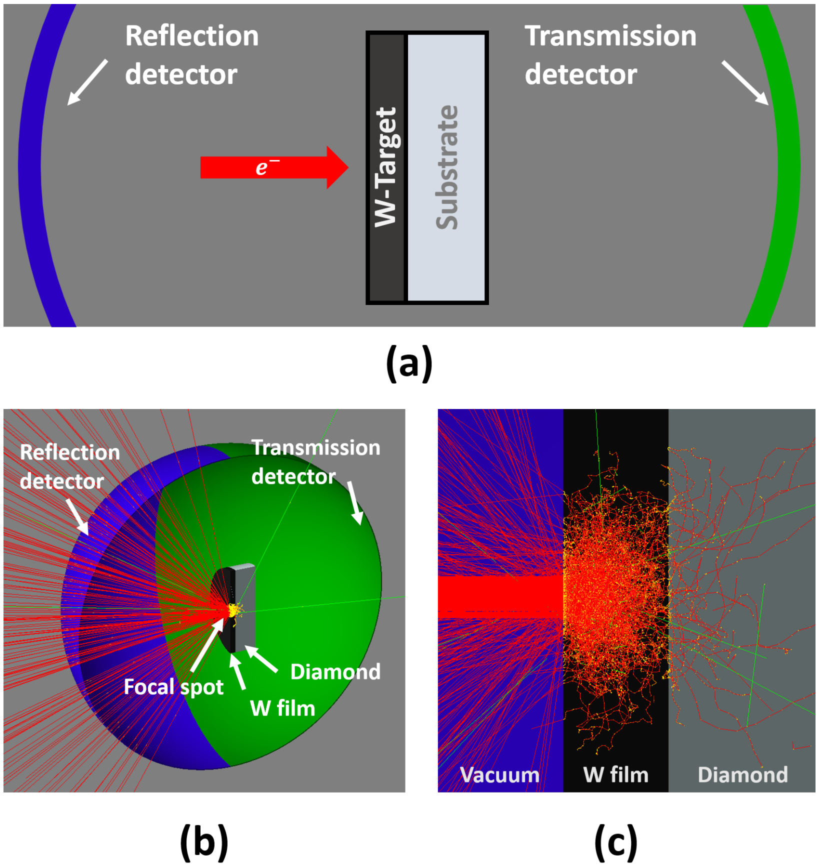

Fig. 5.1: (a) Schematic diagram of the thin-film W-diamond target for MC simulation. A parallel electron beam is incident on the W-diamond thin-film target and produces both transmission and reflection x-rays. Transmission and reflection x-rays are collected by the detectors on the right and left, respectively. (b) Cross-sectional visualization of MC model using Geant4 toolkit. Red lines and green lines represent electrons and photons.

5.3 Thermal performance of thin-film target on diamond substrate

As introduced in Chapter 1, in the conventional electron-impact x-ray source design, the majority of the electron beam kinetic energy is stopped by the Coulomb field in the target material. A large amount of energy is elastically transferred to the target material, which

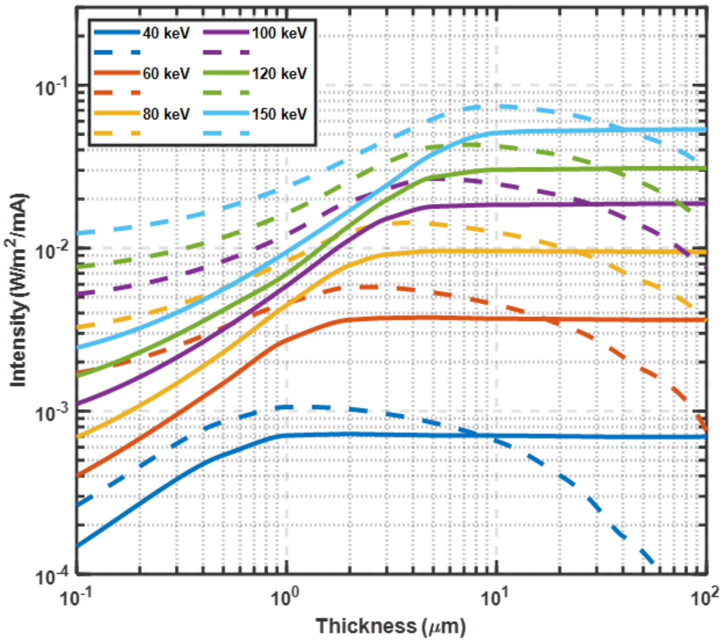

Fig. 5.2: Averaged transmission (dashed lines) and reflection (solid lines) x-ray intensities (as energy fluence rates) at 1 meter away from target per mA of cathode current versus the thickness of W target. Transmission x-ray intensities have peak values at specific target thicknesses depending on electron energies due to self-absorption, whereas the reflection targets reach plateaus at similar thicknesses.

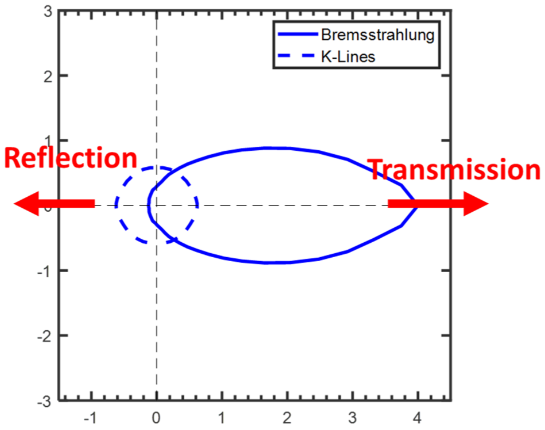

Fig. 5.3: Angular dependent K-alpha characteristic x-rays (K-Lines) and Bremsstrahlung from a 1 μm tungsten target bombarded by 200 keV electrons. The K-alpha characteristic x-rays are isotropically distributed, while the Bremsstrahlung is anisotropic and forward directional.

leads to the target material's local temperature rise. To determine the maximum power of an electron-impact source design, we will need to carefully study the thermal performance of the system, including the energy deposition rate in the target material(s), the heat diffusion of the materials, and the boundary conditions.

5.3.1 Monte Carlo simulation

Geant4 Monte Carlo toolkit was used to determine the bombarding electrons' energy depositions in the W-diamond thin-film target.

Simulation setup

Similar to the x-ray production efficiency simulation in Section 5.2.1, electron beams of kinetic energies ranging from 40 - 150 keV were incident on the target perpendicularly. The energy and its deposited location in the W film and the diamond substrate were recorded and used as heat input in the finite-element thermal analysis.

Depth-dependent energy deposition power density in the W-diamond target per mA of beam current

Figure 5.4 shows the energy deposition power densities at different depths per mA of incident electron beam current (or tube current) obtained from the Monte Carlo simulations. The results of incident electron kinetic energies ranging from 40 to 150 keV were plotted in separate figures. The peak energy deposition increases with the target thickness for thin W targets and reaches a maximum value when the thickness is beyond a certain threshold. In diamond, the power density is much lower than the W due to its low density. The low-atomic-number diamond substrates do not produce significant x-ray photons. Due to self-absorption, there is an optimal transmission target thickness that produces the maximum x-ray intensity for a given tube kVp.

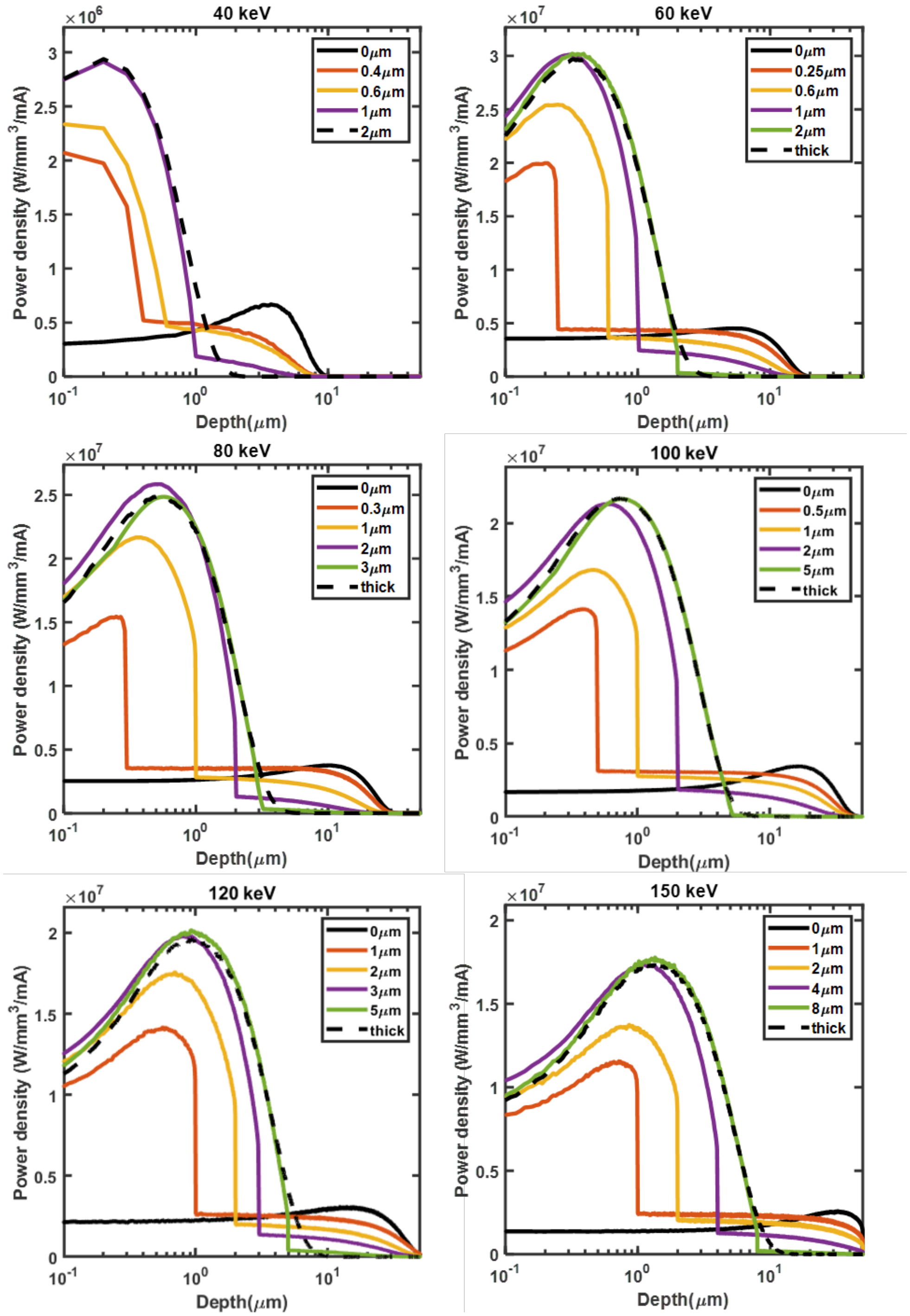

Fig. 5.4: Energy deposition power density per mA of cathode current vs. depth in the W-diamond thin-film targets for different kVps. The curves in each panel represent the results of W-diamond targets of different W-film thicknesses. The discontinuities of the curves indicate the locations of the W-diamond interfaces due to the stopping power difference between W and diamond.

5.3.2 Finite-element heat-transferring simulation

COMSOL Multiphysics software (COMSOL, Inc., Burlinton, MA) was used to study the thermal performance of the W-diamond thin-film target of various W film thicknesses, and it was compared with a thick W target.

Simulation Setup

In the simulation model, the W film was attached to a 1-mm thick diamond substrate and was embedded on a large copper anode. Figure 5.5 demonstrates the cross-section of the axial-symmetric finite-element (FE) model and the nonlinear temperature dependence of the thermal conductivities of tungsten, copper, and diamond [93–95]. The thick W target was also simulated for comparison. In this case, we replaced the W-diamond with the same-sized W material.

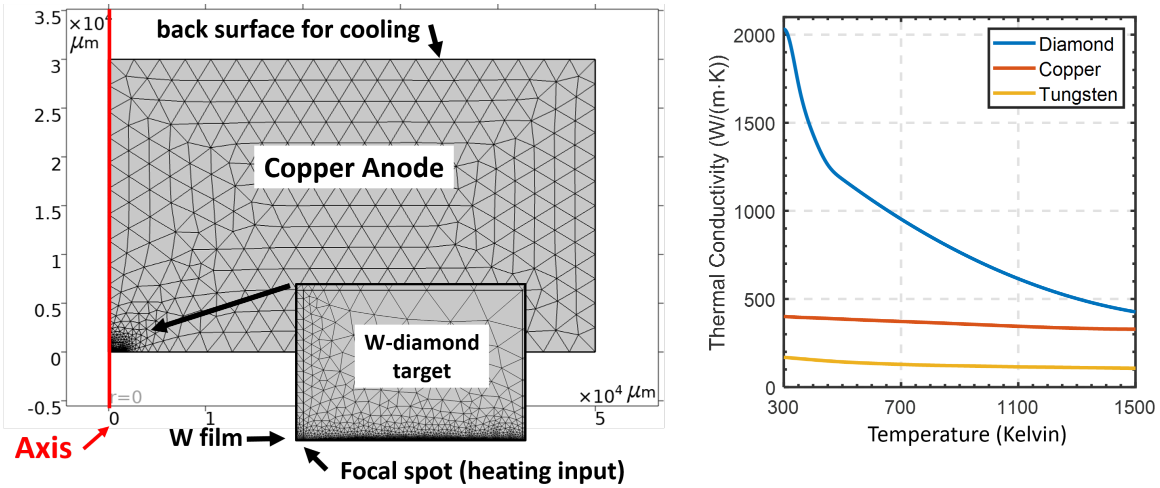

Fig. 5.5: Cross-section of the cylindrical symmetric FE model (left) and nonlinear temperature dependence of the thermal conductivity of diamond, copper, and tungsten used in the simulation (right).

Fixed anodes can be cooled by water or insulation oil. The locations of cooling pipes in the anode body can be very different in different tubes, but their locations would not affect the peak power of the tubes as they are relatively far away from the focal spot. Thus we set the back surface of the copper cylinder to a fixed temperature of 373.15 K for cooling in the simulation. The side surfaces of the copper disk were set to an adiabatic surface. The round focal spot has a diameter of 0.1 mm. The heat input was modeled as a volume heat source, including the W and diamond. The power density of the heat source volumetric per incident current was derived from the MC energy deposition result for each electron beam energy ranging from 40-150 keV. It was assigned to each mesh point in the heat source volume depending on the depth from the target surface.

In the FEA simulation, the deposited power was gradually increased until the tungsten or the diamond reached their temperature limitation. The maximum temperature for tungsten was set to its melting point (3695 Kelvin). Although diamond has a very high melting point, its crystalline structure is unstable at high temperatures and will degrade to a more stable graphite form gradually in high temperatures [96, 97]. Thus, we chose two maximum temperatures for diamond, 1800 and 2000 Kelvin. Below the temperature threshold, the graphitization rate of diamond is insignificant (2000 Kelvin) or negligible (1800 Kelvin) [98]. The results from both temperature limitations can be used for x-ray sources with different expectations of lifetimes. The finite-element solver calculated the temperature distribution of the W-diamond target in both continuous (DC) and pulse mode. In DC mode, the electron current was continuous, and the temperature distribution was in an equilibrium state; in pulse mode, the heating source was turned on for short dwell duration, so the temperature distribution was time-dependent.

Maximum tube power in DC mode

The maximum power density of the W-diamond thin-film target can be limited by either W film or the diamond substrate, depending on the thickness of the W target and the electron energy. For thin W film, more electron energy is deposited in the diamond, which reaches the graphitization temperature point first; On the other hand, the W material will reach its melting point first for thicker W film. In Figure 5.6, we plotted the maximum available DC tube currents for different W film thicknesses at different kVps. There are three regions in the maximum available tube current vs. W target thickness curves. In region 1, the increase of W film thickness will reduce the heat deposition in the diamond. Thus the maximum power increases with the thickness of the W film. In region 2, the tungsten film has an intermediate thickness, and the maximum power reaches a plateau. In region 3, the target is thick. The melting point of W limits the power, and the diamond will always be below 1800 Kelvin. The maximum power decreases with the thickness of the W film.

Maximum tube power in pulse mode

Many x-ray sources work in pulse mode. The source is activated only for a short period before the focal spot reaches the melting point. Thus, pulse mode multi-pixel sources operate at a higher power than continuous mode. We employed a transient thermal analysis module of the COMSOL software to calculate the time-dependent focal spot temperature for pulse mode operation. The maximum input current densities were computed for dwell duration ranging from 0.01 ms to 10 s for four different focal spot sizes, 0.1 mm, 0.2 mm, 1.0 mm, and 2.0 mm. We performed the same pulse mode simulations for the W-diamond thin-film and the thick W targets for comparison.

We obtained the target's transient temperature distribution and maximum power density in pulse mode from the COMSOL thermal simulation. In Figure 5.7, we plotted the temperature distribution along the center axis for a 5-μm W-diamond thin-film target. The temperature increases over the duration of the electron beam heating until when the target is in equilibrium or reaches the temperature limits (reaching the melting point in W or 2000 Kelvin in diamond). The temperature gradient in W is higher than in diamond due to the difference in thermal conductivity. The temperature gradient is high when higher input current density is used because higher localized energy deposition builds up the temperature near the surface faster.

In Figure 5.8, we plotted the maximum power density at 100 keV as a function of pulse duration for four different focal spot sizes. The results for the W-diamond target with

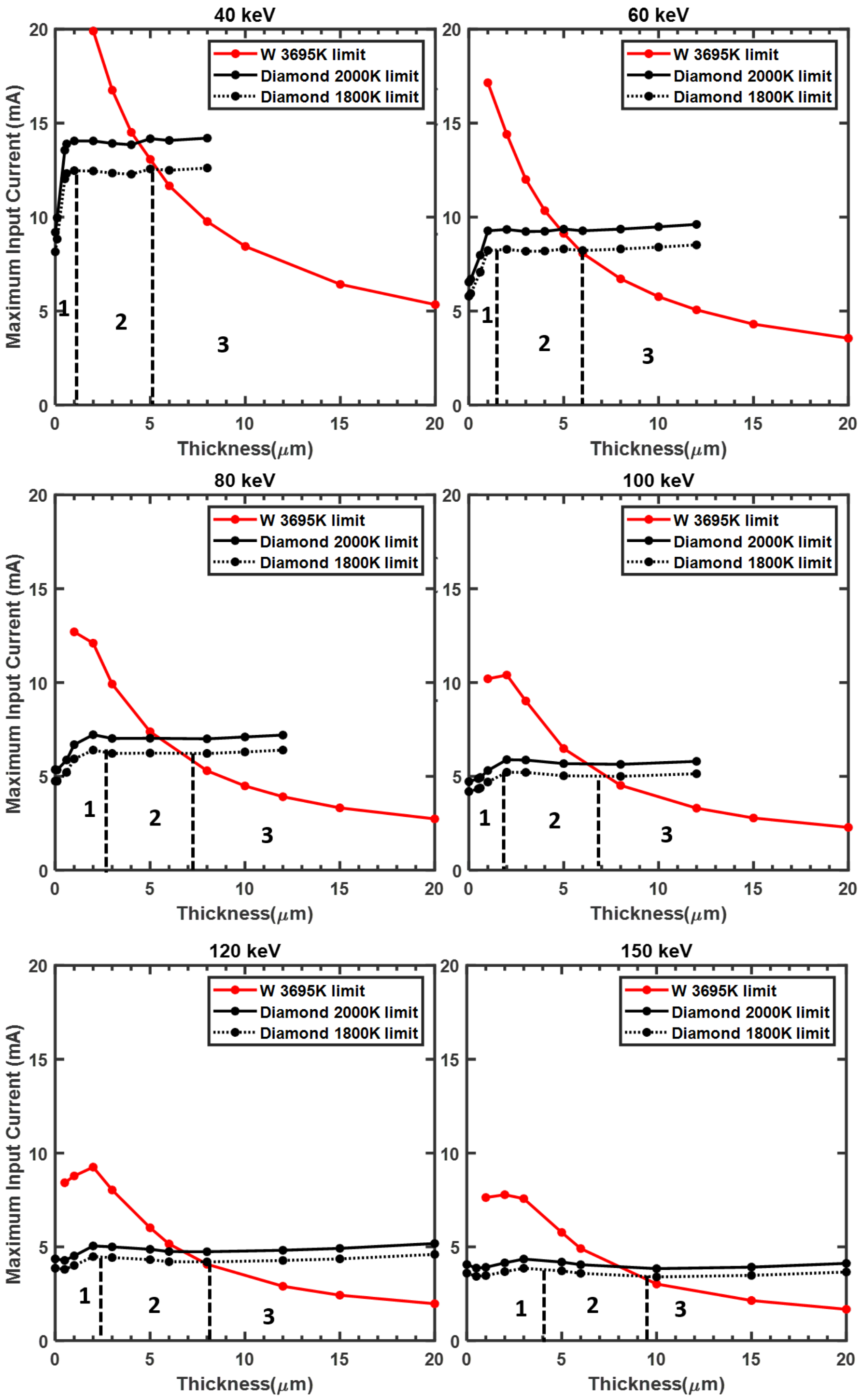

Fig. 5.6: Maximum DC tube current versus the thickness of the tungsten target, limited by the melting temperature of tungsten (red) or limited by the graphitization of the diamond substrate (black solid: 2000 Kelvin and black dotted: 1800 Kelvin). Results of six incident electron kinetic energies are shown in the same scale.

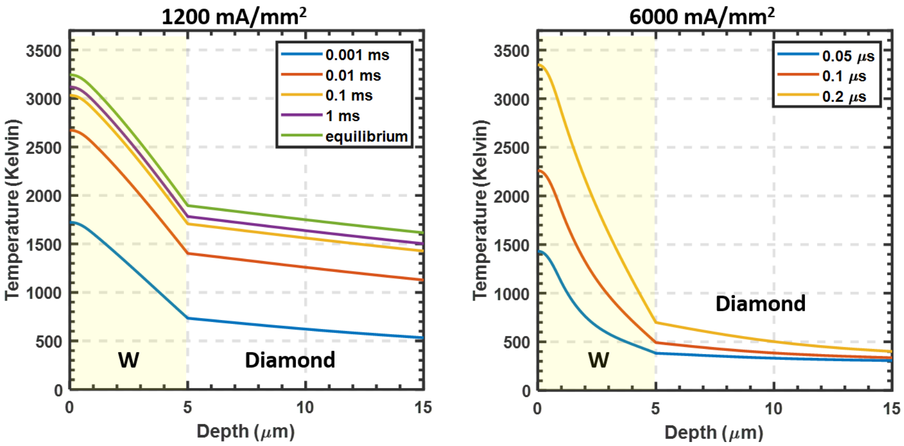

Fig. 5.7: Pulse mode temperature distribution along the center axis for a 5-μm W-diamond thin-film target using current density 1000 mA/mm^2 (left) and 5000 mA/mm^2 (right). Temperature distributions at several time durations are plotted for both cases. Highlighted depth range indicates the W film domain.

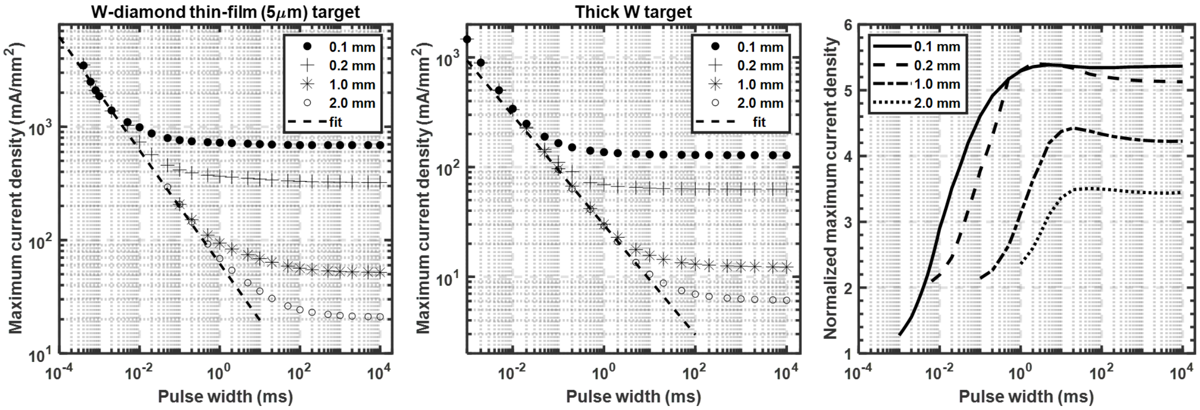

Fig. 5.8: Maximum tube current density vs. pulse width for 5-μm W-diamond thin-film target (left) and thick W target (middle). Simulation results for four different focal spot sizes are shown as scattered plots, and the data of shorter pulses are fitted with $1/\sqrt{t}$. The electron energy was 100 keV for all cases. The 5-μm thin-film target's maximum tube current density is normalized to the thick W target data for each pulse width (right).

the optimal 5-μm W-film are compared with that from the conventional thick W target. Oosterkamp derived that the maximum x-ray tube input power density is proportional to the $1/\sqrt{t}$, where t is the pulse duration under the condition that heat diffusive process is dominant, or equivalently that heat dissipation is irrelevant to the cooling boundaries [14]. In Figure 5.8 (left and middle), both maximum current density vs. pulse duration plots are fitted with $1/\sqrt{t}$ in the short pulse duration region. The value of the fitting parameter is directly related to the thermal properties of the target material(s), which are 62.0 mA·ms$^{0.5}$·mm^{-2} for a 5-μm W-diamond target and 29.6 mA·ms$^{0.5}$·mm^{-2} for thick W target. The maximum tube current density using 5-μm W-diamond target is about twice that of a thick W target. In the long pulse duration region, the maximum tube current density can be approximated as the DC mode. The maximum tube current density using a 5-μm W-diamond target is 5.40, 5.32, 4.52, and 3.50 times the maximum tube current density for a thick W target for focal spot sizes 0.1 mm, 0.2 mm, 1.0 mm, and 2.0 mm, respectively. The comparison results between the two cases are summarized in Figure 5.8. If considering the transmission x-ray production of a 5-μm W-diamond target, the transmission x-ray intensity can be 8.05, 7.93, 6.73, and 5.21 times the maximum produced x-ray intensity for a thick W target.

5.4 Maximum x-ray output in DC mode and optimal target thicknesses

In Figure 5.2 and 5.6, we summarized the intensity produced per mA of electron current and the maximum tube current for different thicknesses of the W film, respectively. By multiplying these two results, we obtained the maximum output x-ray intensity for different thicknesses of the W film, limited by the maximum working temperature of the W-diamond target. Figure 5.9 plots the results for six kVps. For each kVp, there is a range of optimal thicknesses of the W target that can produce maximum intensity. The optimal target thicknesses are almost the same for transmission and reflection targets, and both increase with kVps. The maximum transmission X-ray intensities are more than 40% higher than for the reflection target configuration for all kVps. For each kVp, the range of optimal target thicknesses matches region 2 in Figure 5.6.

The maximum x-ray intensity outputs of various W-film thicknesses were obtained by multiplying the maximum input current in DC mode and the x-ray intensity produced per unit current. Different x-ray sources may operate at different kilovoltage peaks (kVps). We studied clinical imaging settings with kVps ranging from 40 to 150 kV in DC mode. The optimal thickness of the W-diamond for a given kVp generates the largest maximum x-ray intensity either in transmission or reflection direction compared to all other thicknesses.

By normalizing to the maximum possible continuous output x-ray intensity produced by thick tungsten targets described in Section 3.3, we obtained the enhancement of tube output by W-diamond thin-film target over the thick W target. The results for different kVps are plotted in Figure 5.10. The transmission and reflection targets were able to produce up to 6-7 and 4-5 times higher x-ray intensity, respectively than the thick W target. Although the optimal thicknesses vary for different kVp values, the variation is less than ± 2 μm across most of the range of kVps. For example, a 4-5-μm-thick W-diamond target film produces 6-7 times more transmission x-ray intensity than the reflection x-ray of the thick W target over a range of 40-150 kVp with the same focal spot size. In addition, if we choose to use a lower input current and keep the diamond temperature just below 1800 Kelvin, the maximum output intensity decreases about 10%, but this nonetheless largely reduces graphitization of diamond to prolong the target lifetime in continuous mode.

5.5 Fabrication and characterization

5.5.1 Fabrication of W-Diamond Target

The W thin film was deposited on diamond substrates using DC magnetron sputtering (the Kurt J. Lesker PVD 75) from a 99.95% pure W target purchased from Kurt J. Lesker Company. The base pressure in the vacuum chamber of the PVD 75 machine was typically below 1×10^{-5} Torr. Pure (99.99%) argon gas was used as the sputtering gas. The gas pressure was set to 3 mTorr for all the sputtering processes. The diamond substrates were mounted on the rotary metal anode with a rotating speed of three full rotations per second.

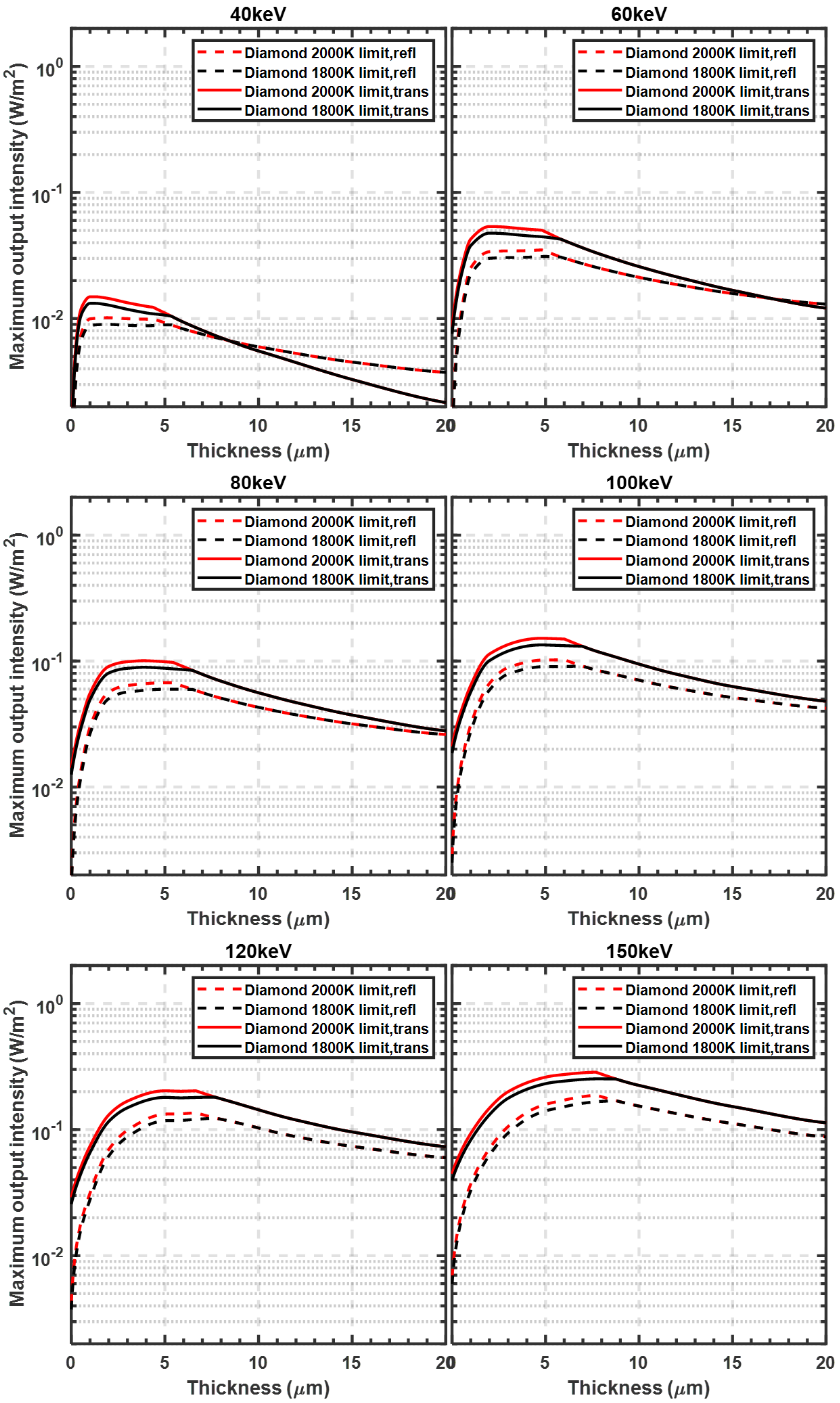

Fig. 5.9: Maximum x-ray intensity at 1 meter away from the target in transmission configuration (solid lines) and reflection configuration (dashed lines) for different kVps. The optimal thicknesses in reflection and transmission target configurations are nearly the same, with transmission target output 40-50% higher than the reflection target.

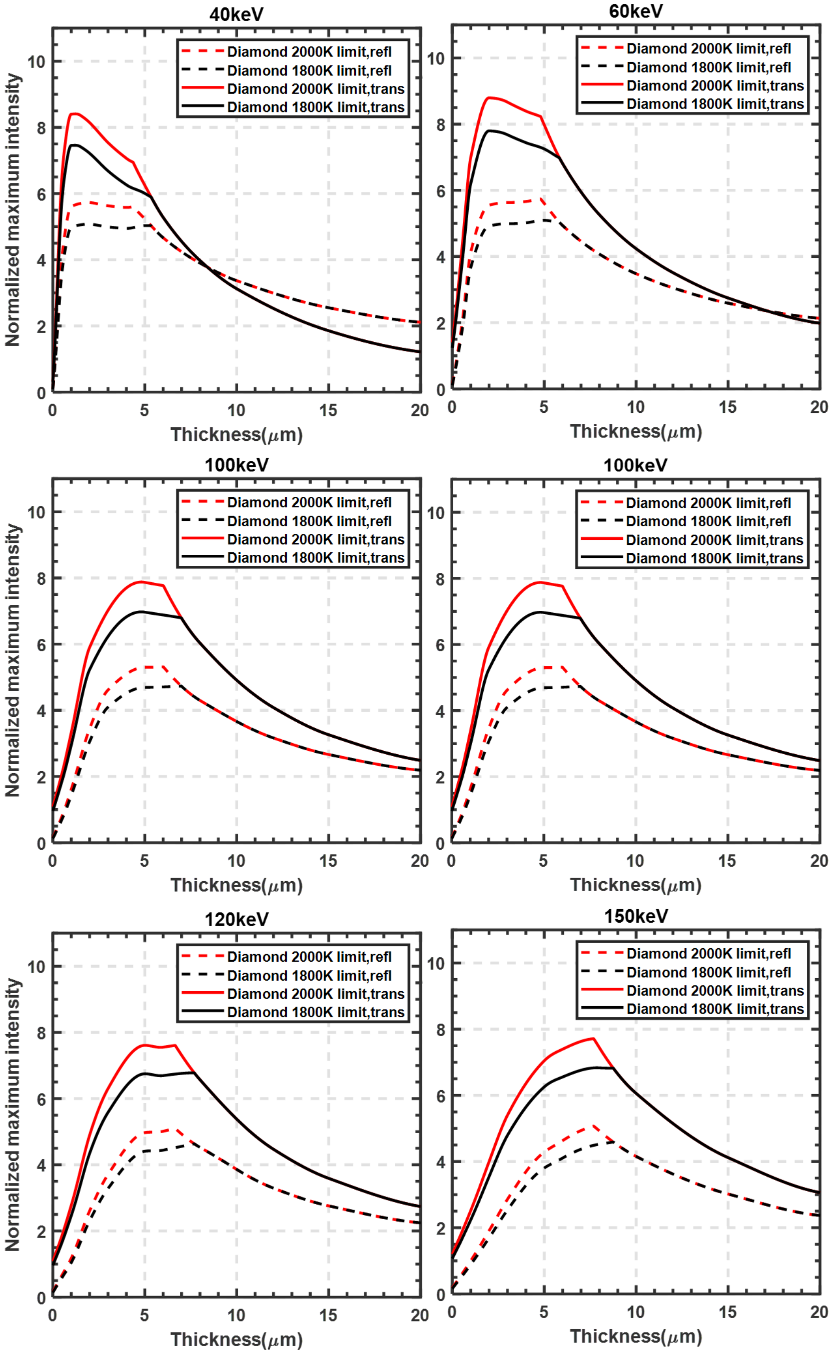

Fig. 5.10: Maximum transmission (solid lines) and reflection (dashed lines) continuous x-ray intensity normalized by the maximum intensity of thick reflection tungsten targets.

The setup is shown in the Figure 5.11.

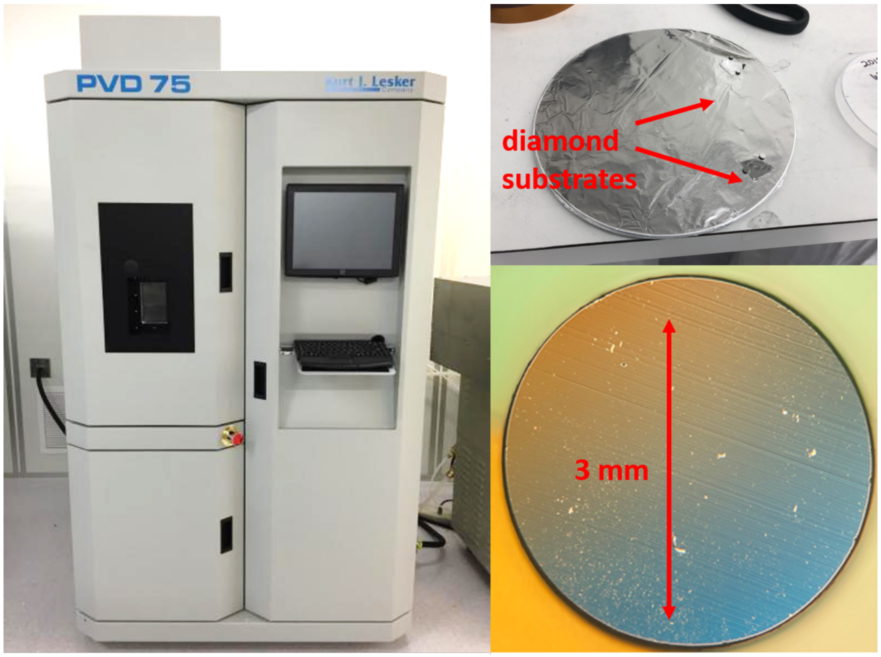

Fig. 5.11: PVD 75 sputtering machine from Kurt J. Lesker in Institute of Material Science and Engineering (IMSE) at Washington University in St. Louis (left). Four diamond substrates were mounted on the metal rotary anode (upper right). Top view of a W film on a diamond substrate sample taken from a microscope (lower right).

5.5.2 Characterization

The film growth rate was measured using the Thermofisher Quattro environmental scanning electron microscope (ESEM) as shown in Figure 5.12 (top). The W film on the silicon substrate was obtained during the fabrication. The power at 120 W for 9600 sec was used in the fabrication process. The sample was cracked into two pieces, and it was mounted into the ESEM. The freshly cut cross-section faced up to the electron beam of ESEM. The SEM image of the film cross-section is shown in Figure 5.12 (bottom left). The thickness of the film can be measured from the figure as 1.18 μm, and since the thickness of the interface layer was negligible, the growth rate is approximately 0.44 μm/hour. The W film was able to be grown over 1 μm thickness on 1-mm thick and 3-mm diameter CVD diamond cylinders purchased from a commercial company. Figure 5.12 (bottom right) shows a realization of the W-diamond design with a copper anode.

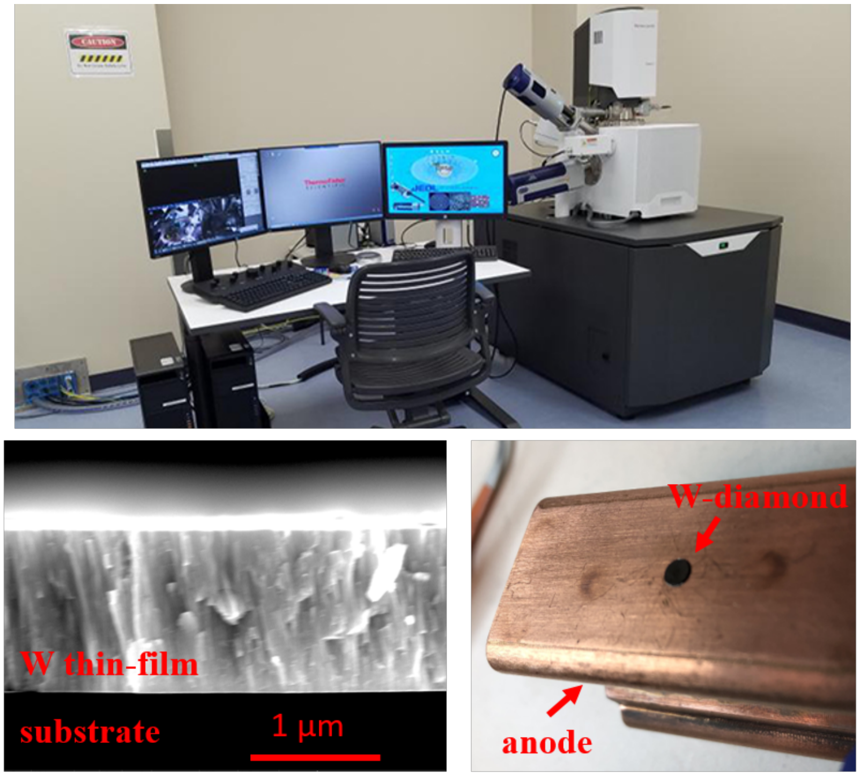

Fig. 5.12: Thermofisher Quattro environmental scanning electron microscope (ESEM) (top). Scanning electron microscope (SEM) image of the cross-section of a fabricated W thin film (bottom left). A single W-diamond target is embedded in a copper anode (bottom right).

5.5.3 Evaluation in an x-ray tube

We built an x-ray testing tube for the W thin-film target. The target was mounted and embedded on a copper or graphite anode. There was a cone-shaped opening on the copper anode to allow the transmission x-rays passing through. The x-ray source design and assembly are illustrated in Figure 5.13 (a-e). A round oxide cathode of 1.27-mm diameter was electrically isolated and mounted on a metal plate. A tuning plate was installed to adjust the focal spot size. The cathode with the focusing plate was placed at a fixed 20 mm distance to the anode and directly faced the W target. The system was aligned by using four assisting metal pins, shown in Figure 5.13 (d). The tube assembly is demonstrated in Figure 5.13 (f). The entire cathode and anode assembly were slotted into a vacuum chamber. The x-ray source was aligned with the optical window of the vacuum chamber, and a star-patterned mask was placed at the center of the window (200 mm to the target). A film detector was plated at 500 mm away from the star pattern. The high voltage source was connected to the anode, and a pulse-generation circuit was connected to the cathode to enable the on/off of the x-ray beam and focusing.

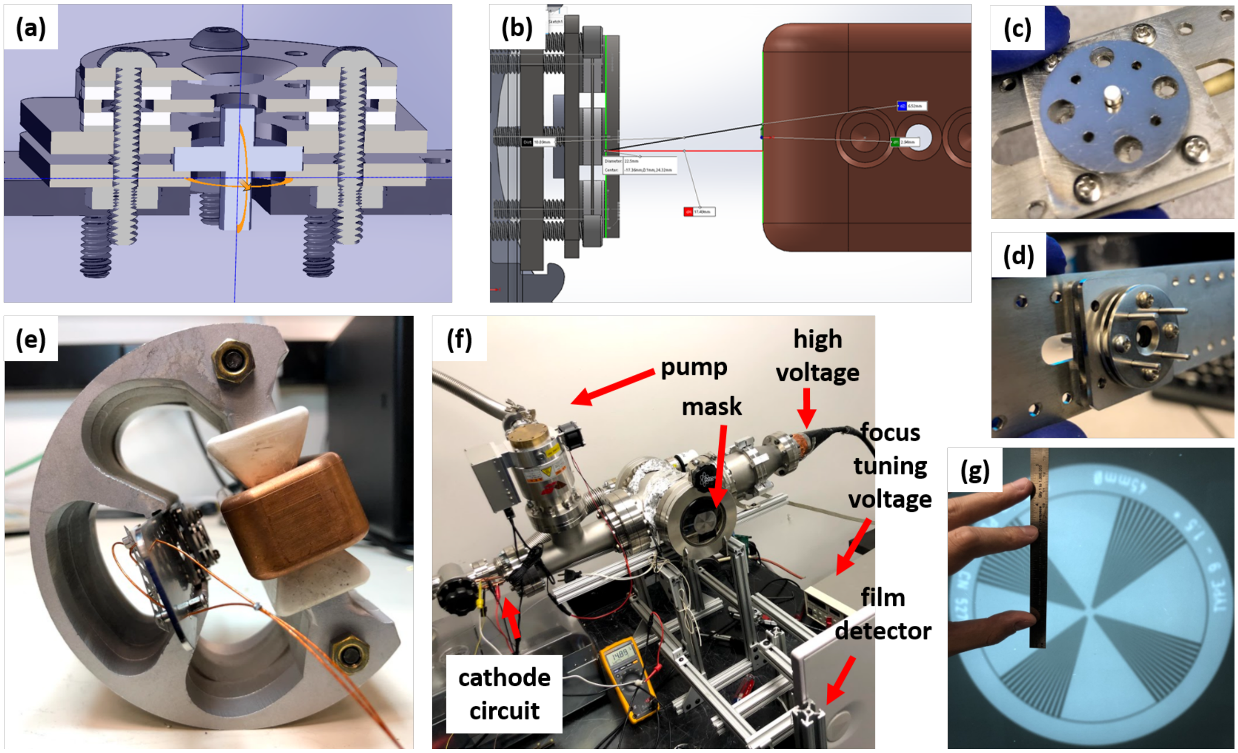

Fig. 5.13: Image of (a) cross-sectional view of the cathode and cathode focusing design, (b) anode and cathode design, (c) cathode assembly with barium oxide coating, (d) cathode focusing assembly, (e) anode and cathode assembly, (f) vacuum chamber assembly, controlling circuit, and a film detector, and (g) image of the star-patterned mask at the film detector.

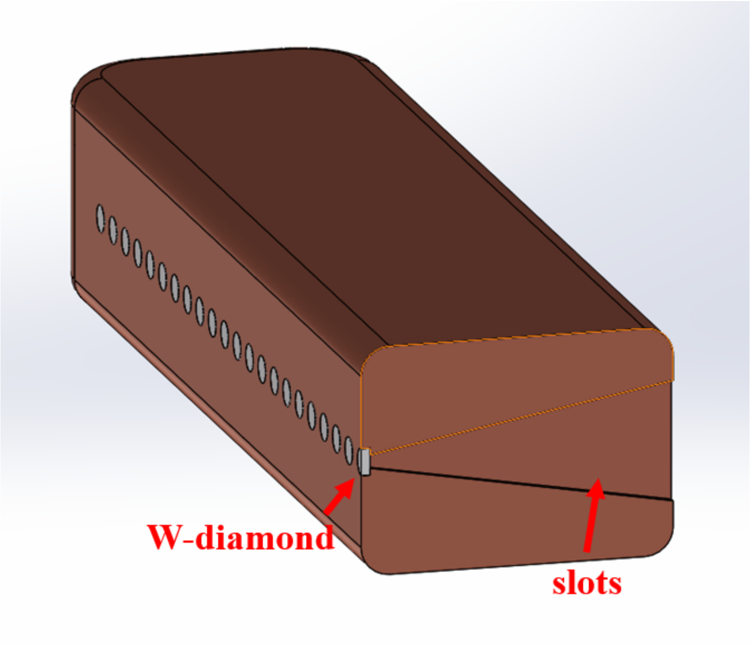

Fig. 5.14: Cross-section of multi-pixel x-ray source anode with thin-film W-diamond targets (left). The W-diamond targets are brazed on the front surface of an elongated anode. A single W-diamond target is embedded in a copper anode (upper right). Scanning electron microscope image of the cross-section of a fabricated W thin film (lower right).

5.6 Discussion

5.6.1 Applications

High-power target for distributed x-ray sources

Thin-film W-diamond targets can be used in both transmission and reflection configurations. Figure 5.14 (left) shows the CAD design of the anode of MPTEX source with thin-film W-diamond targets. The anode can be made of oxygen-free copper or graphite. When used as a transmission source, the anode body will be machined with thin slots, labelled in the Figure 5.14 (left). These anode slots collimate x-ray beams to the x-ray detector. When used as a reflection target, the anode slots are not necessary, and the multi-slot x-ray collimator will be mounted outside the tube. In both cases, the anode can be liquid-cooled and maintain a relatively low temperature at the anode surface.

Quasi-monochromatic x-ray source

In conventional X-ray sources, an energetic electron beam is incident on a thick solid target material, which produces primarily reflective Bremsstrahlung, the continuum X-rays, while the characteristic K-lines are not as significant. However, shown in Figure 5.3, a thin-film target, due to the different physical origin of these two types of X-ray production, produces isotropic discrete K-lines and forward-distributed anisotropic white Bremsstrahlung X-rays. In the reflective direction, the Bremsstrahlung's intensity is largely suppressed, and the K-lines' intensity remains the same. A quasi-monochromatic spectrum can be obtained in the reflective direction of the target [99]. Diamond, as a low density and low Z material, has the highest thermal conductivity among all known solid materials and also stays stable at high temperatures[80]. It is suitable as the substrate material since it produces less utterly fewer X-rays than the higher Z target materials and performs as a heatsink to increase the input power of electron bombardment and compensate for the reduction of x-ray production due to the thin-film design. It is possible to select target materials whose K-lines matching the K-absorption peak of contrast attentions. For example, Cerium oxide can be the target material whose K-lines are at 33.90, 34.28, and 34.72 keV. They match the K-edge of the iodine contrast at 33.2 keV. This source is potentially useful to detect the micro-calcification in mammography.

5.6.2 Limitation and future work

Our simulation studies have demonstrated that distributed x-ray sources with W-diamond thin-film target can produce 6-7 times higher transmission and 4-5 times higher reflection x-ray intensity than for traditional thick W targets operating in continuous mode, and up to 7 times more in pulsed mode, depending on the pulse duration and focal spot size. The target design can greatly accelerate the imaging speeds of distributed x-ray source imaging systems. This improvement is due to multiple factors, including that (1) the localized heat spreads out faster due to the high thermal conductivity of the diamond, (2) a higher radiative yield in the W film due to the higher mean energy of the electrons interacting with the W film, and (3) diamond substrate receives low energy photons at the deeper target location to avoid spurious heating by low energy electrons in the W film.

Multi-pixel x-ray sources operate in pulse mode. Our results indicate that a small focal spot size is less dependent on pulse duration. In particular, 0.1 mm diameter focal spot has almost the same x-ray intensity for pulse durations ranging from 10 ms to 0.1 ms; while for a 1 mm focal spot, the power can increase by a factor of either 3 or 6 for W-diamond thin-film targets or thick W targets, respectively. In this study, we only simulated the maximum power for a single pulse. For the simulation for multiple pulses with duty cycle and frequency, it might not be easy to define the optimal operating condition, and the analysis can be much more complicated, which we might investigate in later studies.

Diamond has the highest thermal conductivity among all known materials. Although the cost of CVD diamond has decreased dramatically, large-area CVD diamond for a 2D distributed x-ray source is still not commercially available. SBDX sources employ a transmission target with tungsten film coated on beryllium substrates (melting point at 1560 K and thermal conductivity at 200 W/(m·K)) and have been able to achieve much higher powers than other distributed x-ray sources with W reflection targets. Other high thermal conductivity materials such as pyrolytic graphite can also be good candidates for the target substrate. Pyrolytic graphite has excellent in-plane thermal conductivity (1800 W/(m·K)) and has been used in heat sinks in electronics.

We obtained W-diamond using the low-power sputtering deposition method. The thickness of the W thin film deposited on the diamond and growing efficiency by sputtering can be a limiting factor in practice. There are other physical or chemical methods that can be utilized to fabricate W-diamond targets with sufficient W thickness - for example, directly brazing the CVD diamond on an extremely thin W foil.

Our results demonstrate that W-diamond targets can produce about 40% more x-ray intensity when used as transmission rather than reflection targets with the same focal spot size. Transmission targets may also have advantages in the tube design. Compared with the rotating anode, the fixed anode of the multi-pixel x-ray source may have direct contact with the tube housing so that heat can be rapidly removed from the anode. However, the transmission target cannot utilize the anode angle to increase x-ray intensity and thus will have a smaller physical focal spot size than the reflection target.

Chapter 6

Conclusion

The multi-pixel thermionic emission x-ray tube (MPTEX), that was developed, tested and assembled in our lab, is a high-power distributed x-ray source for novel x-ray imaging applications. Fourty-eight oxide-coated cathode emitters were assembled in triodes and with electron beam optics plates, and they were arranged in a linear array (4 mm spacing from every two adjacent sources). Controller electronics were developed to control each x-ray beam. We demonstrated the tetrahedron-beam (TB) x-ray imaging using our MPTEX source and a photon-counting detector. Phantom and animal imaging showed that the TB system can produce high quality radiographic and tomographic images comparable to diagnostic helical CT imaging.

A novel small animal x-ray FLASH irradiator (SAFI) based on the concept of MPTEX source was proposed. We did simulation studies to estimate the tube power requirements and the dose rate limits of SAFI. Fifty-one focal spots with a dimension of 2 mm × 20 mm on a 200 mm diameter ring can produce over 120 Gy/s radiation dose at the center of the SAFI system. The system can deliver higher dose rate irradiation with shorter beam-on duration. We further demonstrated forward and inverse FLASH radiotherapy treatment planning for a cylindrical water phantom, as well as a design of inverse-geometry micro-CT associated with the irradiator.

Finally, an innovative composite x-ray target, the thin-film tungsten(W)-diamond target, was studied. It can potentially enhance the power of an x-ray tube using stationary anode, such as microfocus x-ray source and distributed x-ray source. We optimized the thickness of the W film for variety of tube conditions, including the electron beam energy, pulse width, and imaging geometry. The maximum focal spot power density was limited by either the graphitization of the diamond substrate or the melting point of the W target. With optimal W target thickness, the maximum transmission x-ray intensities are about 40-50% higher than the maximum reflection intensities. Thin-film W-diamond targets allow 4-5 times more maximum power input and produce 6-7 times higher transmission x-ray intensity in continuous mode compared with conventional reflection W thick targets. Depending on the focal spot size, reducing the x-ray pulse duration can further enhance the tube power. The progress on target's fabrication and testing was also presented.

References

1. Maltz, J. S. *et al.* Fixed gantry tomosynthesis system for radiation therapy image guidance based on a multiple source x-ray tube with carbon nanotube cathodes. *Medical physics* **36,** 1624–1636 (2009).
2. De Man, B. *et al.* Multisource inverse-geometry CT. Part I. System concept and development. *Medical Physics* **43,** 4607–4616. `http://dx.doi.org/10.1118/1.4954846` (2016).
3. Behling, R. *Modern diagonostic x-ray sources: technology, manufacturing, reliability.* ISBN: 9781482241334 (CRC Press, 2021).
4. Coolidge, W. D. A powerful Röntgen ray tube with a pure electron discharge. *Physical Review* **2,** 409 (1913).
5. Wood, R. W. A new form of cathode discharge and the production of X-rays, together with some notes on diffraction. Preliminary communication. *Physical Review (Series I)* **5,** 1 (1897).
6. Bouwers, A. Self-protecting Tubes and Their Influence on the Development of X-ray Technic. *Radiology* **13,** 191–206 (1929).
7. Nottingham, W. B. Thermionic emission from tungsten and thoriated tungsten filaments. *Physical Review* **49,** 78 (1936).
8. Herrmann, G. & Wagener, S. *The Oxide-coated Cathode: Physics, including thermal emission from metals and semi-conductors* (1951).
9. Futamoto, M., Nakazawa, M., Usami, K., Hosoki, S. & Kawabe, U. Thermionic emission properties of a single-crystal LaB6 cathode. *Journal of Applied Physics* **51,** 3869–3876 (1980).
10. Cheng, Y. *et al.* Dynamic radiography using a carbon-nanotube-based field-emission x-ray source. *Review of scientific instruments* **75,** 3264–3267 (2004).

11. Glukhova, O., Gulyaev, U., Sinitsyn, N. & Torgashov, G. *Carbon nanotubes - Based the cold cathode for field emission electronics* in *2014 Tenth International Vacuum Electron Sources Conference (IVESC)* (2014), 1–2.

12. Gidcumb, E. *et al.* Carbon nanotube electron field emitters for x-ray imaging of human breast cancer. *Nanotechnology* **25,** 245704 (2014).

13. Heo, S. H., Ihsan, A. & Cho, S. O. Transmission-type microfocus x-ray tube using carbon nanotube field emitters. *Applied Physics Letters* **90** (2007).

14. Oosterkamp, W. J. The heat dissipation in the anode of an X-ray tube. *Philips Research Reports* **3,** 303–317 (1948).

15. Whitaker, S. *X-ray anode surface temperatures: the effect of volume heating* in *Medical Imaging II* **914** (1988), 565–576.

16. Malmqvist, L., Rymell, L., Berglund, M. & Hertz, H. Liquid-jet target for laser-plasma soft x-ray generation. *Review of scientific instruments* **67,** 4150–4153 (1996).

17. Müller, M., Mey, T., Niemeyer, J. & Mann, K. Table-top soft x-ray microscope using laser-induced plasma from a pulsed gas jet. *Optics express* **22,** 23489–23495 (2014).

18. Hsieh, J. *Computed Tomography: Principles, Design, Artifacts, and Recent Advances, Third Edition* (SPIE, 2015).

19. Speidel, M. A., Wilfley, B. P., Star-Lack, J. M., Heanue, J. A. & Van Lysel, M. S. Scanning-beam digital x-ray (SBDX) technology for interventional and diagnostic cardiac angiography. *Medical physics* **33,** 2714–2727 (2006).

20. Speidel, M. A. *et al.* Comparison of entrance exposure and signal-to-noise ratio between an SBDX prototype and a wide-beam cardiac angiographic system. *Medical physics* **33,** 2728–2743 (2006).

21. Burion, S., Speidel, M. A. & Funk, T. A real-time regional adaptive exposure method for saving dose-area product in x-ray fluoroscopy. *Medical Physics* **40,** 51911 (2013).

22. Mazin, S. R., Star-Lack, J., Bennett, N. R. & Pelc, N. J. Inverse-geometry volumetric CT system with multiple detector arrays for wide field-of-view imaging. *Medical physics* **34,** 2133–2142 (2007).

23. Schmidt, T. G., Fahrig, R., Pelc, N. J. & Solomon, E. G. An inverse-geometry volumetric CT system with a large-area scanned source: A feasibility study. *Medical Physics* **31,** 2623–2627 (2004).

24. Spronk, D. *et al.* Evaluation of carbon nanotube x-ray source array for stationary head computed tomography. *Medical physics* **48,** 1089–1099 (2021).

25. Kandlakunta, P., Pham, R., Khan, R. & Zhang, T. Development of multi-pixel x-ray source using oxide-coated cathodes. *Physics in Medicine & Biology* **62,** N320 (2017).

26. Neculaes, V. B. *et al.* Multisource inverse-geometry CT. Part II. X-ray source design and prototype. *Medical Physics* **43,** 4617–4627. `http://dx.doi.org/10.1118/1.4954847` (2016).

27. Baek, J. *et al.* A multi-source inverse-geometry CT system: initial results with an 8 spot x-ray source array. *Physics in Medicine & Biology* **59,** 1189 (2014).

28. Qian, X. *et al.* High resolution stationary digital breast tomosynthesis using distributed carbon nanotube x-ray source array. *Medical physics* **39,** 2090–2099 (2012).

29. Xu, X. *et al.* A tetrahedron beam computed tomography benchtop system with a multiple pixel field emission x-ray tube. *Medical physics* **38,** 5500–5508 (2011).

30. Ultrahigh dose-rate FLASH irradiation increases the differential response between normal and tumor tissue in mice. *Science Translational Medicine* **6,** 245ra93 (2014).

31. Barendsen, G., Beusker, T., Vergroesen, A. & Budke, L. Effects of different ionizing radiations on human cells in tissue culture: II. Biological experiments. *Radiation Research* **13,** 841–849 (1960).

32. Fowler, J. F. & Stern, B. E. Dose-rate effects: some theoretical and practical considerations. *The British journal of radiology* **33,** 389–395 (1960).

33. Cottrell, S. S. *Do Colors Exist?: And Other Profound Physics Questions* (Birkhäuser, 2018).

34. Romano, F., Bailat, C., Jorge, P. G., Lerch, M. L. F. & Darafsheh, A. Ultra-high dose rate dosimetry: challenges and opportunities for FLASH radiation therapy. *Medical Physics* (2022).

35. Darafsheh, A. *et al.* Feasibility of proton FLASH irradiation using a synchrocyclotron for preclinical studies. *Medical Physics* **47,** 4348–4355 (2020).

36. Montay-Gruel, P. *et al.* Irradiation in a flash: Unique sparing of memory in mice after whole brain irradiation with dose rates above 100 Gy/s. *Radiotherapy and Oncology* **124,** 365–369 (2017).

37. Schüler, E. *et al.* Experimental Platform for Ultra-high Dose Rate FLASH Irradiation of Small Animals Using a Clinical Linear Accelerator. *International Journal of Radiation Oncology Biology Physics* **97,** 195–203 (2017).

38. Jaccard, M. *et al.* High dose-per-pulse electron beam dosimetry: Commissioning of the Oriatron eRT6 prototype linear accelerator for preclinical use. *Medical Physics* **45,** 863–874 (2017).

39. Montay-Gruel, P. *et al.* X-rays can trigger the FLASH effect: Ultra-high dose-rate synchrotron light source prevents normal brain injury after whole brain irradiation in mice. *Radiotherapy and Oncology* **129,** 582–588. `https://doi.org/10.1016/j.radonc.2018.08.016` (2018).

40. Patriarca, A. *et al.* Experimental Set-up for FLASH Proton Irradiation of Small Animals Using a Clinical System. *International Journal of Radiation Oncology Biology Physics* **102,** 619–626 (2018).

41. Lempart, M. *et al.* Modifying a clinical linear accelerator for delivery of ultra-high dose rate irradiation. *Radiotherapy and Oncology* **139,** 40–45. `https://doi.org/10.1016/j.radonc.2019.01.031` (2019).

42. Vozenin, M. C. *et al.* The Advantage of FLASH Radiotherapy Confirmed in Mini-pig and Cat-cancer Patients. *Clinical Cancer Research* **25,** 35–42 (2019).

43. Bourhis, J. *et al.* Treatment of a first patient with FLASH-radiotherapy. *Radiotherapy and Oncology* **139,** 18–22. `https://doi.org/10.1016/j.radonc.2019.06.019` (2019).

44. Girdhani, S. *et al. Abstract LB-280: FLASH: A novel paradigm changing tumor irradiation platform that enhances therapeutic ratio by reducing normal tissue toxicity and activating immune pathways* 2019.

45. Simmons, D. A. *et al.* Reduced cognitive deficits after FLASH irradiation of whole mouse brain are associated with less hippocampal dendritic spine loss and neuroinflammation. *Radiotherapy and Oncology* **139,** 4–10. `https://doi.org/10.1016/j.radonc.2019.06.006` (2019).

46. Bazalova-Carter, M. & Esplen, N. On the capabilities of conventional x-ray tubes to deliver ultra-high (FLASH) dose rates. *Medical Physics* **46,** 5690–5695 (2019).

47. Diffenderfer, E. S. *et al.* Design, Implementation, and in Vivo Validation of a Novel Proton FLASH Radiation Therapy System. *International Journal of Radiation Oncology Biology Physics* **106,** 440–448. `https://doi.org/10.1016/j.ijrobp.2019.10.049` (2020).

48. Chabi, S. *et al.* Ultra-high-dose-rate FLASH and conventional-dose-rate irradiation differentially affect human acute lymphoblastic leukemia and normal hematopoiesis. *International Journal of Radiation Oncology* Biology* Physics* **109,** 819–829 (2021).

49. Fouillade, C. *et al.* FLASH irradiation spares lung progenitor cells and limits the incidence of radio-induced senescence. *Clinical Cancer Research* **26,** 1497–1506 (2020).

50. Rezaee, M., Iordachita, I. & Wong, J. W. Ultrahigh dose-rate (FLASH) x-ray irradiator for pre-clinical laboratory research. *Physics in Medicine and Biology* **66** (2021).

51. Gao, F. *et al.* First demonstration of the FLASH effect with ultrahigh dose rate high-energy X-rays. *Radiotherapy and Oncology* **166,** 44–50 (2021).

52. Tan, Y. *et al.* A Novel Small Animal FLASH Irradiator (SAFI) Based on Distributed kV X-ray Sources. *Medical Physics* (2022).

53. Wang, X. *et al.* Performance of an oxide cathode prepared from submicrometer carbonates. *IEEE transactions on electron devices* **58,** 3195–3199 (2011).

54. Chen, Q. *et al.* Tetrahedron beam imaging with a multi-pixel thermionic emission X-ray source and a photon-counting detector: A benchtop experimental study. *Medical Physics* **48,** 7250–7260 (2021).

55. Zhang, T., Schulze, D., Xu, X. & Kim, J. Tetrahedron beam computed tomography (TBCT): a new design of volumetric CT system. *Physics in Medicine & Biology* **54,** 3365 (2009).

56. Kim, J., Lu, W. & Zhang, T. Dual source and dual detector arrays tetrahedron beam computed tomography for image guided radiotherapy. *Physics in Medicine & Biology* **59,** 615 (2014).

57. Spiegler, P. & Breckinridge, W. C. Imaging of focal spots by means of the star test pattern. *Radiology* **102,** 679–685 (1972).

58. Feldkamp, L. A., Davis, L. C. & Kress, J. W. Practical cone-beam algorithm. *Josa a* **1,** 612–619 (1984).

59. Kak, A. C. & Slaney, M. *Principles of computerized tomographic imaging* (SIAM, 2001).

60. Montay-gruel, P. *et al.* Erratum: Long-term neurocognitive benefits of FLASH radiotherapy driven by reduced reactive oxygen species. *Proceedings of the National Academy of Sciences of the United States of America* **117,** 25946–25947 (2020).

61. Beyreuther, E. *et al.* Feasibility of proton FLASH effect tested by zebrafish embryo irradiation. *Radiotherapy and Oncology* **139,** 46–50. `https://doi.org/10.1016/j.radonc.2019.06.024` (2019).

62. Levy, K. *et al.* Abdominal FLASH irradiation reduces radiation-induced gastrointestinal toxicity for the treatment of ovarian cancer in mice. *Scientific Reports* **10,** 1–14. `https://doi.org/10.1038/s41598-020-78017-7` (2020).

63. Kim, M. M. *et al.* Development of ultra-high dose rate (FLASH) particle therapy. *IEEE Transactions on Radiation and Plasma Medical Sciences* (2021).

64. Wei, S. *et al.* FLASH Radiotherapy Using Single-Energy Proton PBS Transmission Beams for Hypofractionation Liver Cancer: Dose and Dose Rate Quantification. *Frontiers in Oncology* **11,** 813063 (2021).

65. Koch, C. J. Re: Differential impact of FLASH versus conventional dose rate irradiation: Spitz et al. *Radiotherapy and oncology : journal of the European Society for Therapeutic Radiology and Oncology* **139,** 62–63. `https://doi.org/10.1016/j.radonc.2019.07.004` (Oct. 2019).

66. An integrated physico-chemical approach for explaining the differential impact of FLASH versus conventional dose rate irradiation on cancer and normal tissue responses. *Radiotherapy and Oncology* **139,** 23–27. `https://doi.org/10.1016/j.radonc.2019.03.028` (2019).

67. Adrian, G. *et al.* The FLASH effect depends on oxygen concentration. *The British Journal of Radiology* **92,** 20190702 (2020).

68. Jansen, J. *et al.* Does FLASH deplete oxygen? Experimental evaluation for photons, protons, and carbon ions. *Medical physics* **48,** 3982–3990 (2021).

69. Buchsbaum, J. C. *et al.* FLASH radiation therapy: new technology plus biology required. *International Journal of Radiation Oncology, Biology, Physics* **110,** 1248–1249 (2021).

70. Darafsheh, A. *et al.* Spread-out Bragg peak proton FLASH irradiation using a clinical synchrocyclotron: Proof of concept and ion chamber characterization. *Medical physics* **48,** 4472–4484 (2021).

71. Grilj, V., Buonanno, M., Welch, D. & Brenner, D. J. Proton Irradiation Platforms for Preclinical Studies of High-Dose-Rate (FLASH) Effects at RARAF. *Radiation Research* **194,** 646–655 (2020).

72. Zhang, Q. *et al.* Flash investigations using protons: Design of delivery system, preclinical setup and confirmation of flash effect with protons in animal systems. *Radiation Research* **194,** 656–664 (2020).

73. Cecchi, D. D. *et al.* Characterization of an x-ray tube-based ultrahigh dose-rate system for in vitro irradiations. *Medical Physics,* 1–11 (2021).

74. Maxim, P. G., Tantawi, S. G. & Loo, B. W. PHASER: A platform for clinical translation of FLASH cancer radiotherapy. *Radiotherapy and Oncology* **139,** 28–33. `https://doi.org/10.1016/j.radonc.2019.05.005` (2019).

75. Schmidt, T. G., Fahrig, R. & Pelc, N. J. A three-dimensional reconstruction algorithm for an inverse-geometry volumetric CT system. *Medical Physics* **32,** 3234–3245 (2005).

76. Thibault, J. B., Sauer, K. D., Bouman, C. A. & Hsieh, J. A three-dimensional statistical approach to improved image quality for multislice helical CT. *Medical Physics* **34,** 4526–4544 (2007).

77. Tang, J., Nett, B. E. & Chen, G. H. Performance comparison between total variation (TV)-based compressed sensing and statistical iterative reconstruction algorithms. *Physics in Medicine and Biology* **54,** 5781–5804 (2009).

78. Grider, D. E., Wright, A. & Ausburn, P. K. Electron beam melting in microfocus X-ray tubes. *Journal of Physics D: Applied Physics* **19,** 2281–2292 (1986).

79. Qian, X. *et al.* Design and characterization of a spatially distributed multibeam field emission x-ray source for stationary digital breast tomosynthesis. *Medical physics* **36,** 4389–4399 (2009).

80. Twitchen, D. J., Pickles, C. S. J., Coe, S. E., Sussmann, R. S. & Hall, C. E. Thermal conductivity measurements on CVD diamond. *Diamond and related materials* **10,** 731–735 (2001).

81. Delfaure, C. *et al.* Nanofocus diamond X-ray windows: Thermal modeling of nano-sized heat source systems. *Diamond and Related Materials* **59,** 104–115. `http://dx.doi.org/10.1016/j.diamond.2015.09.015` (2015).

82. Zheng, L., Liu, H. & Wang, J. Transmission-type Window of HFCVD Diamond Film for Microfocus X-ray Tube (2016).

83. Badali, D. S. *et al.* Characterization of an x-ray source with a partitioned diamond-tungsten target for electronic brachytherapy with 3D beam directionality. *Physics in Medicine and Biology* **64** (2019).

84. Kandlakunta, P., Thomas, A., Tan, Y., Khan, R. & Zhang, T. Design and numerical simulations of W-diamond transmission target for distributed x-ray sources. *Biomedical physics & engineering express* **5,** 25030 (2019).

85. Li, X., Wang, X., Li, Y. & Liu, Y. Production and heat properties of an X-ray reflective anode based on a diamond heat buffer layer. *Materials* **13** (2020).

86. Távora, L. M., Morton, E. J. & Gilboy, W. B. Design considerations for transmission X-ray tubes operated at diagnostic energies. *Journal of Physics D: Applied Physics* **33,** 2497–2507 (2000).

87. Harding, G., David, B., Harding, A., Thran, A. & Schlomka, J. P. Directional enhancement of characteristic relative to bremsstrahlung X-rays: Foil thickness optimization. *Radiation Physics and Chemistry* **76,** 1116–1121 (2007).

88. Ihsan, A., Heo, S. H. & Cho, S. O. A microfocus X-ray tube based on a microstructured X-ray target. *Nuclear Instruments and Methods in Physics Research, Section B: Beam Interactions with Materials and Atoms* **267,** 3566–3573. `http://dx.doi.org/10.1016/j.nimb.2009.08.012` (2009).

89. Maeo, S., Krämer, M. & Taniguchi, K. Development of a microfocus x-ray tube with multiple excitation sources. *Review of Scientific Instruments* **80,** 1–6 (2009).

90. Grant, E. J., Posada, C. M., Castaño, C. H. & Lee, H. K. A Monte Carlo simulation study of a flat-panel X-ray source. *Applied Radiation and Isotopes* **70,** 1658–1666 (2012).

91. Avachat, A. V., Tucker, W. W., Giraldo, C. H., Pommerenke, D. & Lee, H. K. Looking Inside a Prototype Compact X-Ray Tube Comprising CNT-Based Cold Cathode and Transmission-Type Anode. *Radiation Research* **193,** 497–504 (2020).

92. Pandola, L., Andenna, C. & Caccia, B. Validation of the Geant4 simulation of bremsstrahlung from thick targets below 3 MeV. *Nuclear Instruments and Methods in Physics Research Section B: Beam Interactions with Materials and Atoms* **350,** 41–48 (2015).

93. Berman, R., Hudson, P. R. W. & Martinez, M. Nitrogen in diamond: evidence from thermal conductivity. *Journal of Physics C: Solid State Physics* **8,** L430 (1975).

94. Hust, J. G. & Lankford, A. B. *Thermal conductivity of aluminum, copper, iron, and tungsten for temperatures from 1 K to the melting point* tech. rep. (National Bureau of Standards, Boulder, CO (USA). Chemical Engineering∼. . ., 1984).

95. Olson, J. R. *et al.* Thermal conductivity of diamond between 170 and 1200 K and the isotope effect. *Physical Review B* **47,** 14850 (1993).

96. Howes, V. R. The graphitization of diamond. *Proceedings of the Physical Society (1958-1967)* **80,** 648 (1962).

97. Yeh, J. J., Pfeffer, R. L., Cole, M. W., Ohring, M. & Yehoda, J. E. Reactions between tungsten and molybdenum thin films and polycrystalline diamond substrates. *Diamond and Related Materials* **5,** 1195–1203 (1996).

98. Davies, G. & Evans, T. Graphitization of diamond at zero pressure and at a high pressure. *Proceedings of the Royal Society of London. A. Mathematical and Physical Sciences* **328,** 413–427 (1972).

99. Motz, J. W., Dick, C. E., Lucas, A. C., Placious, R. C. & Sparrow, J. H. Production of High-Intensity K X-Ray Beams. *Journal of Applied Physics* **42,** 2131–2133. `http://aip.scitation.org/doi/10.1063/1.1660500` (Apr. 1971).